STUDY OF THE d(^{7}Be,^{8}B)n REACTION

By

Christopher F. Powell

A DISSERTATION

Submitted to
Michigan State University
in partial fulfillment of the requirements
for the Degree of

DOCTOR OF PHILOSOPHY

Department of Chemistry

1998

ABSTRACT

STUDY OF THE d(^{7}Be,^{8}B)n REACTION

By

Christopher F. Powell

A number of previous experiments have been performed which were designed to study the structure of the ^{8}B nucleus and to determine whether or not it exhibits a proton halo. These studies have reached conflicting conclusions, and have arrived at very different values for basic properties of the ^{8}B nucleus, such as its radius. We have performed a different type of experiment in order to determine whether such a measurement can provide additional information about the ^{8}B nucleus. We approached the problem using a traditional technique in the study of nuclear structure: a single-nucleon transfer reaction.

In the present study we have performed two experiments designed to measure the cross section of the reaction transferring a single proton from deuterium to ^{7}Be, forming ^{8}B and a neutron: the d(^{7}Be,^{8}B)n reaction. A kinematically complete study of this reaction has been made, measuring the angle and energy of both reaction products. We have also measured the scattering cross section of the two reactants: d(^{7}Be,^{7}Be)d. The measured cross sections were compared to the results of calculations made in the Optical Model framework. The results of DWBA calculations using several Optical Potentials from the

literature are compared to the measurements, and potentials have been fit to the scattering cross section.

We have also made similar measurements for the proton transfer reaction from deuterium to ^{12}C forming ^{13}N, and the scattering of ^{12}C from deuterium. The results of additional DWBA calculations using Optical Potentials from the literature were compared to the measured cross sections.

To my parents

ACKNOWLEDGMENTS

First, I would like to thank my advisor, Prof. Dave Morrissey, for the guidance, support, and friendship he has given me. You were always there with help when I needed it, and have been an excellent teacher and advocate.

Thanks to Vic Viola and Kris Kwiatkowski, my undergraduate research advisors at IUCF. You gave me my start in research, and gave me confidence in my abilities that even grad school couldn't erase.

Thanks to the A1200 post-docs of a few years ago who helped me in my formative years, Maggie Hellström and Jim Brown. Both of you taught me a great deal, and always found answers for my questions.

Thanks to the former grad students at IUCF, Kevin Morley, Dave Bracken, and Erin Foxford. The three of you were great role models for a young scientist.

Thanks to Prof. Paul Mantica, who has been a good friend, a great source of knowledge, and a tenacious defender in the post.

Special thanks to my chemistry friends: Dr. Per Askeland, Dr. Matt Gardner, Dr. Sara Helvoigt, and Prof. Michelle Mac. You guys were my classmates, my roommates, my teammates, and my soul mates. After some of those nights at Dag's we probably mated in other unspeakable ways as well. More thanks to Greg, Mike, Sue, Rob, and Kerry.

More special thanks to my cyclotron friends: Don Anthony, Jac Caggiano, and Jon Kruse. You have been great friends, and knowing you guys were around made it a little

easier to drag myself into work (most) every moring. You have also been great teachers; I've learned at least as much from you as from my research. More thanks to Pat, Barry, Njema, Erik, Heiko, Mike, Raman, and Mathias.

Still more special thanks to my parents, Joseph and Francyne Powell. You have always been a source of love, support, and understanding. Everything I have accomplished has been made possible by the integrity, self-respect, and self-confidence that you have instilled in me. I owe you my deepest gratitude, and share with you my deepest love.

Love and thanks to the rest of my family: Rob, Barb, Sue, Carolyn, Mike, Jen, Steve, Cathy, Al, Don, Glenn, Karen, Beth, Michael, Rachael, Thomas, Emily, Abby, Danielle, Christina, Katie, and all of those still to come.

Finally, I thank Jennifer Hudson for her patience and her love. You've been my inspiration and my dearest friend. You kept me going through the best and the worst. Thank you for sharing it all with me.

Contents

List of Tables

List of Figures

Chapter 1

Introduction

1.1 Physics with Radioactive Nuclear Beams

Traditional studies of the atomic nucleus could only be made using ion beams of naturally abundant nuclei and stable targets. Thus, experimental programs were limited to working with those nuclei which are stable and can be found in nature. With the advent of radioactive beam facilities, a much broader range of nuclei can be utilized. These facilities allow beams of 'exotic' nuclei to be produced, and studies of their structure and reactions to be performed. While fewer than 300 nuclei are stable and can be found in nature, predictions show that about 7,000 nuclei should be particle stable, with lifetimes long on the nuclear time scale. The broad range of these nuclei is illustrated in Figure 1.1, the chart of the nuclides. Stable nuclei are indicated by the solid squares, while nuclei that have been observed experimentally lie between the two solid lines. The two dashed lines indicate the predicted limits of nuclear stability, the proton and neutron driplines.

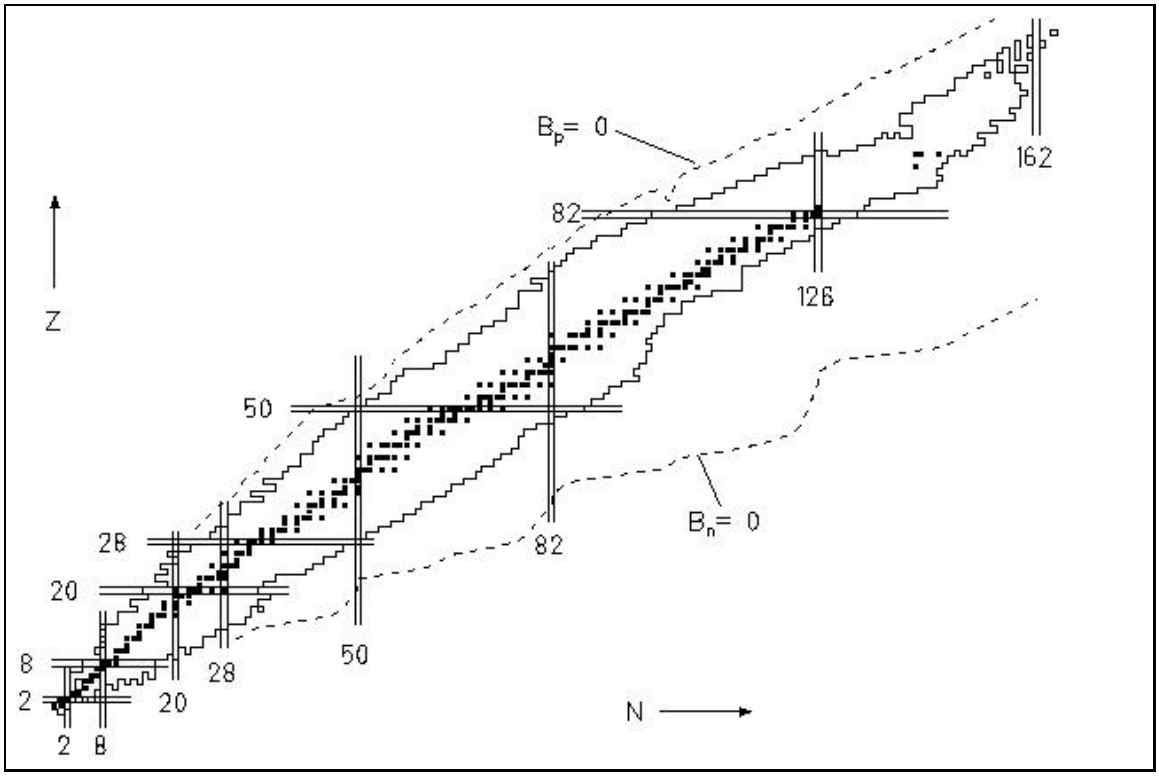

Figure 1.1 The Chart of the Nuclides. Stable nuclei are shown as solid squares, with nuclei that have been observed bound by the solid lines. The dashed lines show the predicted positions of the proton and neutron driplines. The closed proton and neutron shells at 2, 8, 20, 28, 50, 82, 126, and 162 are indicated.

With the utilization of both stable and unstable nuclei in experimental programs, the tools available for study of the nucleus are greatly expanded. Direct study of 'exotic' nuclei is now possible, and their properties can be compared to those of the stable nuclei. Since existing models of the nucleus and its structure were formulated based on properties of the stable nuclei, the application of these models to 'exotic' nuclei is a very stringent test of their validity. As nuclei are produced and studied that are further and further from stability, nuclear models can be accepted, rejected, or refined to account for new data.

In addition to providing new data to test existing models, the study of exotic nuclei has also led to the discovery of features not found among naturally-occurring

nuclei. For example, because of their large β-decay energies, many nuclei far from stability have been found to decay via β-delayed particle emission. Nuclei beyond the drip lines can decay via proton or neutron emission. And in nuclei near the neutron drip line, such as ^{11}Li and ^{19}C, 'nuclear halos' have been observed. The study of these new properties can lead to a much deeper understanding of the atomic nucleus.

1.2 Nuclear Halos

As one moves from the valley of nuclear stability toward the proton or neutron dripline, the average binding energy of individual nucleons decreases. At the very limits of stability, a nucleus might have one bound state very near to the continuum. The small single-particle separation energy, combined with the short range of the nuclear force, can lead to tunneling of the nucleon far outside the normal nuclear radius. This phenomenon was first discovered in the ^{11}Li nucleus by a measurement of its interaction cross section [Ta85]. The long tail in the matter distribution leads to a greatly enhanced probability of interaction with the target nucleus, and a very large RMS radius was determined (3.27 fm). This feature of the structure of ^{11}Li was termed a 'neutron halo'. Similar structures have also been found in other nuclei near the neutron dripline [Ba95, Fu91, Ta85, Za93]

In addition to measurements of interaction cross sections, the properties of neutron halos have been studied in several ways. Experiments have been performed in which the halo is stripped from the core, and the momentum distribution of the breakup products is measured. The momentum distribution of the fragments reflects the internal momentum

distribution before the breakup, which is related by the Uncertainty Principle to the size of the original nucleus. Therefore, a very narrow momentum distribution reflects a very broad nucleus. Table 1.1 contains results from a series of measurements performed by Bazin *et al.* to study the halo nucleus ^{19}C. Momentum distributions for the breakup products of a series of carbon isotopes were measured, and the nuclear radii were extracted [Ba95]. These data show a strong enhancement in the radius of the ^{19}C nucleus, a sign of its one-neutron halo.

Table 1.1 Measured momentum distributions and extracted radii for ^{19,18,17}C performed by Bazin et al. The very narrow momentum distribution of the breakup products of ^{19}C reflect the large radius of its neutron halo.

Nucleus	Momentum Distribution FWHM (MeV/c) (lab)	Expected Radius ($R=r_0A^{1/3}$) (fm)	$\langle r^2\rangle^{1/2}$ (fm)
^{19}C	44.3	3.20	6.0 ± 0.9
^{18}C	110.3	3.14	
^{17}C	82.5	3.08	3.0 ± 0.6

Halos have been found and studied in a small number of cases near the neutron drip line. However, there has been controversy over whether or not a halo might be formed by one or more protons. Figure 1.2 shows the qualitative shapes of the nuclear potential as seen by both a proton and a neutron. In the case of a proton, the coulomb barrier is expected to keep the proton confined near the center of the nucleus. Still, for a very weakly bound proton ($S_p \approx 0$), tunneling through this barrier could be significant, and substantial proton density outside the nuclear core might be observed.

Proton binding energy is weakest near the proton dripline, which is experimentally accessible only for light nuclei. ^{8}B is therefore the lightest and most accessible

proton-halo candidate. Because of the very weak binding of its valence proton (S_p = 138 keV), and because it is experimentally accessible at radioactive beam facilities throughout the world, the ^{8}B nucleus and its structure have been the focus of much study in the last several years. A summary of these results is presented in the next section.

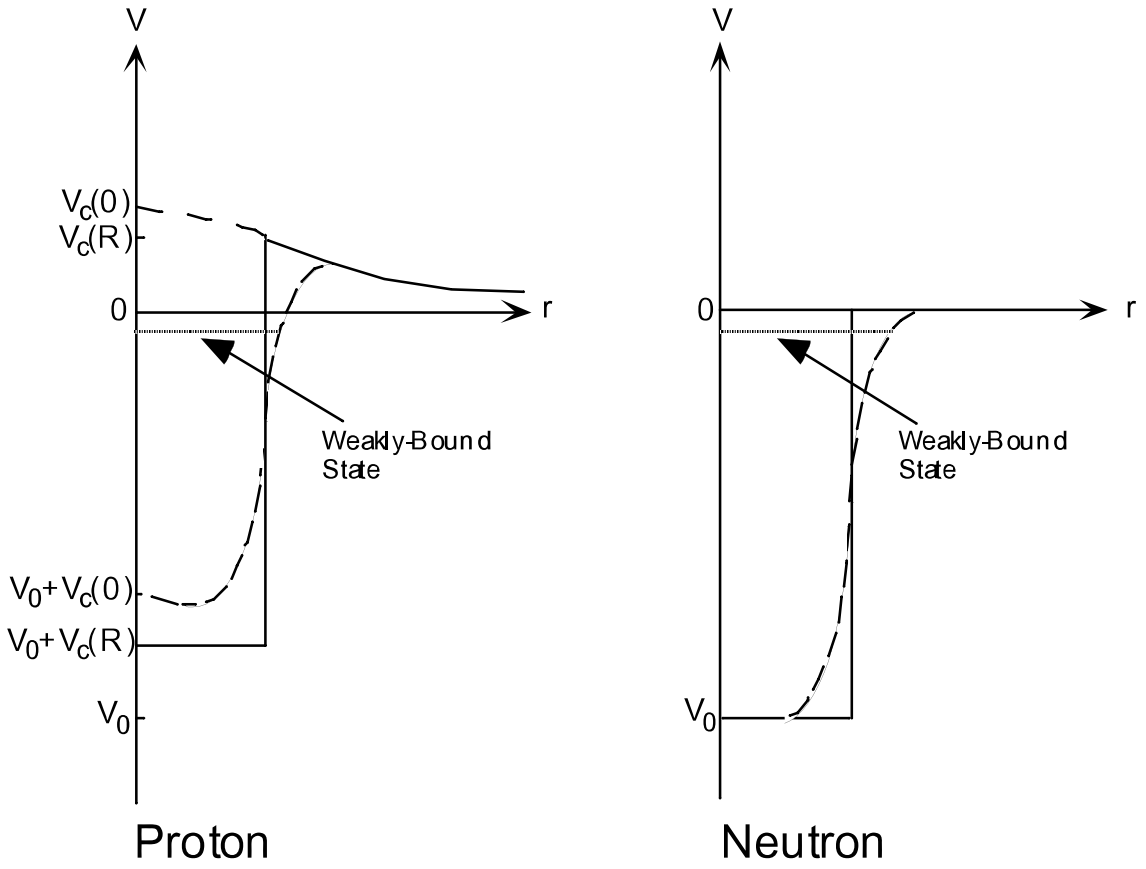

Figure 1.2 Schematic of the variation of potential energy as a function of distance from the center of a nucleus for both a proton and a neutron. The solid curves are square-well potentials, the dashed lines are Woods-Saxon potentials. V_c is the Coulomb potential inside the nucleus. Adapted from reference [Fr81].

1.3 Previous Experiments on the Exotic Nucleus ^{8}B

A number of different experiments have been performed which were designed to study the structure of the ^{8}B nucleus, and determine whether or not it exhibits a proton halo. One of the first measured ^{8}B's interaction cross section [Ta88]. The experiment found an interaction cross section very similar to those of the neighboring boron isotopes, and the deduced interaction radius followed the $A^{1/3}$ dependence typically seen in 'normal' nuclei. These results for the ^{8}B nucleus were in contrast to measured interaction radii of nuclei found to have neutron halos (which showed much larger than expected interaction radii). This early result caused many to dismiss the possibility that ^{8}B might contain a proton halo.

Another early experiment designed as a probe of the structure of ^{8}B was a measurement of the quadrupole moment [Mi92]. The quadrupole moment was found to be $|Q(8B)| = 68.3 \pm 2.1$ mb, which was anomalously large compared to shell model predictions. This large value of the quadrupole moment was interpreted by the authors as evidence for a proton halo within the ^{8}B nucleus. However, later calculations showed that E2 polarization of the ^{7}Be core by the electric field present during the experiment could enhance the quadrupole moment, and therefore the large quadrupole moment in the ^{8}B nucleus was not necessarily indicative of a proton halo [Na94].

Experiments studying the momentum distributions of the breakup products of ^{8}B were also performed in order to study its structure. The breakup of ^{8}B into ^{7}Be and a proton was studied, and the momentum distribution of the ^{7}Be products was measured.

The first such experiment was done by Schwab et al. [Sc95], and the measured momentum distribution was found to be very narrow when compared to those obtained from the breakup of ^{12}C and ^{16}O. The deduced RMS radius for the valence proton in ^{8}B of 6.83 fm was much larger than would be expected for a normally bound proton, and was thought to be a clear sign of a proton halo.

A second study of the momentum distributions of products from the breakup of ^{8}B was performed by Kelley et al. [Ke96] In this experiment, the measured momentum distribution of the ^{7}Be fragments was found to be similar to that obtained by Schwab et al., but after accounting for absorption by the ^{7}Be core, they deduced an RMS radius for the valence proton in ^{8}B of 4.24 fm. Though this radius is larger than the systematic behavior of nuclear radii ($r_0A^{1/3} \approx 2.5$ fm), it is much smaller than the RMS halo radius observed for the neutron halo nucleus ^{11}Li of 6.2 fm [Or92]. These results were interpreted as evidence against a large proton halo in ^{8}B.

A study of quasi-elastic scattering of ^{8}B from ^{12}C was performed with the goal of studying the structure of ^{8}B [Pe95]. The measured scattering cross sections were fitted using Optical Model potentials, and the matter distribution determined. The deduced RMS matter radius of 2.207 fm for the ^{8}B nucleus was small, and the authors interpreted this as evidence against a substantial proton halo in ^{8}B.

Table 1.2 summarizes the RMS radii of ^{8}B determined using several different experimental techniques. Because of the large discrepancies among these values, and the uncertainty they brought to the question of ^{8}B's structure, we performed a new experimental study of the ^{8}B nucleus.

Table 1.2 RMS Radii of the ^{8}B nucleus from several experiments.

Reference	Experimental Method	^{8}B $\langle r^2 \rangle^{1/2}$	^{7}Be core $\langle r^2 \rangle^{1/2}$	valence proton $\langle r^2 \rangle^{1/2}$
Ta88	Interaction σ	2.38 ± 0.04		
Wa95	Total Reaction σ	2.72		
Mi92	Quadrupole Moment	2.98		
Sc95	Breakup p-distribution	2.78		6.83
Ke96	Breakup p-distribution		2.39	4.24

1.4 Purpose of the Present Work

The goal of the present work is to study the structure of the ^{8}B nucleus. Given the discrepancies among the results of previous work, we chose a different experimental approach to the problem: the use of a single-nucleon transfer reaction as a probe of ^{8}B's structure. Such nucleon transfer reactions are a very powerful probe of the structure of the product nucleus, and have been used for many years in the study of nuclear structure. The transfer of a single nucleon probes the single-particle states of the product nucleus, and measurement of the transfer reaction's cross section over a range of angles can reveal a great deal about the single-particle wave functions. Such a measurement can determine the angular momentum transfer and thus the spin quantum numbers, the energies of the single-particle orbits, and a measure of the nuclear radius. In addition, since the single-particle wave functions are one component of the total final-state wave function, information about the final-state wave function can also be determined [Fe92].

A traditional study of the valence proton state of ^{8}B would use a ^{7}Be target, and the reaction transferring a proton from projectile to target to form ^{8}B would be studied. However, with ^{7}Be's somewhat short half-life (53 days), production of such a target would be difficult. If instead we produce a beam of ^{7}Be and use a deuterium target, the study of this reaction becomes more tractable. Modern radioactive beam facilities allow studies of a variety of such reactions in inverse kinematics.

For the present work, we chose the reaction d(^{7}Be,^{8}B)n. This reaction transfers a single proton from deuterium to ^{7}Be, forming ^{8}B. The reaction probes the proton single-particle states in the ^{8}B nucleus, and measurement of the reaction cross section over a range of angles gives information about these states. In this way, the wave function of the ^{8}B ground state can be determined, and its structure understood. Our goal, then, is to produce the d(^{7}Be,^{8}B)n reaction, measure its cross section over a range of angles, and analyze the measured cross section to determine the implications for the structure of ^{8}B.

Another study of d(^{7}Be,^{8}B)n at a much lower bombarding energy ($E_{^{7}Be}$= 26 MeV) has recently been published by Liu et al. [Li96]. The focus of their work was not to study the structure of ^{8}B, but rather to measure the astrophysical $S_{17}(0)$ factor for the ^{7}Be(p,γ)^{8}B reaction. The value of $S_{17}(0)$ plays an important role in the solar neutrino problem, since the ^{7}Be(p,γ)^{8}B reaction is the source of the high energy neutrinos measured [Ba92]. It has been previously shown by Xu *et al.* that the proton-pickup reaction of ^{7}Be at low energies can be used to measure $S_{17}(0)$ [Xu94]. Liu *et al.* obtained a value of $S_{17}(0) = 27.4 \pm 4.4$ eV b, which is significantly higher than the currently accepted value of $S_{17}(0) = 19\ ^{+4}_{-2}$ eV b [IN97]. As a secondary goal, our work will attempt to use the measurement of

the d(^{7}Be,^{8}B)n reaction cross section to determine the astrophysical $S_{17}(0)$ factor for the ^{7}Be(p,γ)^{8}B reaction using the method described by Xu *et al.* However, there is a general loss of sensitivity to the value of $S_{17}(0)$ at higher bombarding energies because the nuclei penetrate more deeply into one another. For this reason, our work is likely to be more sensitive to the internal structure of ^{8}B than to reactions at the surface of the nucleus.

Chapter 2

Experimental Equipment

This study of d(^{7}Be,^{8}B)n consisted of two experiments which took place at the National Superconducting Cyclotron Laboratory (NSCL) at Michigan State University. NSCL Experiment 93045 took place in June 1995, and was an exploratory test of the techniques and detector systems used to make a measurement of a reaction cross section in inverse kinematics. This experiment was followed in July 1996 by NSCL Experiment 96019, which built upon the results of 93045, and improved upon the shortcomings of the first.

In order to make the best possible measurement of the reaction cross section, an array of detectors was assembled to observe *both* products of the (d,n) reaction. In this way, two measurements of the cross section are obtained, one from the number of ^{8}B products, and one from the number of neutrons in coincidence with ^{8}B. The observation of both products in kinematic coincidence (at the correct angles and energies) is the strongest possible test that the desired transfer reaction took place. Agreement between these two measures would indicate proper handling of systematic corrections, while the redundant measurements decrease statistical uncertainties.

This chapter describes the experimental equipment used to make the coincidence measurement of the d(^{7}Be,^{8}B)n reaction in inverse kinematics. This includes the production of the ^{7}Be beam, and several detector components to identify the products of the (d,n) reaction. These are detailed in the following sections.

2.1 The A1200 Fragment Separator

Prior to the development of radioactive beam facilities, study of the d(^{7}Be,^{8}B)n reaction was extremely difficult. However, with today's fragment separators the reaction can be performed in 'inverse' kinematics, using ^{7}Be as the beam and deuterium as the target. In studies of the (d,n) reaction, inverse kinematics actually has many advantages over 'normal' kinematics. In inverse kinematics, the heavy product has enough kinetic energy to exit even a moderately thick target, and the neutron is moving slowly enough to allow a high probability for its detection. In contrast, normal kinematics (energetic deuteron and heavy target) would leave the heavy product trapped in all but the thinnest targets, and eject an energetic (thus difficult to detect) neutron.

In this study, the energetic ^{7}Be beam was produced in the A1200 Fragment Separator at the National Superconducting Cyclotron Laboratory operating in momentum-loss achromat mode [Sh91]. Figure 2.1 shows the schematic design of this device. A 60 MeV/A ^{12}C beam from the K1200 Cyclotron was focussed onto a 587 mg/cm^{2} ^{9}Be target placed at the medium acceptance target position. The target thickness was chosen to optimize production of ^{7}Be. The fragmentation products of the collision between beam and target were separated on the basis of A/Z by the first dipole pair of the

A1200, which were set to maximize the transmission of ^{7}Be ($B\rho_1$=1.567). The beam then passed through an achromatic 425 mg/cm^2 Al wedge, producing a momentum shift described by the energy loss relation of Bethe:

$$\frac{dE}{dx} = \frac{AZ}{E}$$

This momentum shift gives each isotope a distinct A, Z, and E, allowing relatively unambiguous separation in the final pair of dipoles ($B\rho_2$=1.279). In this work, the primary beam current was typically ~400 nA $^{12}C^{3+}$ (133 pnA) using the ECR ion source. This produced a ^{7}Be count rate in the N3 vault of ~335,000 s^{-1}. This beam consisted of ~96% ^{7}Be and ~4% ^{8}B impurity. Several other secondary beams were produced during NSCL experiments 93045 and 96019 for reference measurements and calibrations. Their production is summarized in Table 2.1

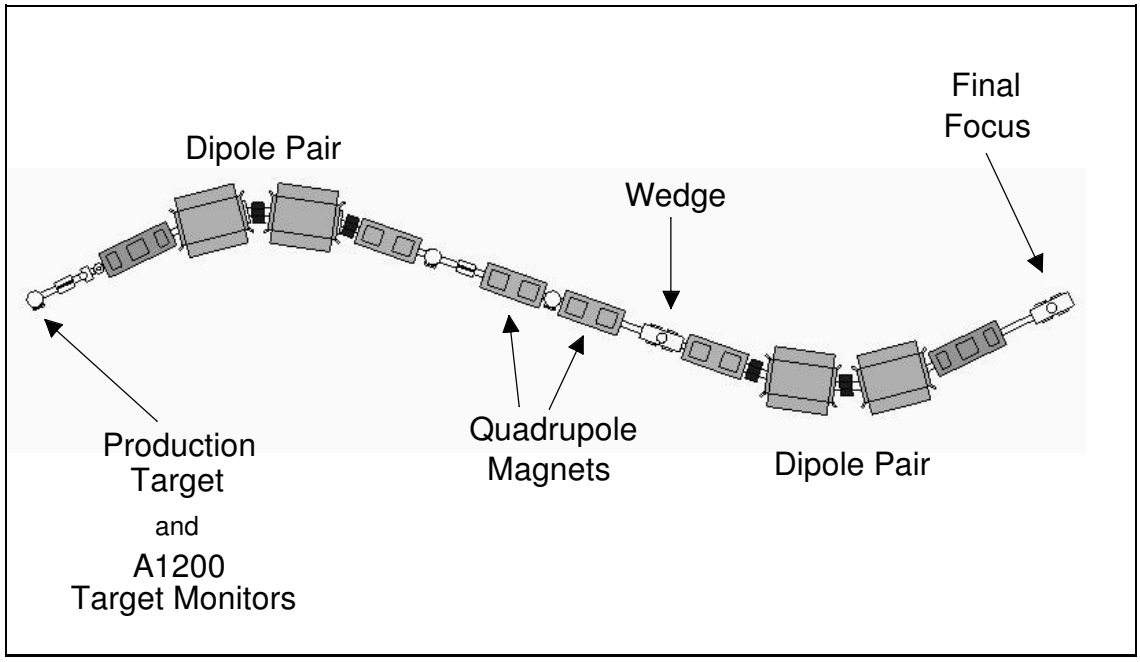

Figure 2.1 The A1200 Fragment Separator.

Table 2.1 Secondary beams from the A1200 and their production. These results are a summary of measurements made in NSCL Experiments 93045 and 96019.

	^{17}N @ 25 MeV/A	^{12}C @ 21 MeV/A	^{7}Be @ 25 MeV/A
Primary Beam	^{18}O @ 60 MeV/A	^{12}C @ 60 MeV/A	^{12}C @ 60 MeV/A
Primary Current		133 pnA	133 pnA
Production Target	587 mg/cm^2 ^{9}Be	790 mg/cm^2 ^{9}Be	587 mg/cm^2 ^{9}Be
Bρ_1	2.24	1.71	1.57
Wedge	425 mg/cm^2 Al	300 mg/cm^2 Al	425 mg/cm^2 Al
Bρ_2	1.75	1.34	1.28
Secondary Beam Rate	1.5×10^3 s^{-1}	8×10^5 s^{-1}	3.4×10^5 s^{-1}
Beam Composition	100 % ^{17}N	100 % ^{12}C	96 % ^{7}Be, 4% ^{8}B

2.2 Detectors for the Study of (d,n) in Inverse Kinematics

In order to perform the coincidence measurement of the (d,n) reaction in inverse kinematics, a diverse array of detector systems was needed. The detector array had to identify the particles, and measure their energy and angle of emission. Figure 2.2 shows a schematic of the detectors used for the study of d(^{7}Be,^{8}B)n in Experiment 96019. The laboratory and center-of-mass angles of these detectors are reported in Tables 2.2 and 2.3 for NSCL Experiments 93045 and 96019, respectively. These detector arrays consisted of three major components: target ladder, heavy fragment detectors, and neutron detectors. Each of these is detailed in the following sections.

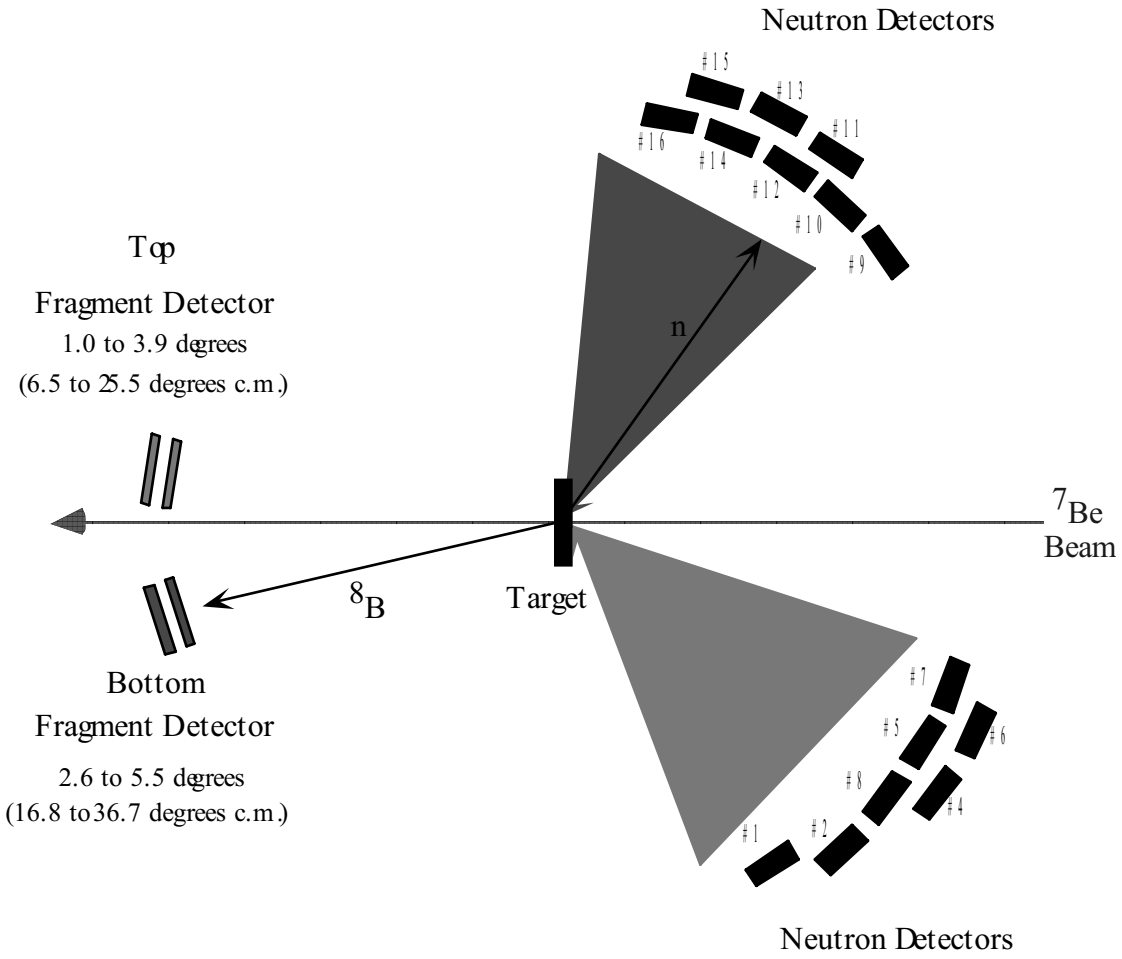

Figure 2.2 Side view of detectors used in Experiment 96019. The figure shows the neutron detector numbering scheme and their positions. Also shown is the angular coverage of the fragment telescopes in the lab and center-of-mass frame. The exact angles of all detectors are given in Table 2.3. The triangles show the allowed angular range for neutrons in kinematic coincidence. If a ^{8}B hits the Bottom Fragment Detector, the coincidence neutron is emitted at an angle within the triangle above the beam axis.

Table 2.2 Detector placement for experiment 93045. Note that the neutron detectors subtend 4.35 degrees in the lab frame.

Detector	Lab Angle	CM Angle for d(^{7}Be,^{8}B)n @ 25 MeV/u
Top Fragment	2.0° - 4.5°	20° - 48°
Bottom Fragment	2.0° - 4.5°	20° - 48°
Neutron 12	121.5°	22.7°
Neutron 13	112.5°	28.1°
Neutron 14	103.5°	34.5°

Table 2.3 Detector placement for experiment 96019. Note that the neutron detectors subtend 4.35 degrees in the lab frame.

Detector	Lab Angle	CM Angle for d(^{7}Be,^{8}B)n
Top Fragment	1.0° - 3.9°	7° - 25°
Bottom Fragment	2.6° - 5.5°	18° - 36°
Neutron 1	121.5°	23°
Neutron 2	130.5°	18°
Neutron 4	144°	12°
Neutron 5	148.5°	11°
Neutron 6	153°	9°
Neutron 7	157.5°	7°
Neutron 8	139.5°	14°
Neutron 10	130.5°	18°
Neutron 11	126°	20°
Neutron 12	121.5°	23°
Neutron 13	117°	25°
Neutron 14	112.5°	28°
Neutron 15	108°	31°
Neutron 16	103.5°	35°

2.2.1 Target Ladder

The target ladder at the center of the detector array was used to position various devices in the path of the incoming beam. Devices mounted on the ladder included two targets (reaction and background), a beam normalization detector, and a beam-stopping scintillator.

The reaction target was an 18 mg/cm^2 deuterated polyethylene (CD_2) foil, made at the NSCL from commercially available enriched polyethylene. Details of the fabrication process can be found in Appendix A. The background target was a 31 mg/cm^2 carbon foil, used to subtract any effect of the carbon atoms in the CD_2 target from the measured reaction cross section.

The Beam Normalization Detector consisted of a 500 μm silicon diode masked by an aluminum target frame thick enough to stop the beam, making the active area the same size and shape as the reaction and background targets. During several runs over the course of the experiment, this detector was inserted into the path of the incoming beam to measure beam intensity. This intensity measurement was used to calibrate and monitor the response of the A1200 Target Monitors (see Figure 2.1), which continuously measured the primary beam intensity. With this proportionality, the A1200 Target Monitors gave a continuous measure of the flux at the reaction target. Because the beam normalization detector was a silicon diode, its response could be used to measure the energy loss of the ions passing through it. In this way, the identity of the beam

components was determined, and the beam purity at the reaction target was also measured.

The beam-stopping scintillator consisted of a fast-plastic scintillator (BC412) 3mm thick, 25mm × 20mm in area, mounted between two Hammamatsu photomultiplier tubes (H3167). It was used to stop a beam of ^{17}N from the A1200 and to count betas from its beta-delayed neutron decay. The neutrons emitted after the beta decay of ^{17}N were used to calibrate the detection efficiency of the NSCL Neutron Array. The neutron array is described in section 2.2.3, and the calibration procedure is detailed in section 3.2.1.

2.2.2 Heavy Fragment Detectors

The heavy fragment detectors were designed to identify and to measure the angle and energy of the heavy product of the (d,n) reaction. Two different systems were used to accomplish this in experiments 93045 and 96019.

For the first experiment (93045), the heavy fragment detectors consisted of a Parallel-Plate Avalanche Counter (PPAC) and a pair of silicon diodes. A PPAC is a gas-filled, position-sensitive counter that was used to determine the angle of the outgoing fragment; its design is described in [Sw94]. Behind the PPAC were two silicon diodes, each 500 μm thick. The first silicon diode measured the energy loss of the ion in the fixed thickness of the detector, the second stopped the ion to measure its remaining kinetic energy. This measure of ΔE-E allowed unique identification of the penetrating ion, along with its kinetic energy. Unfortunately, the PPACs proved to be inefficient at detecting the

high-energy, low-charge ions used in this experiment, and the angles of the reaction products could not be accurately determined. The shortcomings of this detector system are discussed more fully in Section 3.1.

For the second experiment (96019), the heavy fragment detectors were changed to overcome limitations of the PPACs. The new fragment telescopes consisted of a 5 × 5 cm^2 double-sided silicon-strip detector placed 100 cm from the reaction target, followed by a 5 × 5 cm^2 stopping silicon diode. The silicon strip detector is coated with conducting stripes, dividing the detector into 16 horizontal strips on the front surface, and 16 vertical strips on the back surface, which in effect, divides the detector into 256 pixels. Each of the strips is connected to its own channel of linear electronics. Ionization from a particle passing through any point on the detector will be collected primarily by one horizontal strip on the front, and one vertical strip on the back. In this way, the position and ΔE of the ion can be determined by the strip detector. The remaining kinetic energy of the ion is deposited in the stopping silicon diode, allowing the identity and energy of the ion to be determined.

The first element of the Top Fragment Detector was a 500 μm thick silicon-strip detector, specially manufactured with a supporting frame surrounding only 3 sides of the detector. On the fourth side, the active area extended to the edge of the detector, allowing its placement very near to the beam axis. Behind this strip detector was a 500 μm silicon diode. The Bottom Fragment Detector consisted of a 300 μm silicon-strip detector followed by a pair of 500 μm silicon diodes.

In order to decrease statistical uncertainties, the data from pixels with similar angles from the beam axis were combined offline. This formed 16 pixel *groups* in each of the top and bottom detectors. The grouping of pixels is illustrated in Figure 2.3

A schematic of the electronics used for the fragment detector data acquisition is shown in Figure 2.4.

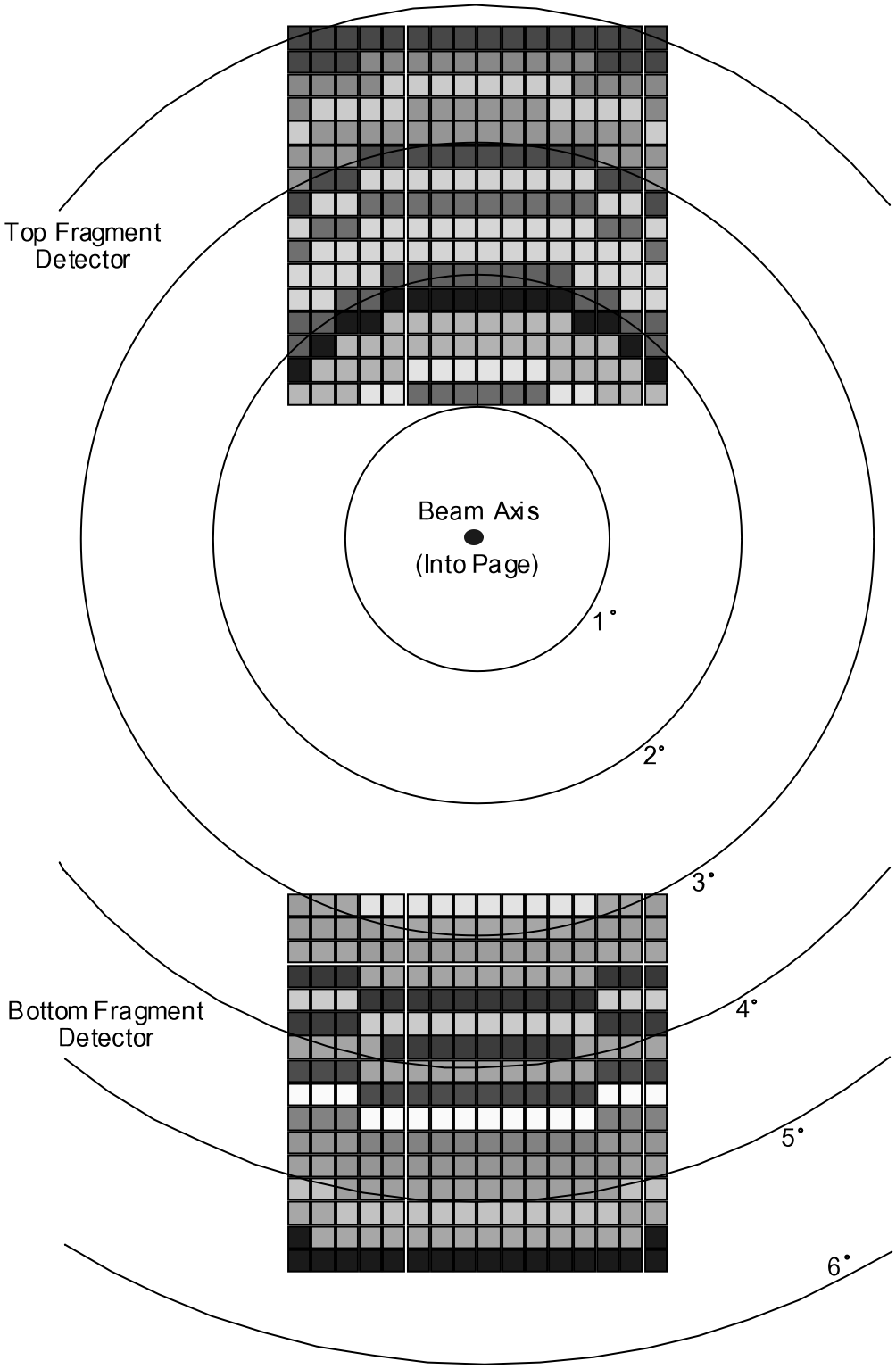

Figure 2.3 Beam view of the Heavy Fragment Detectors. Each of the two detectors is divided into 16 different pixel groups based on the lab angle of the pixel. In this figure, different colors indicate the different pixel groups. In the remainder of this document, these groups are referred to as Groups Top 1-16 and Bottom 1-16.

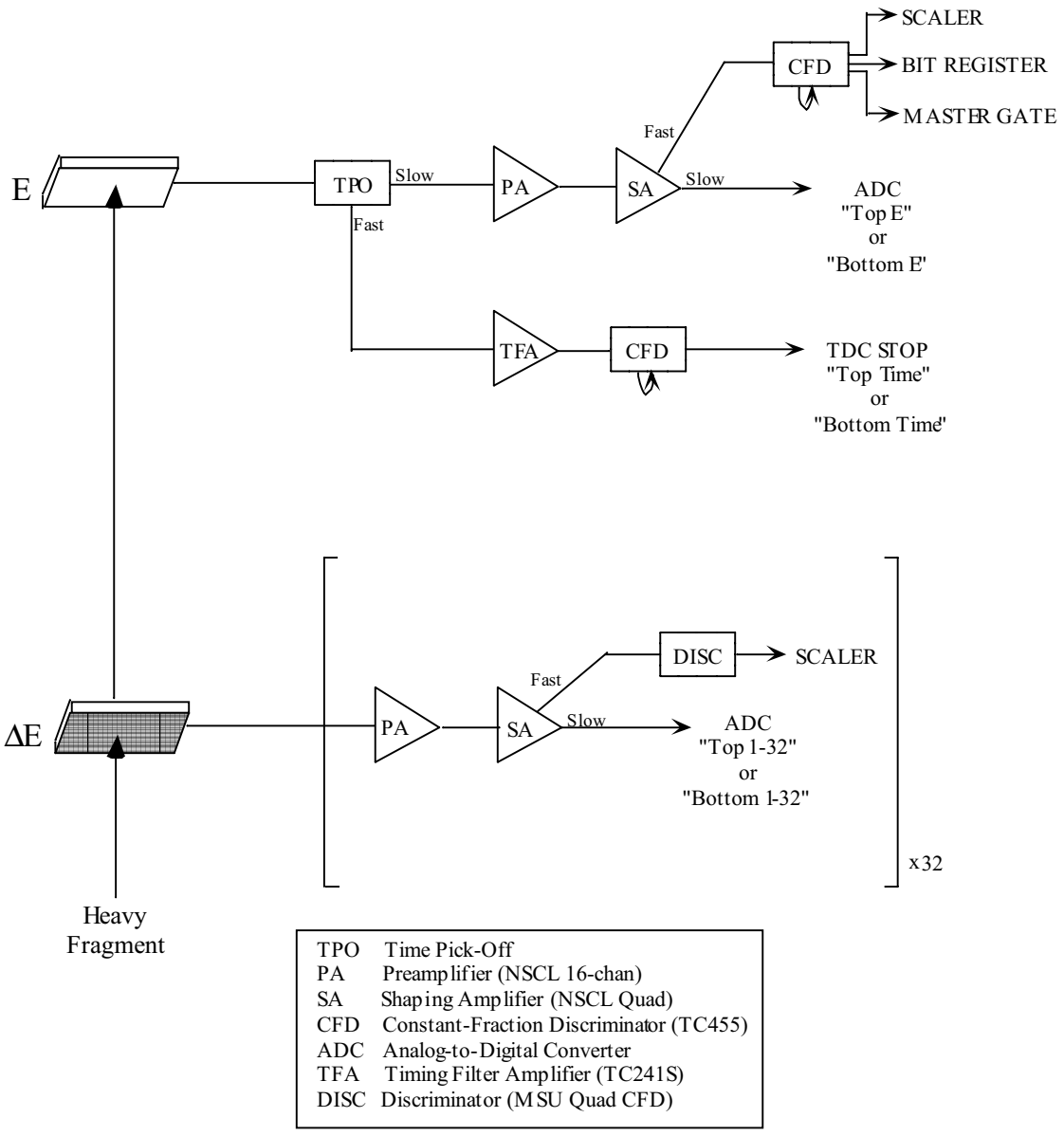

Figure 2.4 Schematic of the data acquisition electronics for the Fragment Detectors used in experiment 96019. This schematic represents the setup for both the Fragment Detector *above* the beam axis ("Top") and the Fragment Detector *below* the beam axis ("Bottom").

2.2.3 Neutron Detector Array

In order to measure the angle and energy of the neutron products of the d,n reaction, the NSCL Neutron Time-of-Flight Array was positioned at backward angles. This neutron detection system is described in detail in [Ha92]. The array consisted of 16 bars of scintillating fast-plastic (BC412) 157 cm × 7.6 cm × 2.54 cm. The bars are bent with a one meter radius of curvature to enable an equal flight path from the target to all points along the detector. Each scintillator bar was read out by two photomultiplier tubes (Thorn EMI 9821), one at each end. The calculated mean time from the two photomultiplier tubes (PMTs) served as the stop signal for the neutron time-of-flight, while the time difference between the two PMT signals allowed the determination of the position of the neutron's interaction along the length of the detector. With the bars positioned one meter from the reaction target, each bar subtended a solid angle of 119.3 msr.

The Neutron TOF Array was designed to be used at atmospheric pressure, and the requirements of the (d,n) coincidence experiment called for it to be placed inside the 92" chamber under vacuum. This presented several problems. First, the PMT bases contained electrolytic capacitors that can fail under vacuum. These capacitors were replaced with ceramic disks in all 32 PMT bases. Second, under vacuum the lack of convection might heat the PMTs to high temperatures, causing instability in their photocathodes and dynodes. To prevent this problem, the equilibrium operating temperature of the PMT bases was measured at a test station under various conditions.

Figure 2.5 shows the PMT base temperature as a function of the elapsed time after voltage was applied. The equilibrium temperature of the base at atmospheric pressure and ambient temperature was determined to be ~28 °C. Under vacuum, this rose to ~34.5 °C. After connection of a heat sink to the base, this temperature decreased to ~31 °C. In Experiments 93045 and 96019, a steel strap (~50 cm long) was used to connect each PMT base to the aluminum support structure to serve as a heat sink. The temperature of one of the PMT bases (#16) was monitored throughout the experiment, and averaged ~26 °C in this configuration.

An unexpected problem with high-voltage connections was discovered in Experiment 96019. The tight-fitting SHV electrical connectors trapped a volume of gas inside the connector which slowly leaked out under vacuum. Sparking was observed inside these connectors, and voltage could not be applied to the detectors until the connectors were allowed to outgas.

A schematic diagram of the electronics used for the neutron detector data acquisition is shown in Figure 2.6.

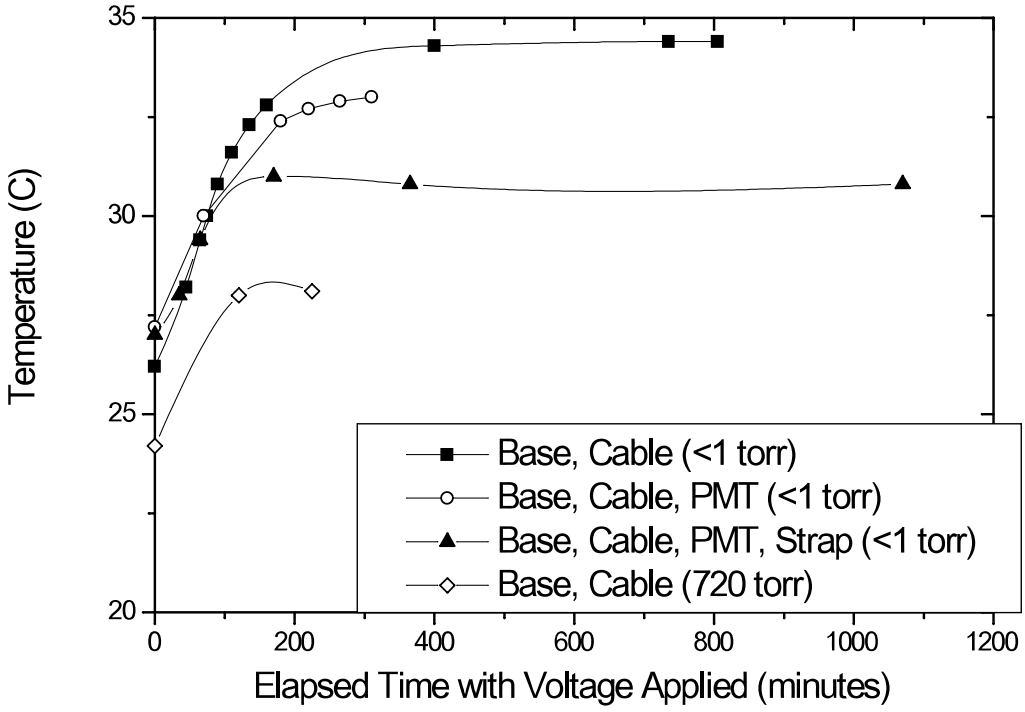

Figure 2.5 Temperature of the PMT base in several configurations as a function of time.

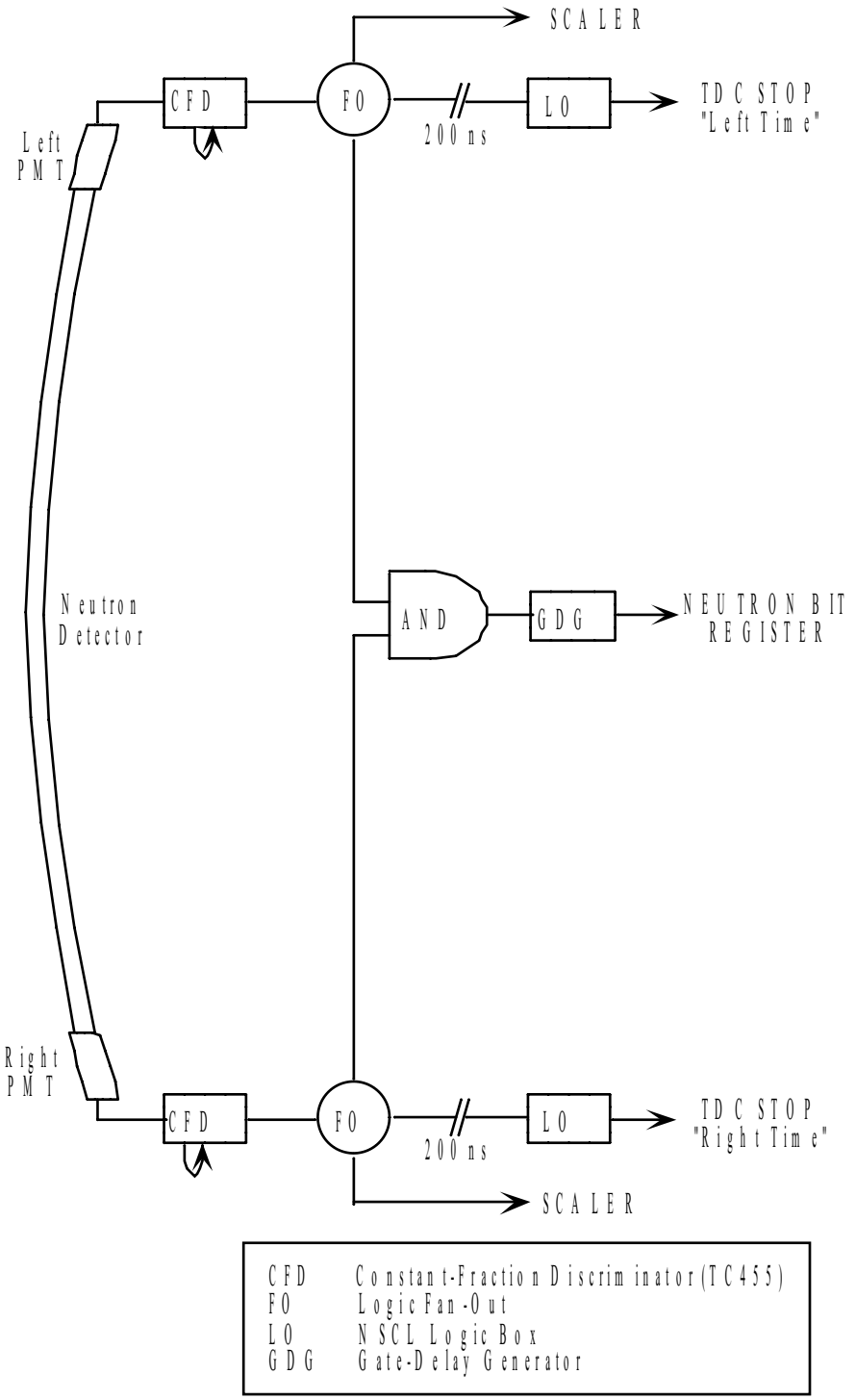

Figure 2.6 Schematic of the data acquisition electronics used for each of the 16 Neutron Detectors in experiment 96019.

Chapter 3

Results and Analysis

In order to make a reliable measurement of the d(^{7}Be,^{8}B)n cross section, several preliminary calibrations needed to be made. These include TOF calibrations, beam flux calibrations, and neutron detection efficiency calibrations. Once these measurements were made, we decided to make a measurement of another (d,n) reaction: d(^{12}C,^{13}N)n. This is a transfer reaction whose cross section has been measured previously [Pe72, Sc84, Be93], and involves nuclei which have been studied extensively. The measurement of d(^{12}C,^{13}N)n serves as a proof-of-concept; if the cross section we measure agrees with previous works, it will lend validity to our measurement of d(^{7}Be,^{8}B)n.

Experiments 93045 and 96019 were performed in several parts. First, calibrations of the detector systems were made. This was followed by the measurement of d(^{12}C,^{13}N)n, and then by the study of d(^{7}Be,^{8}B)n. Section 3.1 details this process for Experiment 93045, while Section 3.2 describes Experiment 96019.

3.1 NSCL Experiment 93045

NSCL Experiment 93045 was our first attempt to study the d(^{7}Be,^{8}B)n reaction. The experiment was also the first of its kind, attempting to make a coincidence measurement of a reaction cross section using a radioactive beam. The experiment was performed in June 1995, and consisted of 120 hours of K1200 primary beam time which was divided into several parts, each of which are described in the following sections.

3.1.1 TDC Calibrations

In order to make time-of-flight (TOF) measurements of the neutron kinetic energy, it was necessary to calibrate the response of all Time-to-Digital Converter (TDC) channels used in the experiment. This was done using an Ortec 462 Time Calibrator, a NIM electronics module that outputs electronic pulses at fixed time intervals. The 'start' pulse was directed into the common TOF START, and the 'stop' pulses were input to each of the 32 TDC channels used to determine the neutron TOF. A sample time spectrum for this calibration is shown in Figure 3.1. By measuring the channel number of each peak, and fitting it to the known elapsed time, the number of channels per nanosecond is determined. All 32 TDC channels were found to be quite linear and quite similar, with an average of 2.9773 channels/ns for a 512 channel histogram, with an average uncertainty of 0.0008 channels/ns.

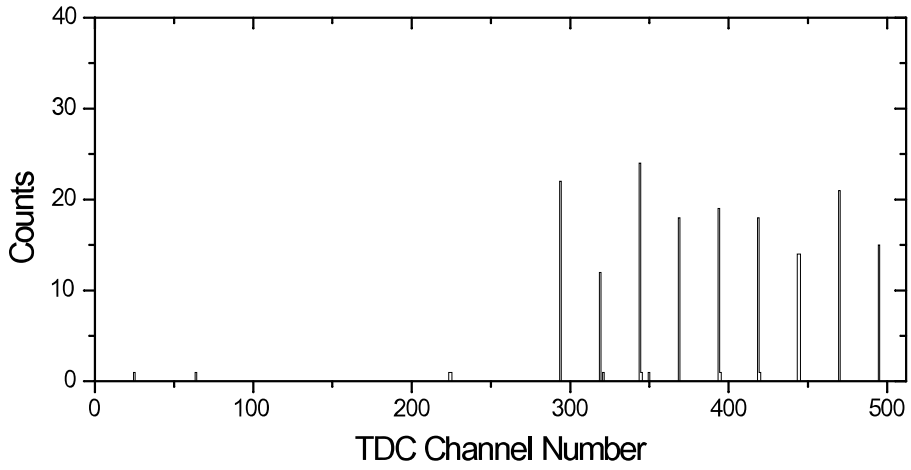

Figure 3.1 Time Calibration of TDC channel for Neutron Detector 2. Time between peaks is known to be 10 ns, TDC is set at 200 ns full scale.

3.1.2 Measurement of the Neutron Detection Efficiency

The detection efficiency of the NSCL Neutron Array is strongly dependent upon the readout electronics. It is therefore necessary to calibrate the neutron detection efficiency for every new application. This calibration utilized the well-studied beta-delayed neutron decay of ^{17}N as the calibration standard, a process described in detail in [Sc93].

^{17}N β^- decays to one of several neutron-unbound states of ^{17}O with known branching ratios. The strongest of these states emit neutrons with kinetic energies of 1.689, 1.161, and 0.384 MeV. A schematic of this beta-delayed neutron decay is shown in Figure 3.2. An efficiency calibration is obtained by counting the total number of ^{17}N decays, and the neutrons detected at each energy. Figure 3.3 shows a schematic of this measurement and the associated detectors.

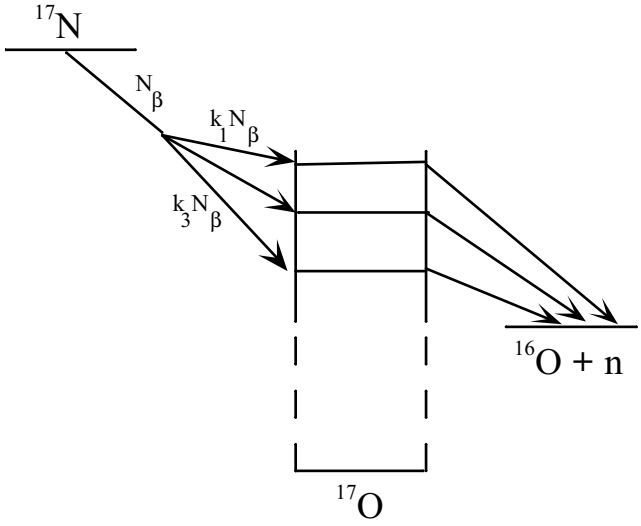

Figure 3.2 Schematic of the beta-delayed neutron decay of ^{17}N.

In order to make the ^{17}N decay measurement, the primary beam from the K1200 cyclotron was cycled on and off. The electronic setup for this procedure is identical to that used by Harkewicz, and a schematic can be found in [Ha92]. During BEAM ON cycles (~4 seconds), a beam of ^{17}N @ 25 MeV/A produced in the A1200 Fragment Separator was implanted into the beam-stopping scintillator at the target position. During the BEAM OFF cycles (~8 seconds), the beta-delayed neutron decay of the implanted nuclei was observed ($t_{1/2}$ = 4.17s). The emitted β^- was detected in the beam-stopping scintillator, serving as a count of the number of decays (N_β) and also as the START signal for a neutron time-of-flight (TOF) measurement. A spectrum of light-output from this detector is shown in Figure 3.4. After the beta decay of ^{17}N, the unbound ^{17}O daughter

immediately emitted a neutron. If this neutron interacted with one of the neutron detectors, the time signal from the detector served as the neutron TOF STOP, with the elapsed time serving as a measure of the neutron energy. Figure 3.5 shows a sample neutron time-of-flight spectrum from one of the neutron detectors (Detector #9). Peaks corresponding to neutrons with energies of 1.689 and 1.161 MeV are clearly separated, and their integration counts the number of detected neutrons at each energy (N_n). The intrinsic neutron detection efficiency ε_{int} is given for each energy by:

$$\varepsilon_{int} = \frac{N_n}{N_\beta \ni BR \ni \varepsilon_{geom}}$$

where ε_{geom} is the geometric efficiency of the detector, and BR is the branching ratio to the neutron-unbound state. Table 3.1 gives the areas of the neutron peaks from Figure 3.5, the branching ratios, and the corresponding detection efficiencies.

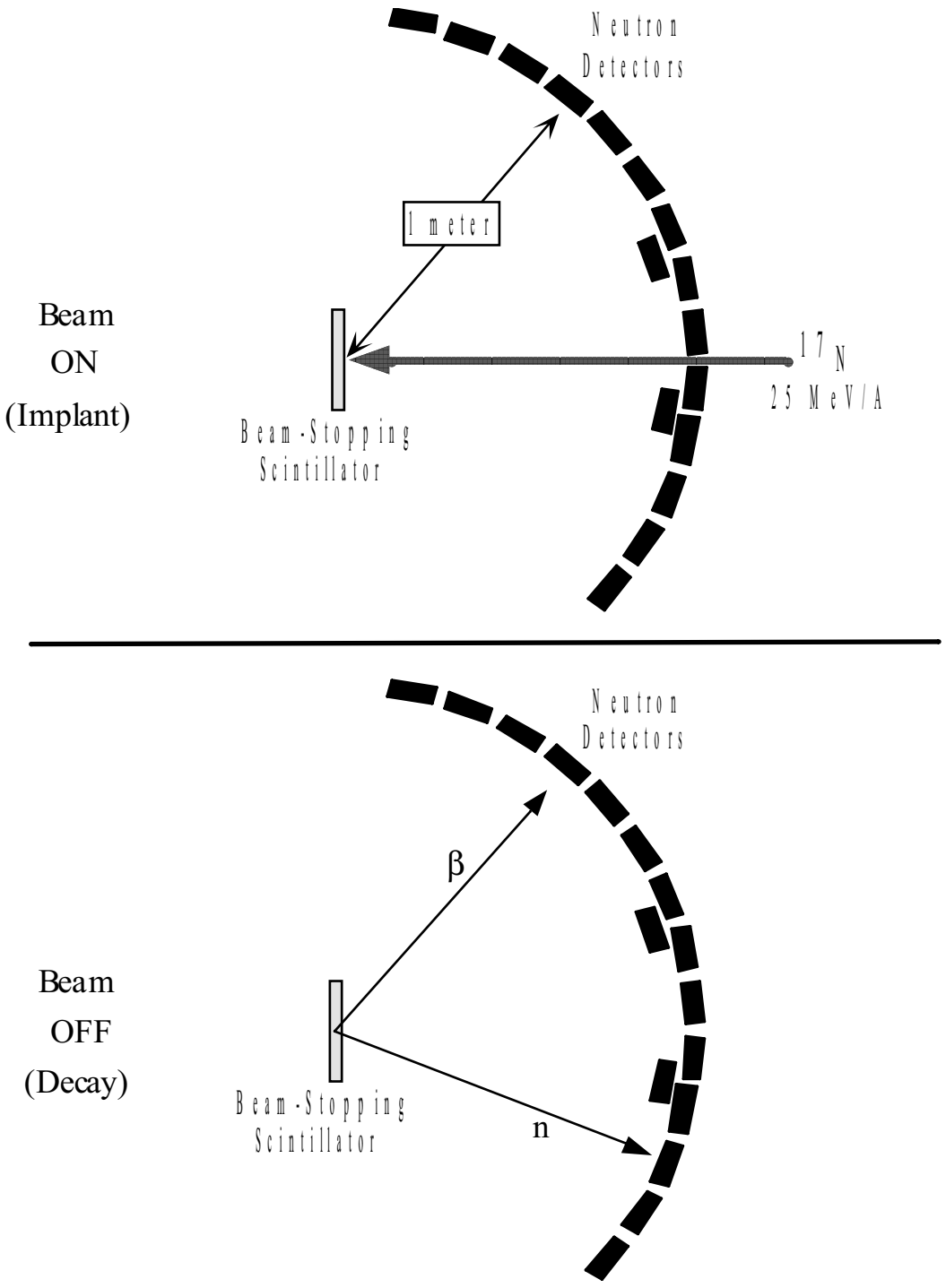

Figure 3.3 Side view of the neutron detector efficiency calibration using the beta-delayed neutron decay of ^{17}N.

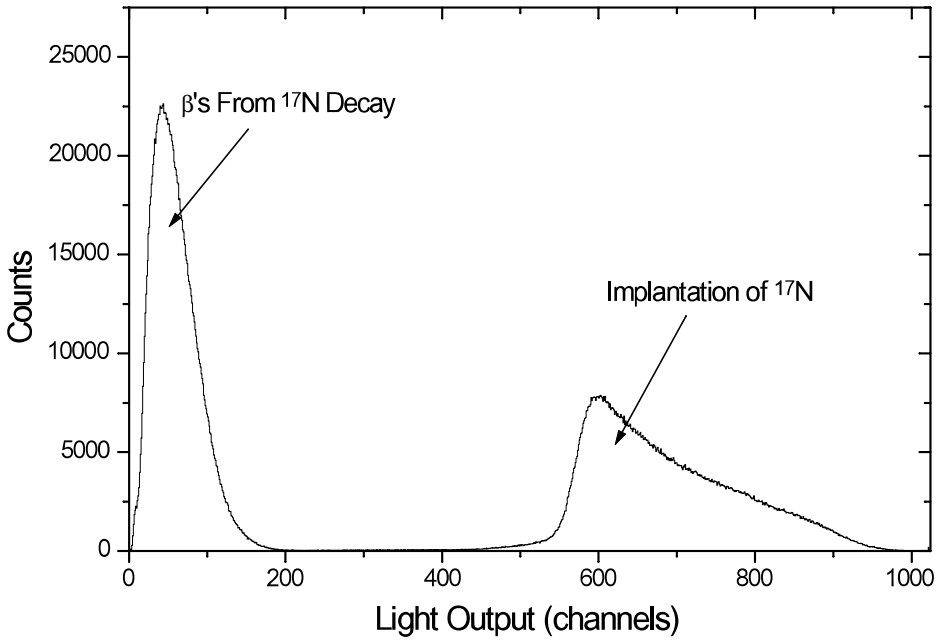

Figure 3.4 Light output from Beam-Stopping Scintillator. Spectrum shows events collected during both BEAM ON and BEAM OFF cycles. Integration of the β peak determines the number of ^{17}N decays observed ($N_\beta = 1.57 \times 10^6 \pm 2 \times 10^4$).

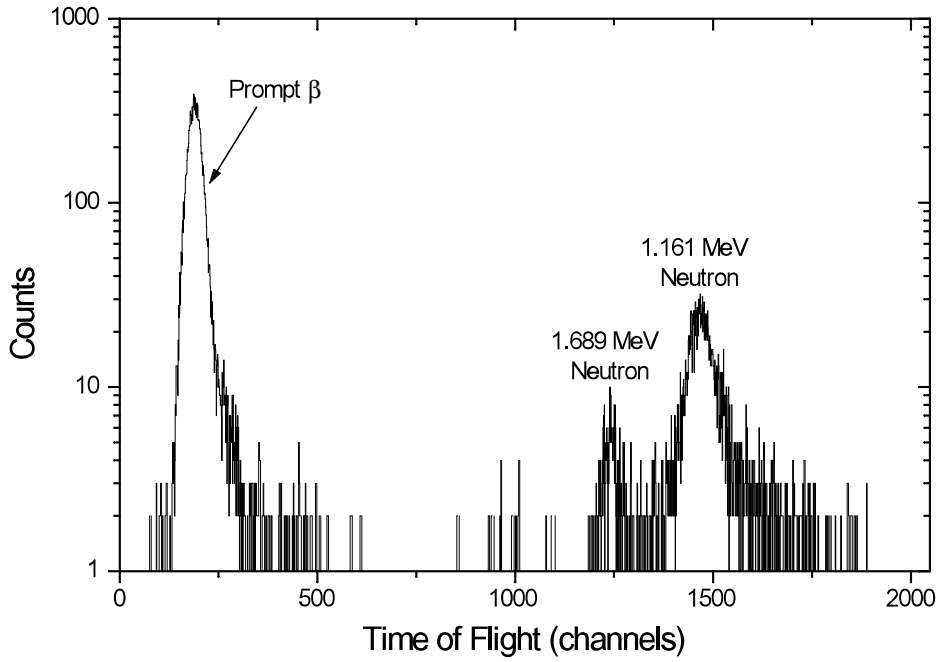

Figure 3.5 Typical time-of-flight spectrum from β-delayed neutron decay of ^{17}N. Prompt beta peak at known energy determines time of decay, areas of neutron peaks determine detection efficiency at each energy.

Table 3.1 Detection efficiencies for neutron detector number 9. From the measured N_β and N_n, and the known branching ratios and geometric efficiency, the intrinsic efficiency is determined.

Neutron Energy	Branching Ratio (%)	Neutron Counts	Geometric Efficiency	Detection Efficiency
1.689	6.9	311 ± 17	0.00949	0.302 ± 0.007
1.161	50.1	2080 ± 42	0.00949	0.28 ± 0.01

Measuring the decay of ^{17}N allows the determination of the neutron detection efficiency at neutron energies of 1.689 and 1.161 MeV. However, in the study of the d(^{7}Be,^{8}B)n reaction at 25 MeV/A, the neutrons to be measured ranged in energy from ~3.5 MeV to ~12 MeV. It was necessary to extend the measured efficiencies to higher energies. This was done using a Monte Carlo calculation [Ce79] of the neutron detectors, and scaling the results to the measured data. This extension of the measured neutron efficiencies to higher energies was performed by Harkewicz, and was shown to give good agreement between calculated and measured efficiencies [Ha92].

Figure 3.6 shows the dependence of the neutron detector efficiency on neutron energy for neutron detector #9. Measured efficiencies determined from the decay of ^{17}N are plotted, along with the results of the Monte Carlo calculation which were scaled to match the measured values. The fit to these points was used for calculation of neutron detection efficiency at arbitrary energies.

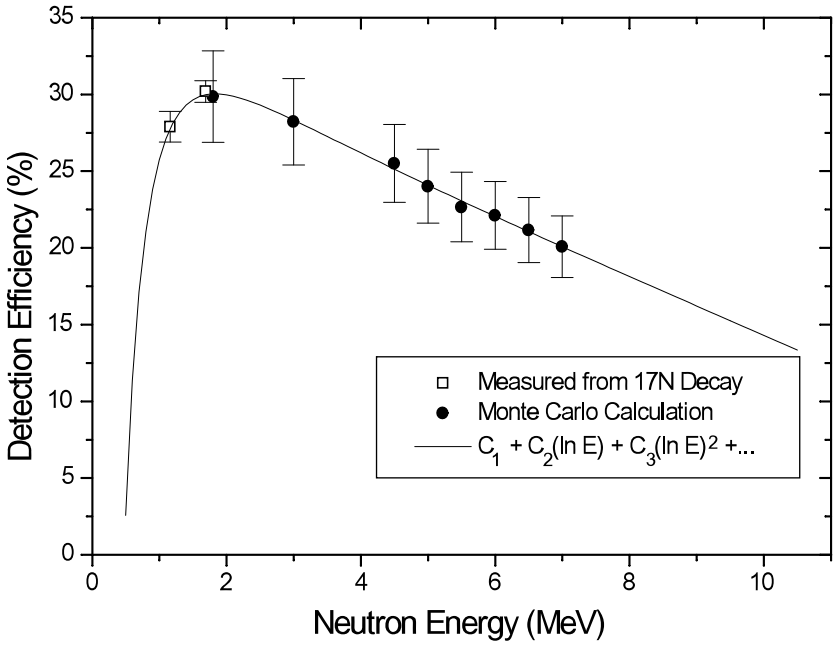

Figure 3.6 Neutron detection efficiency curve for neutron detector #9. Data measured using the decay of ^{17}N, along with Monte Carlo results scaled by 1.357, are plotted. The fit to these points is used to determine detection efficiency at arbitrary neutron energies.

3.1.3 Determination of the Neutron Flight Path

In addition to the peaks from the beta-delayed neutrons, Figure 3.5 also shows that the neutron detectors occasionally detected the β^- from ^{17}N decay, and measured its TOF. Since the energies of the ejectiles from the ^{17}N decay are known, the measured TOF's can be used to determine the flight path from the beam-stopping scintillator to each neutron detector. Table 3.2 shows the ejectiles from the decay of ^{17}N, along with their energies and the corresponding velocities. The flight path ℓ is given by

$$\ell = v_n \cdot [(C_n - C_\beta) \cdot k + t_\beta]$$

where v_n is the neutron velocity, C_n and C_β are the peak centroids of the neutron and the beta, k is the TDC calibration in ns/channel (Section 3.1.1), and t_β is the flight time of the beta. Note, the kinetic energy of the β particle is much larger than its rest mass, and it travels at essentially the speed of light. In experiment 93045, the average flight path for neutron detectors 1-14 was determined to be 101.3 ± 0.4 cm, and 91.8 ± 0.3 cm for detectors 15 and 16.

Table 3.2 Ejectile energies from the decay of ^{17}N. Corresponding velocities, and the peak position in Figure 3.5 are also shown. These values are used to determine the length of the neutron flight path.

Ejectile	Kinetic Energy (MeV)	Velocity (cm/ns)	Peak Centroid (Figure 3.5)
β	3.3	29.7	189.4
n	1.689	1.798	1241.3
n	1.161	1.490	1469.2
n	0.384	0.857	-

3.1.4 Identification of the Reaction Products

Once the calibration of the neutron detectors was completed, measurements of the (d,n) reaction cross sections were attempted for both d(^{12}C,^{13}N)n and d(^{7}Be,^{8}B)n. Collision of the secondary beams with the CD_2 target led to a wide variety of reaction products. These were identified by the fragment telescopes. Figure 3.7 and Figure 3.8

show the values of ΔE-E from the fragment telescopes for both $^{12}C + CD_2$ and $^{7}Be + CD_2$. These figures indicate the identification of the nuclei detected at the fragment telescopes, and the clear separation between isotopes.

The events leading to the detection of the (d,n) reaction product ^{13}N are clearly visible in Figure 3.7, and are easily isolated from the other fragments hitting this detector. Integration of these events will lead to the measure of the cross section for the d(^{12}C,^{13}N)n reaction.

The ^{8}B events are also clearly visible in figure 3.8, and are separable from other events in this detector. However, in addition to production from the (d,n) reaction, ^{8}B events also resulted from the scattering of the ^{8}B beam contaminant into the detectors. In order to determine the reaction cross section in the case of d(^{7}Be,^{8}B)n, the ^{8}B reaction product had to be isolated from the background events. This process was straightforward, and is illustrated in Figure 3.9. Because the ^{8}B product was ejected at specific energies defined by the reaction kinematics, the projection of the ^{8}B total energy shows a strong peak at the allowed energies. The scattered beam contaminant, however, was evenly distributed over a range of energies. Subtracting this flat background from the total energy spectrum gives the true reaction yield for the range of angles covered by this detector.

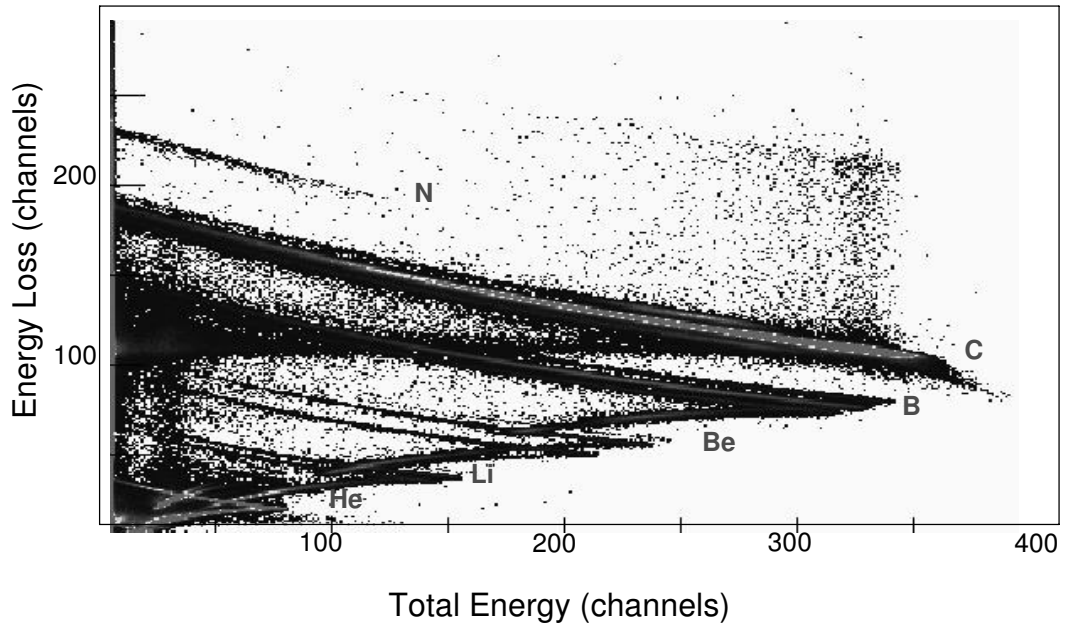

Figure 3.7 Subset of the fragments detected in the Top Fragment Detector from ^{12}C + CD_2.

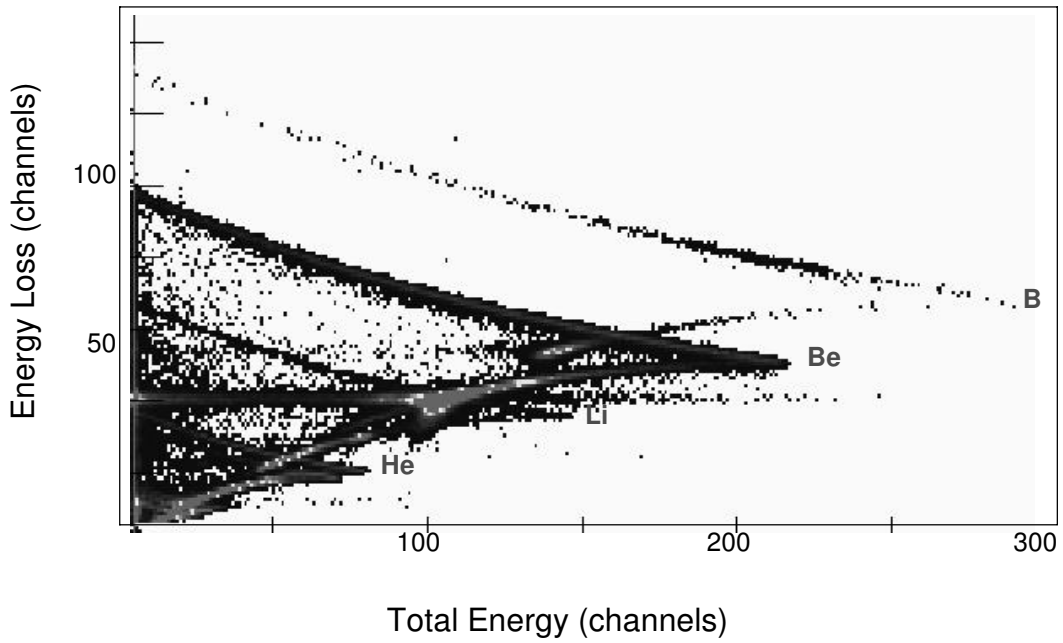

Figure 3.8 Fragments detected in the Top Fragment Detector from ^{7}Be + CD_2.

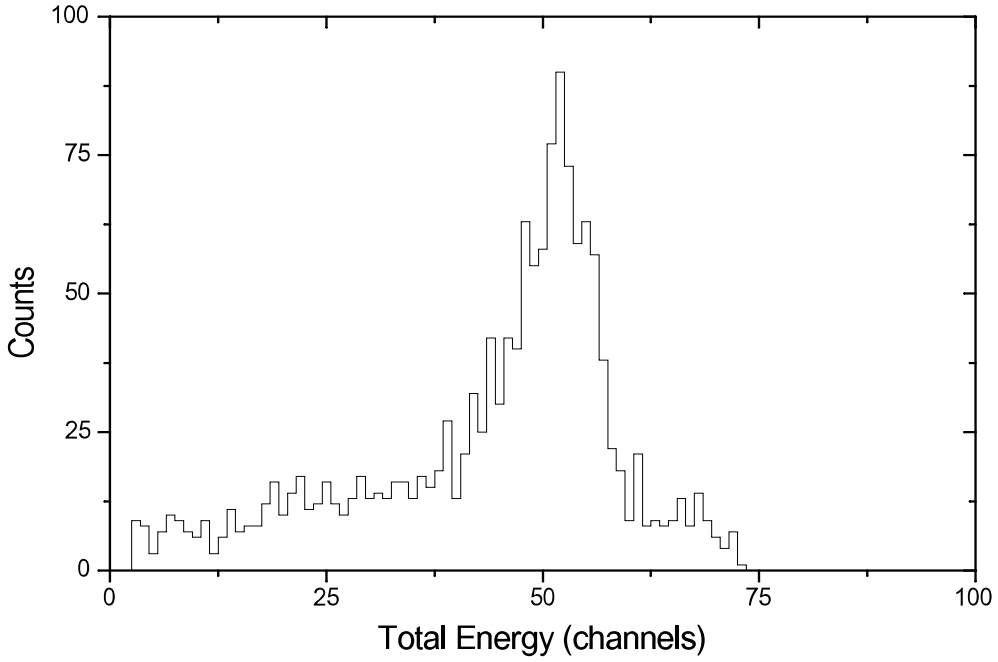

Figure 3.9 Measured total energy of ^{8}B fragments detected in the top telescope. Flat background is due to scattered beam impurities hitting detector, peak is ^{8}B events from the (d,n) reaction.

Once the heavy reaction products had been separated from the other events in the forward telescopes, their correlation with events in the neutron detectors could be observed. Figure 3.10 shows events in neutron detector #9 correlated with ^{13}N events in the fragment detectors. This neutron TOF spectrum shows a sharp peak at a particular neutron energy which is defined by the detector's position and the reaction kinematics. Similar correlation is seen in Figure 3.11 with neutron detector #9 and ^{8}B events. Figures 3.12 and 3.13 show the energies of the neutron peaks plotted against the angles of the neutron detectors. The measured neutron energies correlate well with the kinematics for

each reaction. This is a clear signal that the peaks in the neutron detectors result from the reactions we intended to study. Integration of these peaks could lead to a second measurement of the reaction cross sections of d(^{12}C,^{13}N)n and d(^{7}Be,^{8}B)n.

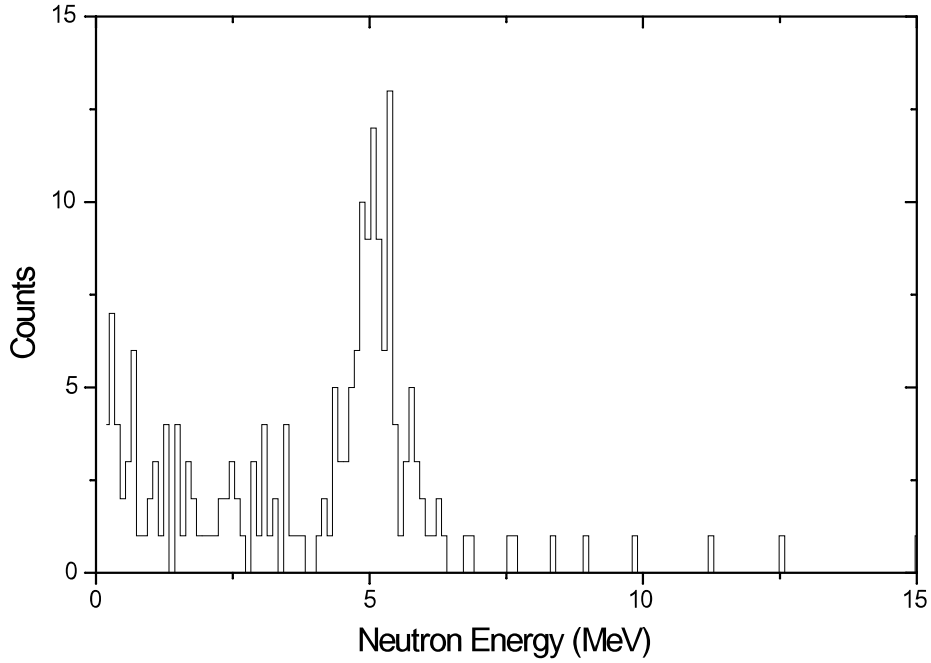

Figure 3.10 Neutron events in coincidence with ^{13}N events in the forward telescope. Data shown is from Neutron Detector #1. The neutron energy is determined by the reaction kinematics and the detector's angular coverage.

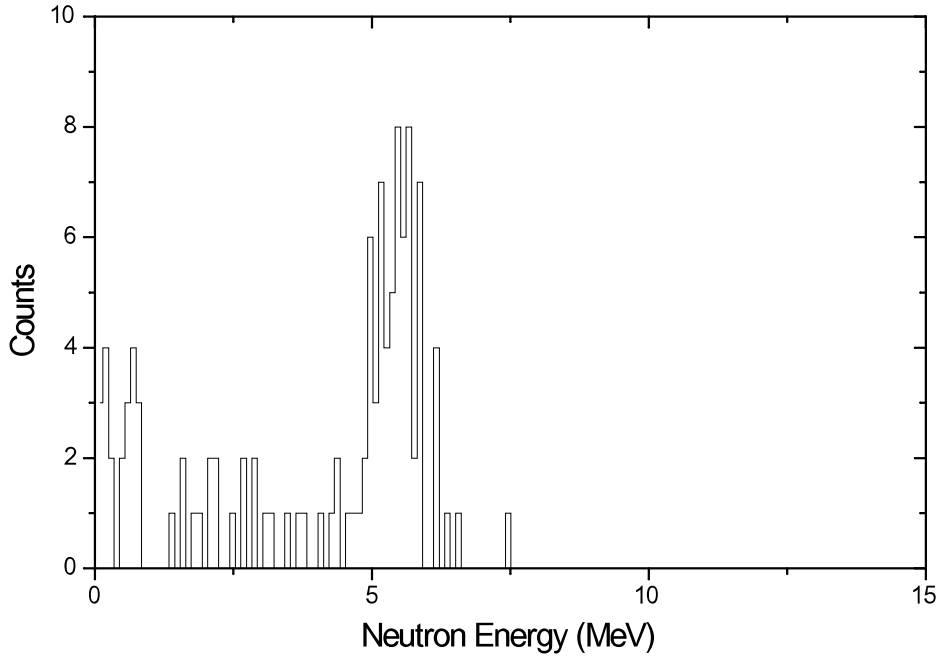

Figure 3.11 Neutron events in coincidence with ^{8}B events in the forward telescope. Data shown is from Neutron Detector #1. The neutron energy is determined by the reaction kinematics and the detector's angular coverage.

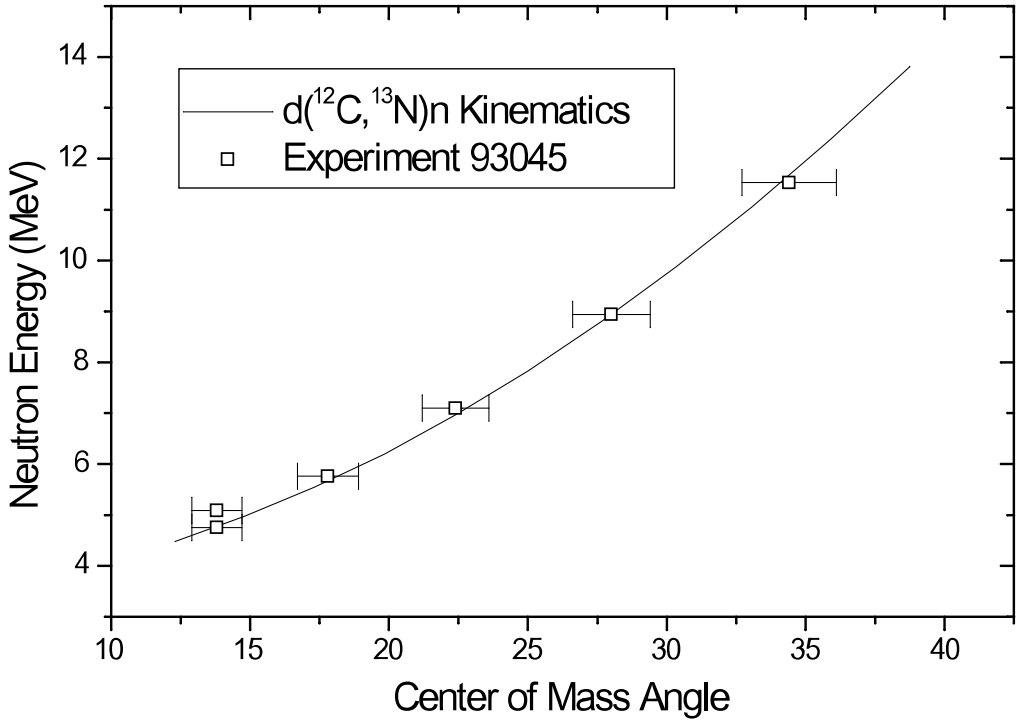

Figure 3.12 Measured energies of neutrons in coincidence with ^{13}N, along with the reaction kinematics.

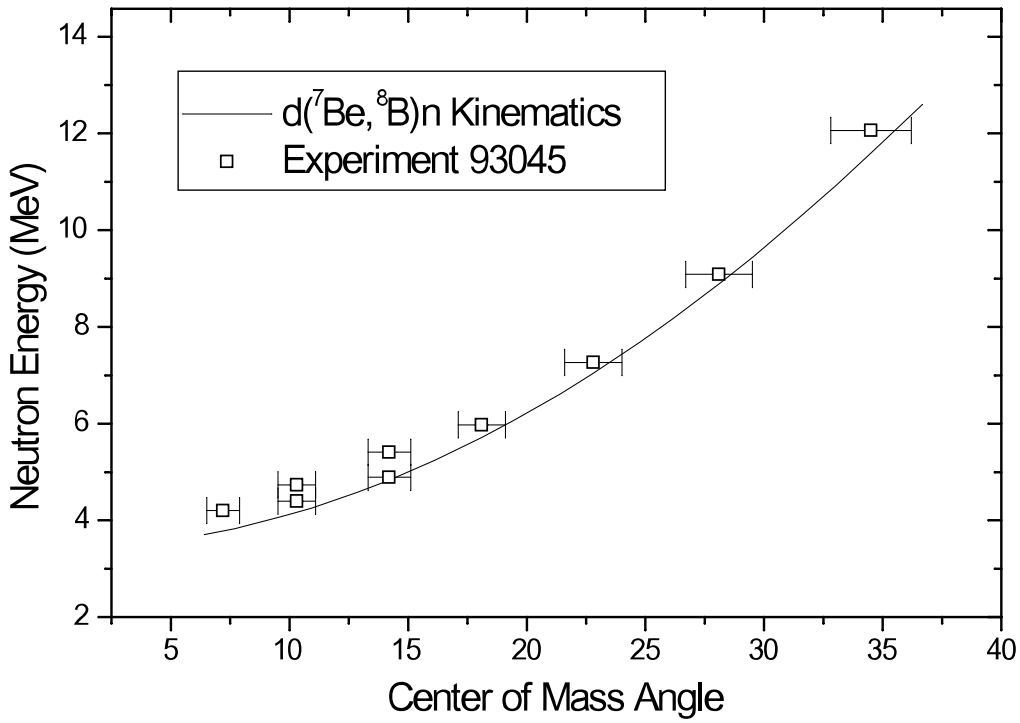

Figure 3.13 Measured energies of neutrons in coincidence with ^{8}B, along with the reaction kinematics.

3.1.5 Determination of the Beam Flux

In order to make a measurement of a reaction cross section, it is critical to measure the flux of incident particles with high precision. Unfortunately, the A1200 Target Monitors (see Section 2.2.1) failed during the course of Experiment 93045, which prevented an absolute measurement of the flux of the incident beams. Without knowledge of the incident beam flux, the absolute reaction cross sections of d(^{12}C,^{13}N)n and d(^{7}Be,^{8}B)n could not be measured.

3.1.6 Measurement of the Fragment Angle

The goal of Experiment 93045 was to measure the differential cross sections of d(^{12}C,^{13}N)n and d(^{7}Be,^{8}B)n over a range of angles. As described in Section 2.2.2, the experiment used PPAC's to measure the position and thus the angle of the reaction products. Unfortunately, the position resolution of the PPAC's for ^{8}B ions @ 25 MeV/A was much poorer than expected (~8 mm FWHM). This position resolution corresponded to an uncertainty in the fragment angle of ~0.5° in the lab, and ~5.0° in the center-of-mass frame. It is thought that the high energy and low nuclear charge of the ion led to weak ionization in the very thin detectors, and a low signal-to-noise ratio. This poor position resolution made it impossible to accurately determine the angular distribution of the reaction cross sections.

Another inherent limitation of the PPAC is the large aluminum frame surrounding the active area of the detector. This frame prevented placing the detector's active area at

angles very near to the beam axis. In order to keep the PPAC frame out of the path of the incident beam, the smallest angle that could be measured is about 2.0° in the lab.

3.1.7 Learning From Experiment 93045

Although Experiment 93045 failed to make a measurement of the reaction cross sections of d(^{12}C,^{13}N)n and d(^{7}Be,^{8}B)n, the experiment showed that such a study was feasible, and pointed to improvements that could be made in subsequent measurements. The ΔE-E plots (Figures 3.7 and 3.8) showed clear identification of the heavy reaction products, and that they could be isolated from other events. The angular dependence of the coincidence neutron energies (Figures 3.12 and 3.13) showed clear evidence of the (d,n) reactions. Integration of both the heavy fragment and neutron events could lead to redundant measurements of the reaction cross sections. Counting rates of both reaction products were measured for various primary beam intensities, which would be used to estimate the time needed to make a statistically precise measurement of the cross sections. However, it was clear that greater care needed to be taken to obtain precise normalization of the incident beam, and that detector systems for measurement of the heavy fragment angle needed improvement.

3.2 NSCL Experiment 96019

NSCL Experiment 96019 was proposed as an improvement to Experiment 93045, and was approved by NSCL PAC-20 for 126 hours of K1200 Cyclotron time. Experiment 96019 took place in July 1996.

In order to improve the measurement of d(^{7}Be,^{8}B)n, the Fragment Detectors were modified by replacing the PPAC's with Silicon Strip detectors. The poor position resolution of the PPAC's, along with the large frame surrounding the detector's active area, prevented an accurate measure of the cross section at small angles. The Strip Detectors were purchased without a frame surrounding the active area on one edge of the detector. This allowed the active area to be placed very near to the beam axis (~1.0°), allowing measurement of the reaction cross section at angles nearer to 0°. In addition, the segmented detector assures a position resolution of ±1.6 mm. With these detectors, the measurement of d(^{7}Be,^{8}B)n could be made over a broader range of angles with better angular resolution.

As with 93045, Experiment 96019 was divided into several parts, each of which is described in the following sections.

3.2.1 TDC Calibration

In order to accurately measure the neutron TOF, it was necessary to calibrate the response of all TDC channels. The method used is identical to that used in Experiment 93045, as described in Section 3.1.1. Particular effort was made to cover the entire range

of each TDC channel, as can be seen in Figure 3.14. This assured us of linearity over the entire time range. The measurement calibrated the response for each of the TDC channels, all were found to be quite linear and consistent. For a 512 channel histogram, the average of all 32 channels was found to be 2.540 channels/ns with an uncertainty of 0.001 channels/ns.

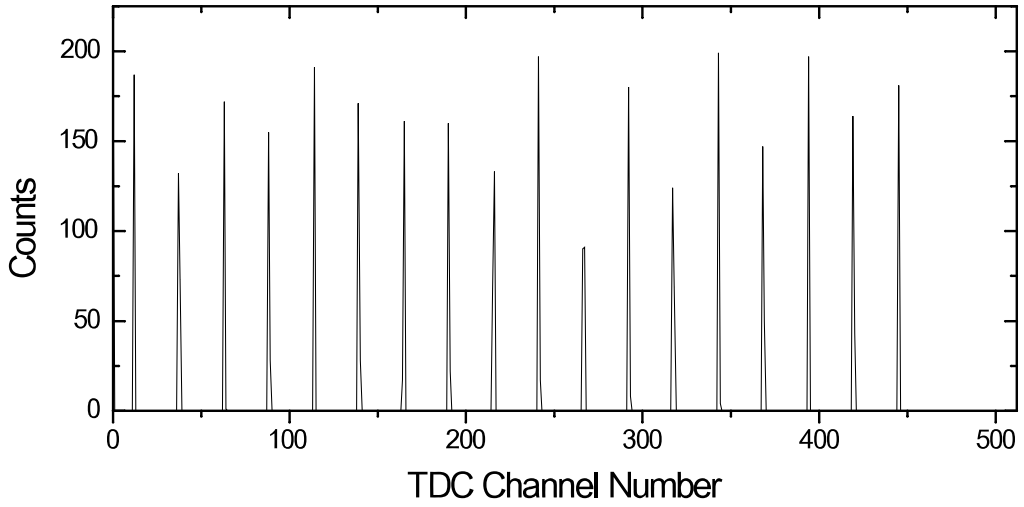

Figure 3.14 Time pulses used for TDC calibration of neutron detector #8. Time between peaks is known to be 10 ns, the TDC is set at 200 ns full scale.

3.2.2 Measurement of the Neutron Detection Efficiency

In order to determine the intrinsic detection efficiency of the neutron detectors used in Experiment 96019, the beta-delayed neutron decay of ^{17}N was again measured (see Section 3.1.2). Particular effort was made in this experiment to set electronic thresholds as low as possible, therefore increasing detection efficiency of lower-energy

neutrons. This resulted in the detection of the beta-delayed neutron at 0.384 MeV, in addition to those neutrons at 1.689 and 1.161 MeV. This can be seen in Figure 3.15, a sample TOF spectrum. From the integration of these peaks, the neutron efficiency is measured at three different neutron energies. Figure 3.16 shows measured detection efficiencies for all of the neutron detectors at each neutron energy. Because of their anomalously low detection efficiencies, as seen in Figure 3.16, Neutron Detectors 12, 15, and 16 were determined to be somewhat unreliable. The detection of the 0.4 MeV peak adds an additional point (compared to the fit shown in Figure 3.6) to the fit of detection efficiency versus neutron energy, seen in Figure 3.17.

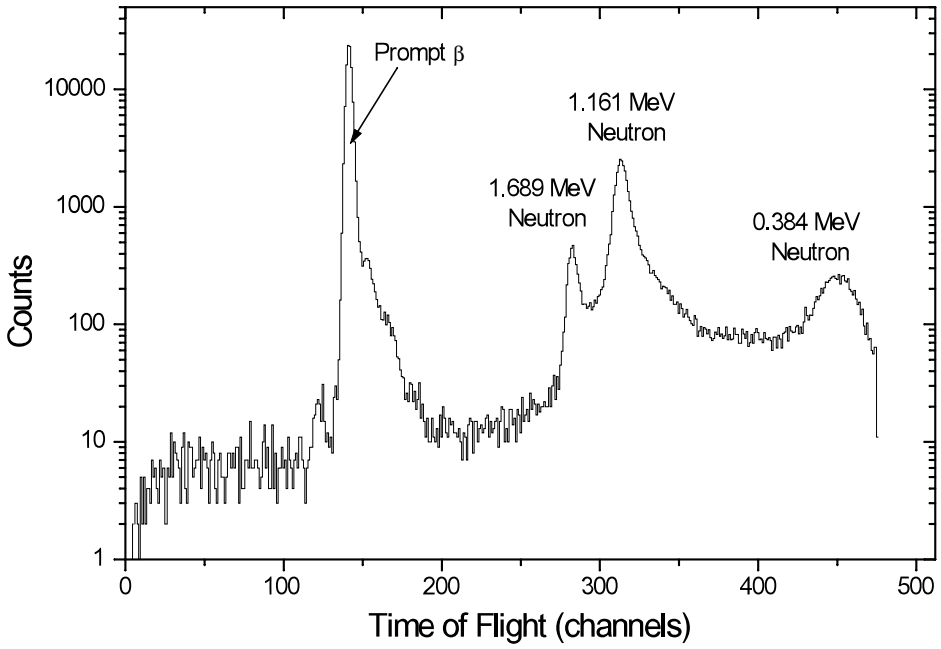

Figure 3.15 Time of flight spectrum from the decay of ^{17}N.

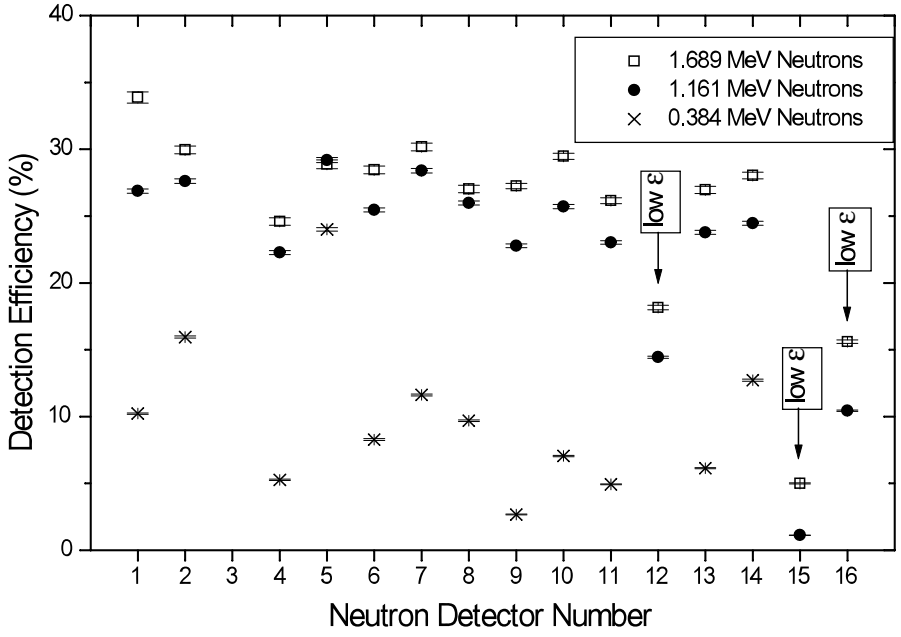

Figure 3.16 Measured neutron detection efficiencies for all neutron detectors at each neutron energy.

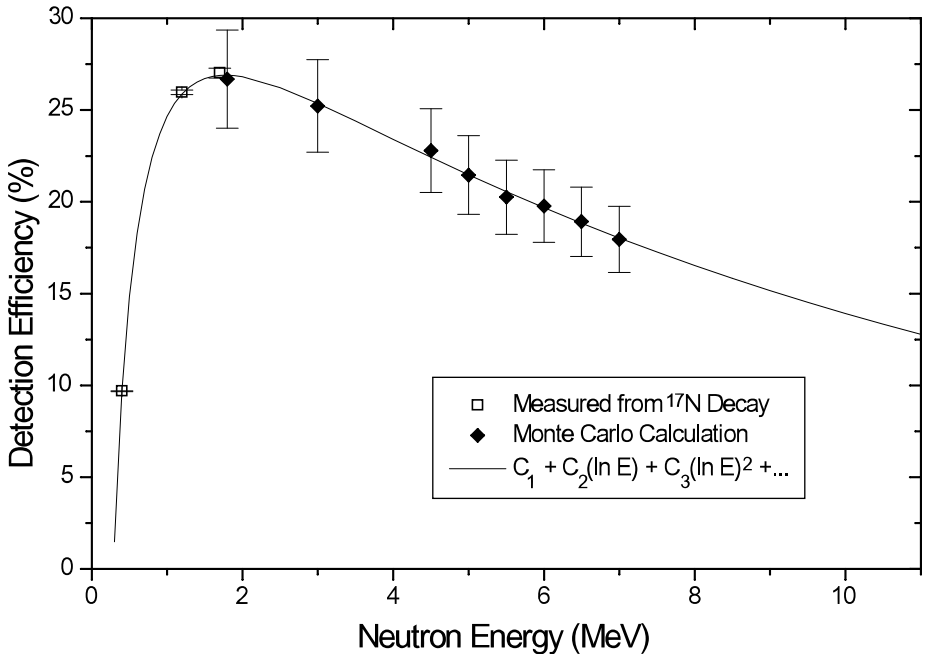

Figure 3.17 Fit to measured neutron detection efficiencies and monte carlo data for neutron detector #8. The function used for this fit is $\varepsilon = 24.66 + 8.14(\ell n\ E) - 7.97(\ell n\ E)^2 + 1.05(\ell n\ E)^3$.

3.2.3 Determination of the Neutron Flight Path

Because the neutron energies from the decay of ^{17}N are known, their measured peak positions in the TOF spectra can be used to determine the length of their flight path to each detector (see Section 3.1.3). Table 3.3 shows the distances determined from the neutron TOF spectra for each of the neutron detectors.

Table 3.3 Flight path lengths to neutron detectors determined by the decay of ^{17}N.

Neutron Detector Number	Distance from Reaction Target (m)
1	0.924 ± 0.017
2	1.007 ± 0.019
4	1.082 ± 0.020
5	1.013 ± 0.019
6	1.082 ± 0.020
7	1.015 ± 0.019
8	1.019 ± 0.019
9	1.010 ± 0.019
10	1.010 ± 0.019
11	1.073 ± 0.020
12	1.005 ± 0.016
13	1.070 ± 0.020
14	1.010 ± 0.019
15	1.073 ± 0.017
16	1.006 ± 0.016

3.2.4 Normalization of the Beam Flux

An accurate count of the incident beam particles is necessary for determination of the reaction cross section. In Experiment 96019, this was achieved by comparing the response of the A1200 Target Monitors to the Beam Normalization Detector at various beam intensities. Much care was taken with this calibration, and it was repeated every 24 hours.

Figure 3.18 shows the flux calibration of the ^{12}C beam made during the first few hours of the experiment. This calibration was repeated several times throughout the study of d(^{12}C,^{13}N)n, and the response of the A1200 target monitors was found to have remained constant.

Figure 3.19 shows the results of a series of flux calibrations made during the study of d(^{7}Be,^{8}B)n. The figure shows the result of radiation damage to the response of the A1200 target monitors during the experiment. Repeating the calibration over the course of the study proved to be crucial to obtaining an accurate normalization of the ^{7}Be beam. In fact, three of the four target monitors had failed completely by the end of the experiment due to the exposure to radiation from the production target.

From the flux calibrations in Figures 3.18 and 3.19, the number of beam particles reaching the reaction target can be determined for each experimental run. These results are tabulated for the study of d(^{12}C,^{13}N)n in Table 3.4, and for d(^{7}Be,^{8}B)n in Table 3.5.

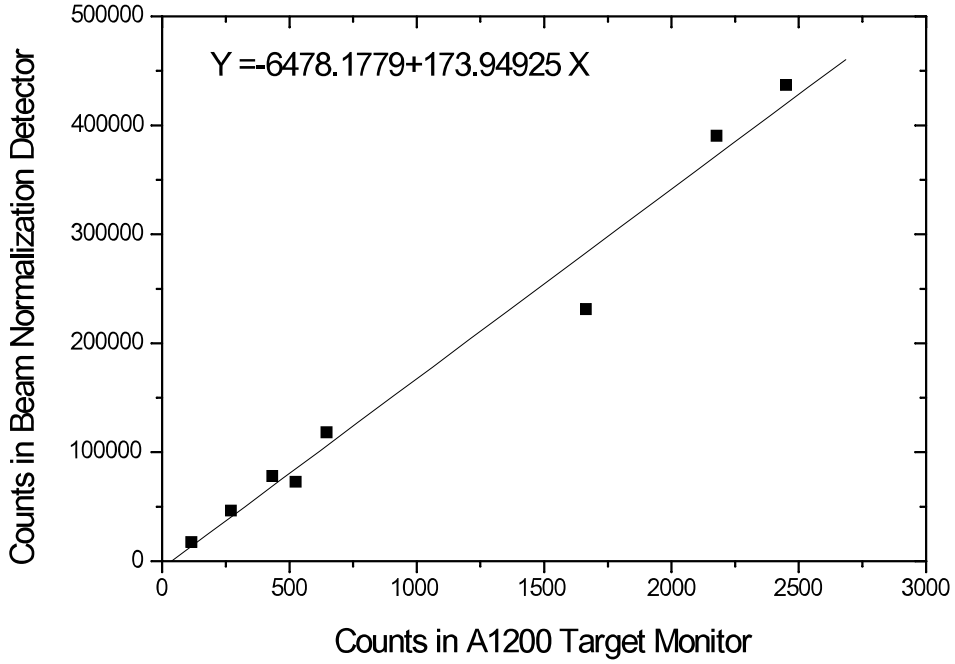

Figure 3.18 Flux calibration for the ^{12}C beam. This calibration remained constant throughout the study of d(^{12}C,^{13}N)n.

Table 3.4 Determination of the number of ^{12}C nuclei hitting the reaction target during the study of d(^{12}C,^{13}N)n. The total number of ^{12}C nuclei hitting the CD_2 target was 2.30×10^{10}, the total number hitting the C target was 2.73×10^{9}. Correcting these counts for the live-time of the data acquisition, the number of 'computer-live' hits was 1.50×10^{10} for the CD_2 target and 1.44×10^{9} for the C target.

Run Number	Reaction Target	A1200 Target Monitor Counts	Slope of Flux Calibration	Beam Purity (%)	Number of ^{12}C on Target
53	CD_2	12311391	173.95	100	2.14×10^{9}
54	CD_2	20994624	173.95	100	3.65×10^{9}
56	CD_2	8458663	173.95	100	1.47×10^{9}
65	CD_2	29799852	173.95	100	5.18×10^{9}
66	CD_2	19876518	173.95	100	3.46×10^{9}
67	CD_2	22608620	173.95	100	3.93×10^{9}
68	CD_2	18457000	173.95	100	3.21×10^{9}
69	C	9130700	173.95	100	1.59×10^{9}

70	C	6580443	173.95	100	1.14×10^9

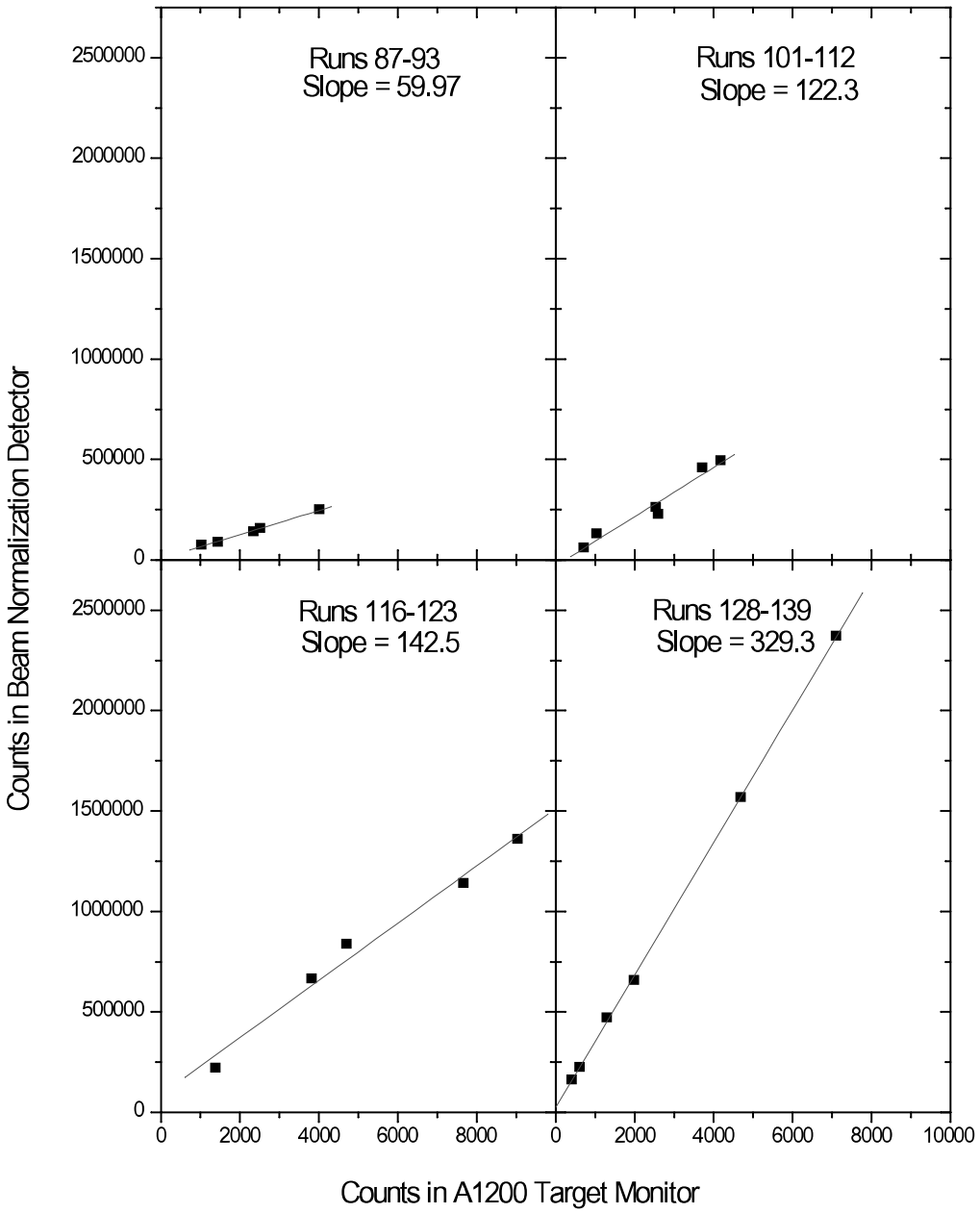

Figure 3.19 Flux calibration for the ^{7}Be beam. Radiation damage caused the change of the response of the A1200 Target Monitor throughout the study. These figures span approximately 80 hours of beam on target.

Table 3.5 Determination of the number of ^{7}Be nuclei hitting the reaction target during the study of d(^{7}Be,^{8}B)n. The total number of ^{7}Be nuclei hitting the CD_2 target was 2.00×10^{10}, the total number hitting the C target was 2.80×10^{9}. Correcting these counts for the live-time of the data acquisition, the number of 'computer-live' hits was 1.08×10^{10} for the CD_2 target and 1.38×10^{9} for the C target.

Run Number	Reaction Target	A1200 Target Monitor Counts	Slope of Flux Calibration	Beam Purity (%)	Number of ^{7}Be on Target
77	CD_2	13571883	69.79	96	9.07×10^{8}
78	CD_2	7808436	69.94	96	5.23×10^{8}
79	CD_2	5651673	70.10	96	3.80×10^{8}
80	C	2639599	70.27	96	1.78×10^{8}
83	CD_2	7335430	70.92	96	4.98×10^{8}
84	CD_2	6743400	71.18	96	4.60×10^{8}
85	CD_2	4405175	71.47	96	3.02×10^{8}
86	CD_2	11082235	71.79	96	7.62×10^{8}
91	CD_2	9919228	73.96	96	7.03×10^{8}
92	CD_2	11858100	74.54	96	8.47×10^{8}
96	C	900415	77.52	96	6.69×10^{7}
97	C	4010754	78.47	96	3.02×10^{8}
98	CD_2	8651044	79.52	96	6.59×10^{8}
99	CD_2	10434729	80.68	96	8.06×10^{8}
100	CD_2	8041549	81.95	96	6.31×10^{8}
105	CD_2	7350902	90.64	96	6.38×10^{8}
107	CD_2	15693390	95.50	96	1.44×10^{9}
108	CD_2	6210953	98.32	96	5.85×10^{8}
113	C	8614311	117.5	96	9.70×10^{8}
114	CD_2	10029272	122.6	96	1.18×10^{9}
115	CD_2	9055258	128.2	96	1.11×10^{9}
119	CD_2	7721211	157.3	96	1.16×10^{9}
120	CD_2	9072872	166.6	96	1.45×10^{9}
121	C	3002057	176.8	96	5.08×10^{8}
124	CD_2	7161173	214.3	96	1.47×10^{9}
125	CD_2	3919418	229.5	96	8.62×10^{8}
131	C	1152291	360.2	96	3.98×10^{8}
132	CD_2	1740571	390.5	96	6.51×10^{8}
133	CD_2	2123111	424.1	96	8.62×10^{8}
134	CD_2	1095528	461.1	96	4.84×10^{8}
135	CD_2	1372605	501.9	96	6.60×10^{8}
136	C	730937	547.1	96	3.83×10^{8}

3.2.5 Identification of the Reaction Products

Figure 3.20 shows the correlated ΔE-E signals obtained by the Fragment Telescopes from the interaction of the ^{12}C beam with the CD_2 target. Figure 3.21 shows similar results from ^{12}C + C. If the gate around the ^{13}N events shown in Figure 3.20 is projected onto the neutron detectors, sharp peaks in the neutron TOF result, as shown in Figure 3.22. These peaks come from neutrons in coincidence with ^{13}N from the d(^{12}C,^{13}N)n reaction.

Similar results were seen using the ^{7}Be beam. Figure 3.23 and 3.24 show the ΔE-E plots from ^{7}Be + CD_2 and ^{7}Be + C, respectively. Applying the gate around the ^{8}B events shown in Figure 3.23 to the neutron detectors gives Figure 3.25, the coincidence neutron TOF from the d(^{7}Be,^{8}B)n reaction.

One notable difference between the data sets resulting from the ^{12}C beam and those from the ^{7}Be beam is the amount of background measured from the C target. The ΔE-E plots from ^{12}C + C show few ^{13}N events, while the plots from ^{7}Be + C show a large number of ^{8}B events over a range of energies. These events result from the main impurity of the ^{7}Be beam: ^{8}B. The ^{8}B contaminant scatters throughout the beamline, creating a background of ^{8}B nuclei over a broad range of energies and angles. Subtraction of the ^{8}B background events will be crucial to obtain an accurate measure of the reaction cross section using the data from the forward telescopes. The ^{8}B background should not be in coincidence with neutrons, however, so the cross section determined from the neutron data will be free of background from the beam impurity. Comparison of the two

measurements of the cross section will show whether or not the background subtraction was done correctly.

Other features are evident in the ΔE-E plots corresponding to the combinations of various beams and targets. Events resulting from the elastic scattering of beam from the target are shown in Figures 3.21 and 3.24. These events were used to make energy calibrations of the Fragment Telescopes, a process detailed in Section 3.2.7.

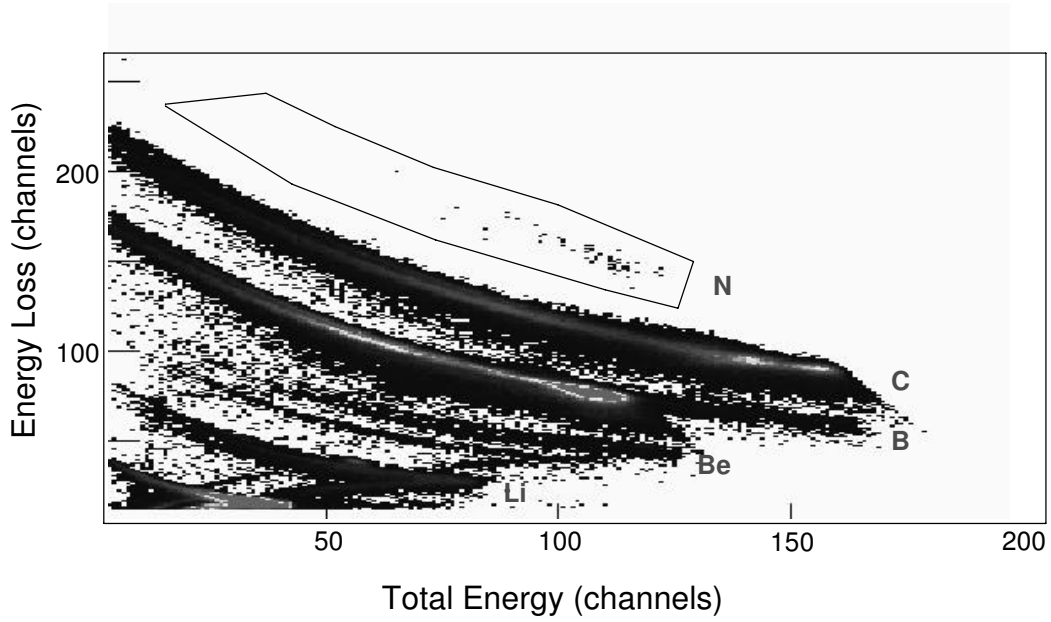

Figure 3.20 Subset of the fragments detected in the Bottom Fragment Detector from $^{12}C + CD_2$.

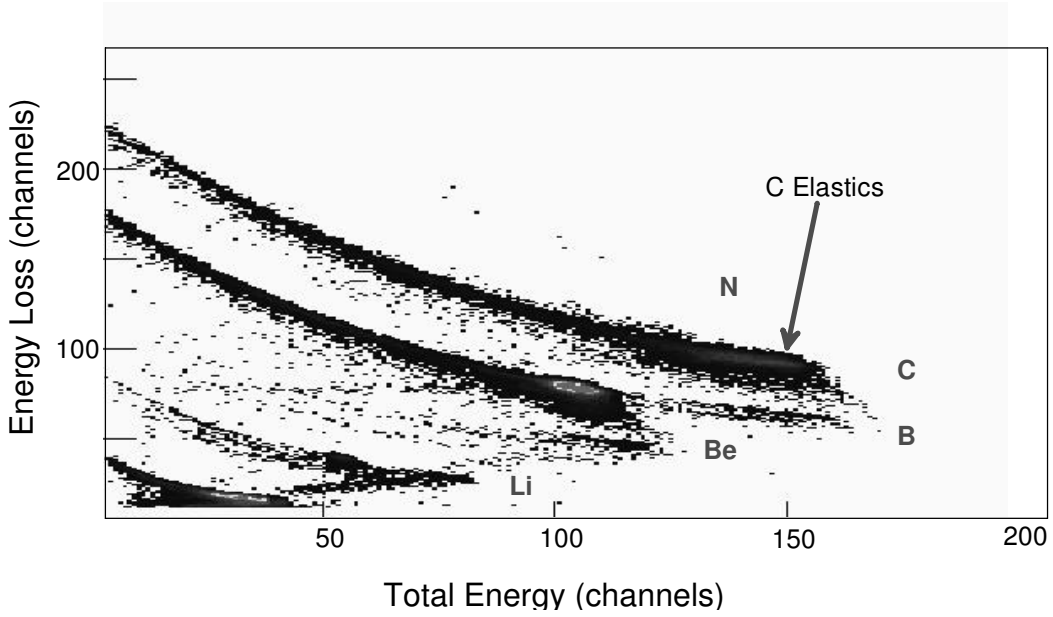

Figure 3.21 Fragments detected in the Bottom Fragment Detector from $^{12}C + C$.

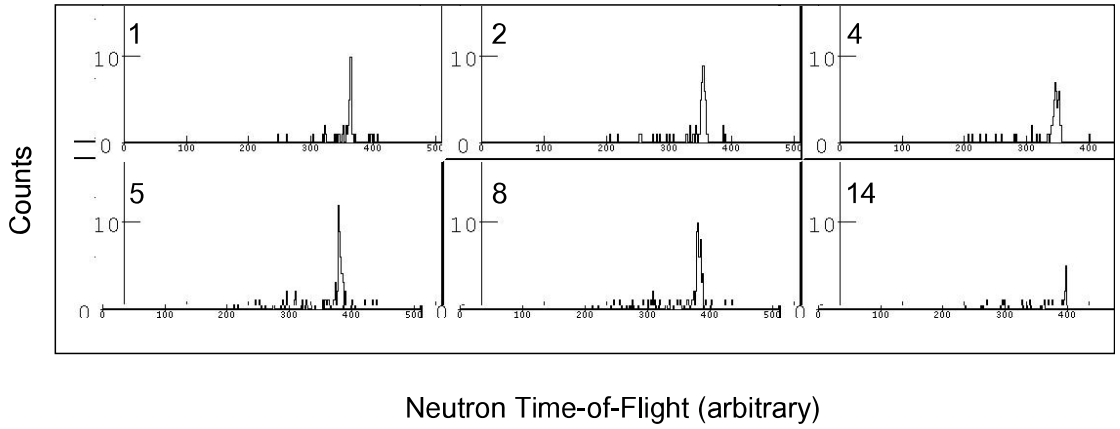

Figure 3.22 Neutrons in Coincidence with ^{13}N produced from $^{12}C + CD_2$. Times-of-flight for each of the six neutron detectors are shown.

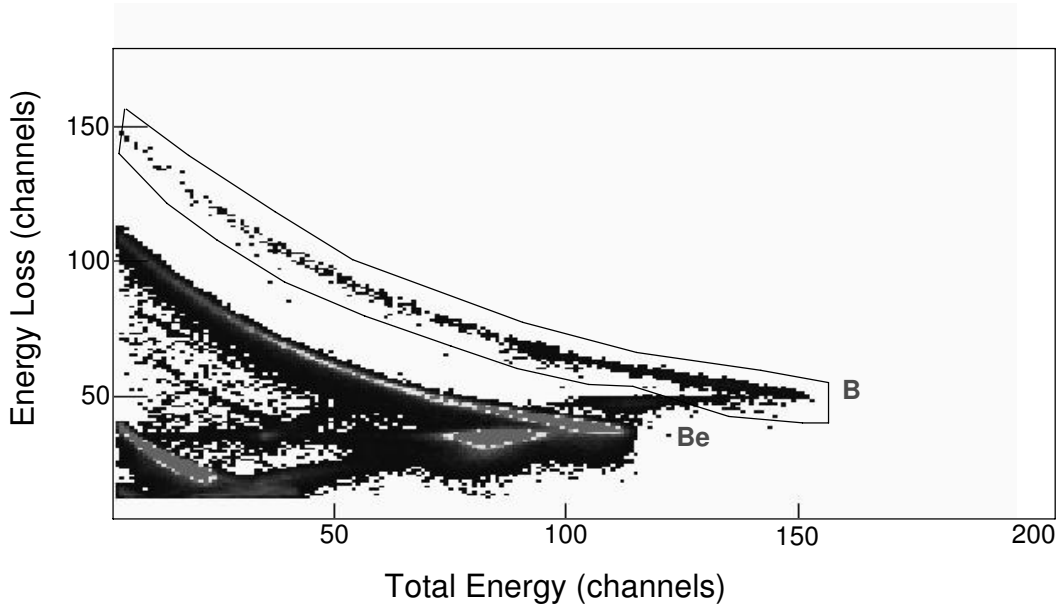

Figure 3.23 Subset of the fragments detected in the Bottom Fragment Detector from $^{7}Be + CD_2$.

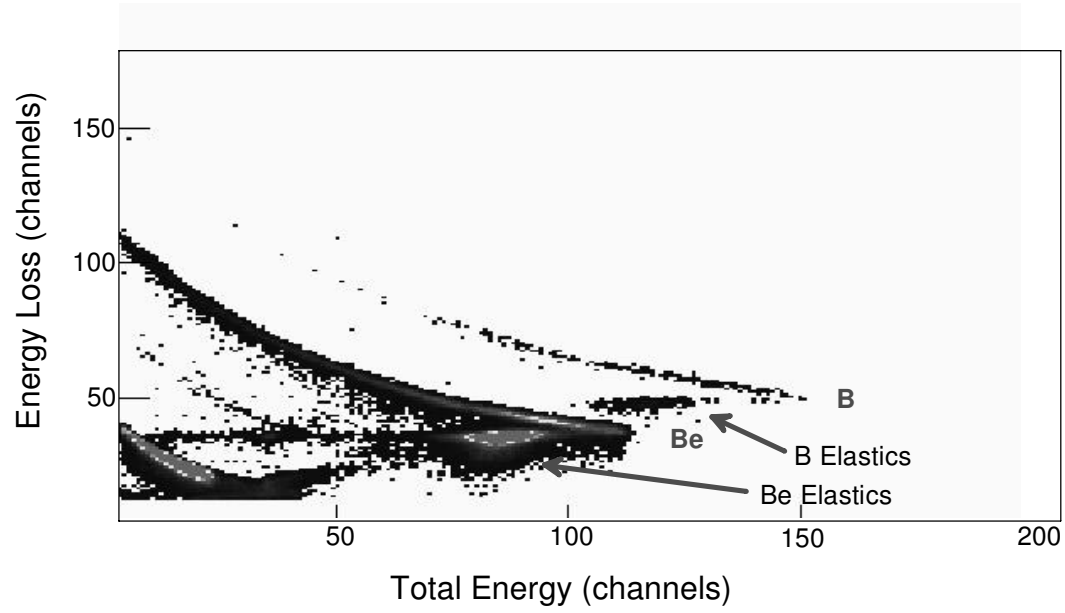

Figure 3.24 Subset of the fragments detected in the Bottom Fragment Detector from $^{7}Be + C$.

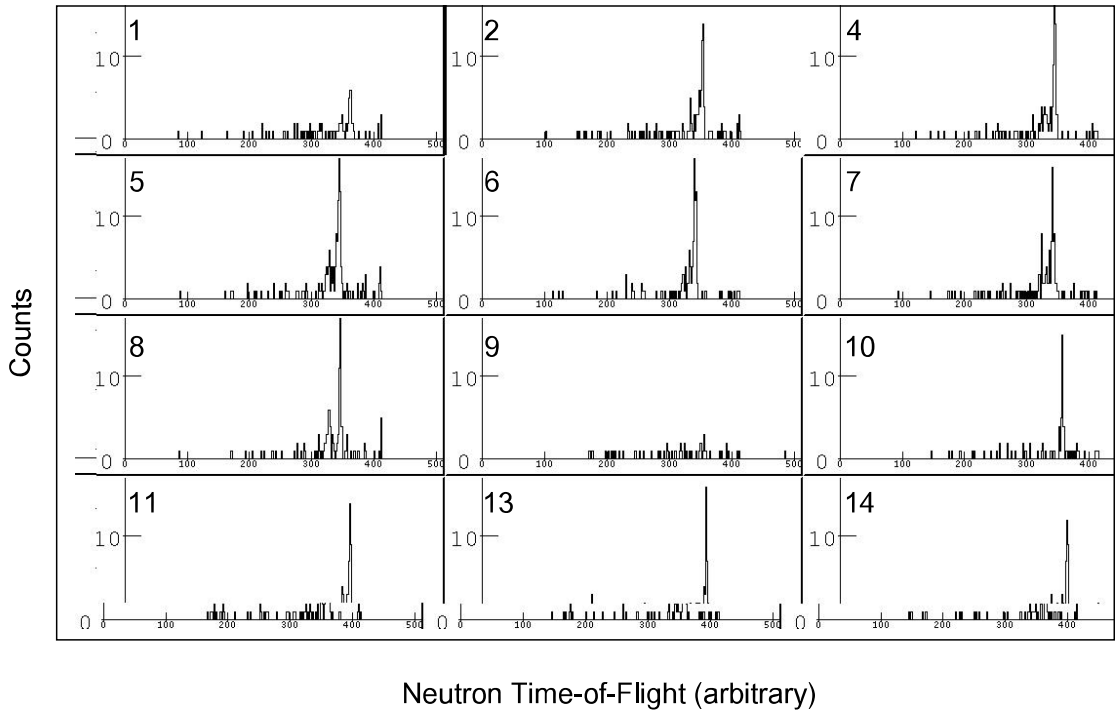

Figure 3.25 Neutrons in Coincidence with ^{8}B produced from ^{7}Be + CD_2. Times-of-flight for each of the twelve neutron detectors are shown.

3.2.6 Energy Calibration of the Neutron Detectors

In order to measure the energy of the neutrons emitted from the (d,n) reaction, it was necessary to calibrate the neutron TOF. The slope of the TOF calibration is determined by the TDC calibrations described in Section 3.2.1, and the peaks from relativistic particles (β,γ) in the neutron spectra determine the intercept. The validity of the calibration is shown in Figures 3.26 and 3.27. In these figures, the energies of the coincidence neutron peaks show very good agreement with the reaction kinematics for both d(^{12}C,^{13}N)n and d(^{7}Be,^{8}B)n systems.

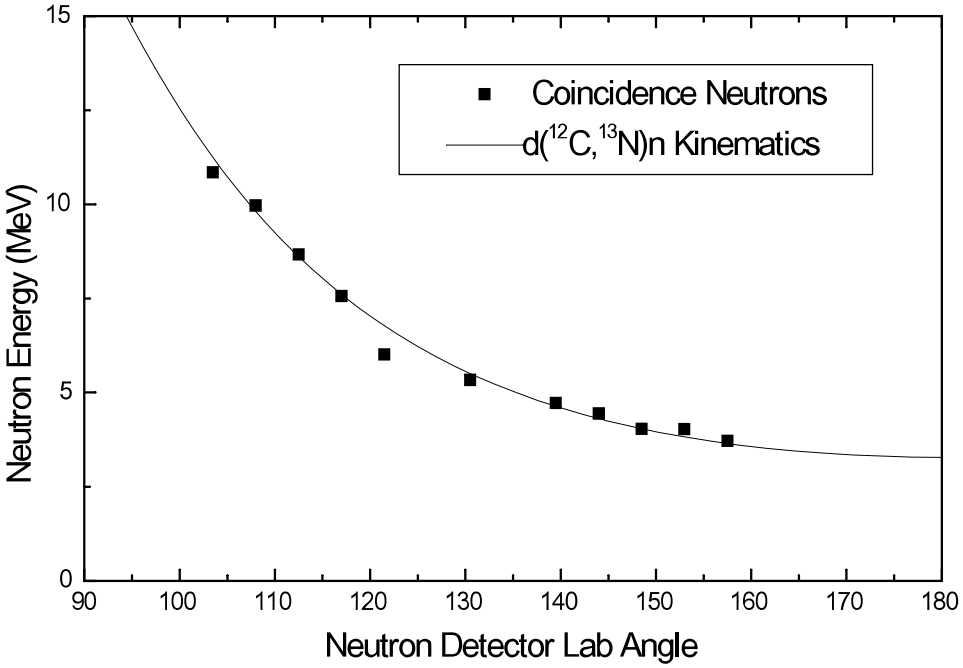

Figure 3.26 Neutron kinematics from d(^{12}C,^{13}N)n.

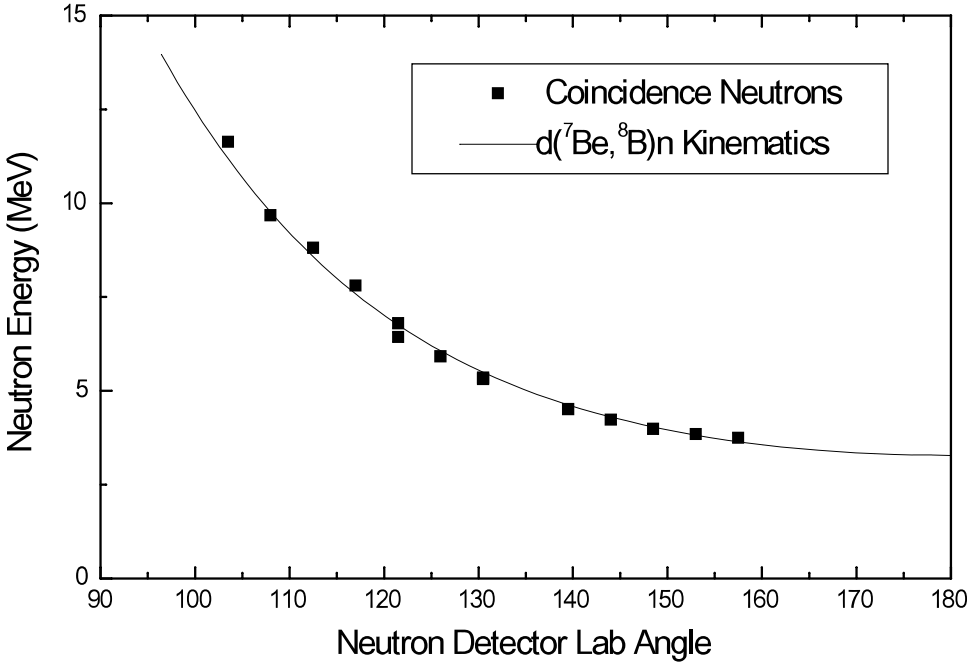

Figure 3.27 Neutron kinematics from d(^{7}Be,^{8}B)n.

3.2.7 Calibration of Fragment Telescopes by Elastic Scattering

In order to determine the energies of the heavy products of the (d,n) reactions, the response of the Fragment Telescopes had to be calibrated. This was done using the elastic scattering of the beam nuclei from the carbon target, the locus of which are marked in Figures 3.21 and 3.24. The kinematics of the elastic scattering are known, therefore each pixel of the Fragment Telescopes (a specific angle) records elastically scattered particles with a specific energy. Three elastic scattering reactions were used to calibrate each pixel: $^{12}C(^{12}C,^{12}C)^{12}C$, $^{7}Be(^{12}C,^{12}C)^{7}Be$, and $^{8}B(^{12}C,^{12}C)^{8}B$, and thus we have a three-point calibration for the energy scale.

The validity of the energy calibration is demonstrated in Figures 3.28 and 3.29. The coincidence neutron events from each neutron detector are projected onto the Fragment Telescopes. This defines a particular energy for each fragment group based on the lab angle of the neutron detector. In Figures 3.28 and 3.29, the calibrated energies for the ^{13}N and ^{8}B reaction products are plotted versus the neutron detector angle, along with the reaction kinematics. The agreement between the calculated energy and the kinematics show the calibration's validity. Note that the large error bars in these figures are a systematic effect resulting from the angular coverage of the neutron detectors and the expanded scale of the figure.

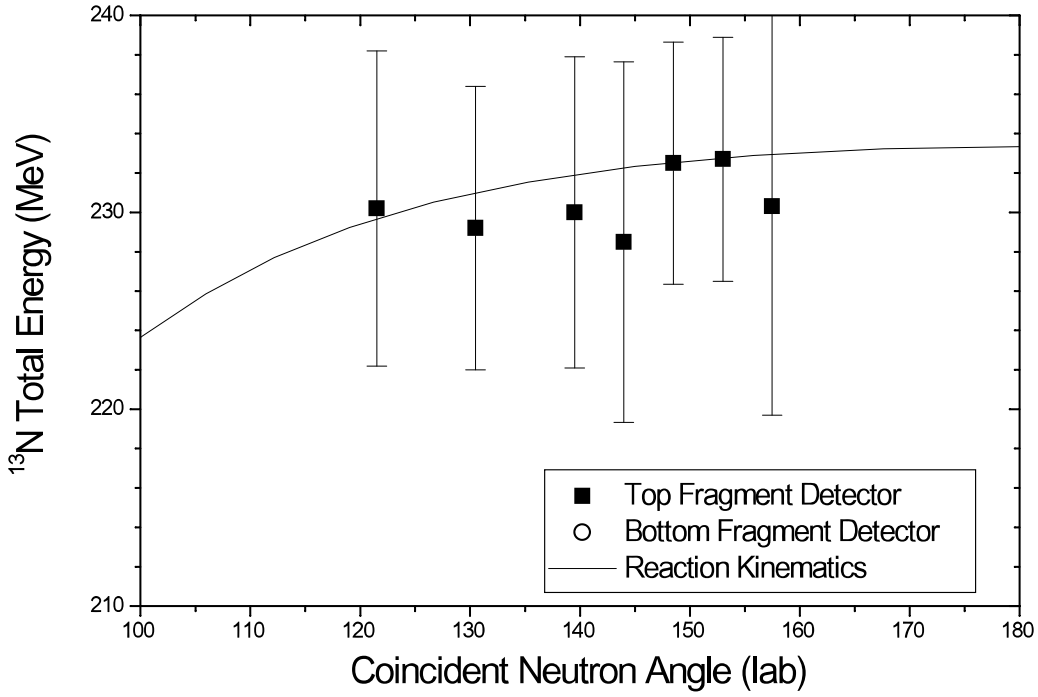

Figure 3.28 Kinematics of ^{13}N fragments in coincidence with neutrons.

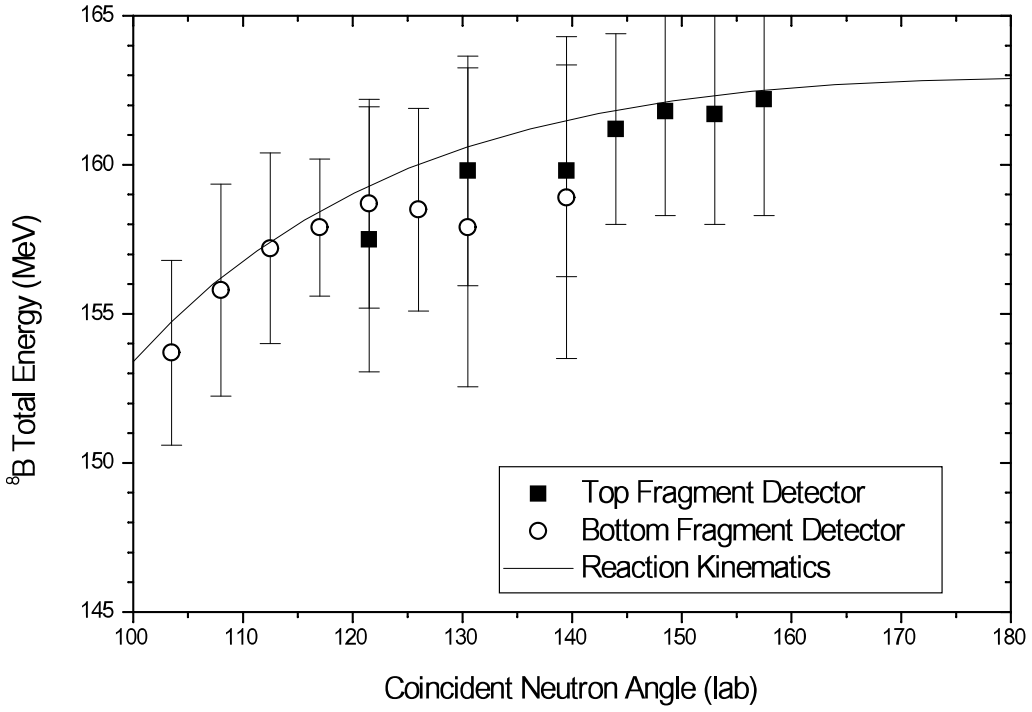

Figure 3.29 Kinematics of ^{8}B fragments in coincidence with neutrons.

3.2.8 Extraction of the Scattering and Reaction Cross Sections

A single procedure for extracting reaction cross sections was used for all reaction and scattering processes studied. This section details the methods for measuring the scattering cross sections of d(^{12}C,^{12}C)d and d(^{7}Be,^{7}Be)d, and the reaction cross sections of d(^{12}C,^{13}N)n and d(^{7}Be,^{8}B)n.

All measurements from Experiment 96019 made using the CD_2 target contain events resulting from beam interacting with deuterium, which we wish to study, and events resulting from the beam interacting with carbon. For this reason, all measurements using the CD_2 target were repeated with a target of pure carbon. This allowed the contribution of the carbon nuclei to be measured and removed from the CD_2 target data.

In order to perform this subtraction, the data must be normalized to the same number of incident beam particles and the same number of carbon atoms in each target. Table 3.6 and Table 3.7 contain the details of the normalization process for the ^{12}C and ^{7}Be beams, respectively.

The carbon-subtraction was performed on the histograms of the fragment total energy. These histograms were obtained by projecting the data falling into the fragment gates onto the total energy axis for each of 32 pixel groups in the fragment telescopes. The fragment gates are shown in Figure 3.20 for ^{13}N, Figure 3.21 for ^{12}C, Figure 3.23 for ^{8}B, and Figure 3.24 for ^{7}Be. The values in the histograms from the carbon target were multiplied by the normalization factor, then subtracted from the CD_2 target data. The resulting histograms should include only the contribution of the beam + deuterium, and Gaussian functions were fitted to these peaks. Fitting and integration of the peaks gives the number of detected product nuclei for each of the 32 pixel groups in the fragment telescopes. The measured peak areas are tabulated in Tables 3.8, 3.9, 3.10 and 3.11 for d(^{12}C,^{12}C)d, d(^{7}Be,^{7}Be)d, d(^{12}C,^{13}N)n, and d(^{7}Be,^{8}B)n systems, respectively.

For the transfer reactions d(^{12}C,^{13}N)n and d(^{7}Be,^{8}B)n, the number of coincidence neutrons served as an additional measure of the reaction cross sections. Because very few neutrons were observed with the carbon target (as opposed to the CD_2 target), subtraction of the carbon target data from the coincidence neutron data was deemed unnecessary. Integration of the neutron TOF peaks in each detector gives the number of neutrons resulting from the (d,n) reactions. The areas of these neutron peaks are tabulated in Table 3.10 for d(^{12}C,^{13}N)n and in Table 3.11 for d(^{7}Be,^{8}B)n.

In order to compare the yields for different groups of pixels in each detector, their solid angles must be normalized. The normalization was obtained through a Monte Carlo computer simulation of the detector geometries. In this way, the relative geometric and intrinsic efficiencies of all detectors can be easily accounted for. Figure 3.30 shows the results of these simulations for the d(^{7}Be,^{8}B)n reaction kinematics, the other reactions are similar. The figure shows the relative detection efficiencies (both geometric and intrinsic combined) for the fragment and neutron detectors. Note that the scatter in this plot is caused by the irregular grouping of pixels as shown in Figure 2.3.

The measured peak areas divided by the relative detector efficiency give the angular distribution of the reaction yield. The yield can be converted to a differential cross section using the beam flux (described in Section 3.2.4), the deuterium density in the target (1.33×10^{21} cm^{-2} for 18 mg/cm^2 CD_2), and the calculated solid angle of one of the detectors. The absolute cross sections for the remaining detectors were determined based on their relative yields. The measured angular distribution of the scattering cross sections for d(^{12}C,^{12}C)d and d(^{7}Be,^{7}Be)d are plotted in Figures 3.31 and 3.32, and tabulated in Tables 3.8 and 3.9. The measured angular distribution of the transfer reaction cross sections for d(^{12}C,^{13}N)n and d(^{7}Be,^{8}B)n are plotted in Figures 3.33 and 3.34, and tabulated in Tables 3.10 and 3.11.

For all cross section measurements, a discrepancy was found between the absolute normalization of the Top and Bottom Fragment Detectors. It was noted during the experiment that a constant-fraction discriminator used in the acquisition electronics had behaved erratically. It is suspected that this led to the loss of events by the Top Fragment

Detector. In addition, better particle identification was achieved with the Bottom Fragment Detector. For these reasons, the absolute normalization of the data was taken from the Bottom Fragment Detector. The results from the Top Fragment Detector were normalized to the results from the Bottom Fragment Detector, and were used to increase the angular coverage of the measurement.

The measurements of the scattering cross sections d(^{12}C,^{12}C)d and d(^{7}Be,^{7}Be)d have an important limitation at angles very near to the beam axis. The angular divergence of the ^{12}C and ^{7}Be beams caused *unscattered* beam to hit the detectors at very small lab angles. This caused very high count rates of ^{12}C or ^{7}Be in the pixel groups closest to the beam. These events cannot be separated from the elastic scattering events, and led to very high measured cross sections in these pixel groups. At twice the angular divergence of the beam (2° lab frame), this effect was estimated to be negligible. Therefore, data from those pixel groups which have lab angles smaller than 2° (Top 1 through Top 6) were removed from the measurements of the d(^{12}C,^{12}C)d and d(^{7}Be,^{7}Be)d scattering cross sections.

A limitation of the measurements of d(^{12}C,^{12}C)d, d(^{7}Be,^{7}Be)d, and d(^{12}C,^{13}N)n is the inability to resolve events leading to excited states of the products. Because of the energy spread of the incident beam (6% ≈ 15 MeV for the ^{12}C beam, 6% ≈ 10 MeV for the ^{7}Be beam), the energy resolution of the system was insufficient to identify nuclei in their low-lying excited states based on the energy deposited in the fragment detectors. ^{12}C, ^{13}N, and ^{7}Be all have bound excited states, and the deuteron can be excited to unbound continuum states above 2.2 MeV. The reported cross sections for these reactions may

therefore contain contributions from interactions leading to both ground and excited states of the products.

For the d(^{7}Be,^{8}B)n reaction, however, the measurement will be of the pure ground state to ground state transition. This is because ^{8}B contains no bound excited states, and any excitation would cause it to break up before reaching the Fragment Detectors.

Table 3.6 Normalization of the data taken with the ^{12}C beam using CD_2 and C targets during the study of d(^{12}C,^{12}C)d and d(^{12}C,^{13}N)n. When the data obtained from the C target is multiplied by the normalization factor, the two data sets are normalized to the same number of incident beam atoms and the same number of carbon atoms in the target.

Target	Carbons per cm^2 in target	Total ^{12}C beam atoms hitting target	Beam atoms × target atom	Normalization Factor
31 mg/cm^2 C	1.56×10^{21}	1.44×10^{9}	2.25×10^{30}	4.44
18 mg/cm^2 CD_2	6.66×10^{20}	1.50×10^{10}	9.99×10^{30}	-

Table 3.7 Normalization of the data taken with the ^{7}Be beam using CD_2 and C targets during the study of d(^{7}Be,^{7}Be)d and d(^{7}Be,^{8}B)n. When the data obtained from the C target is multiplied by the normalization factor, the two data sets are normalized to the same number of incident beam atoms and the same number of carbon atoms in the target.

Target	Carbons per cm^2 in target	Total ^{7}Be beam atoms hitting target	Beam atoms × target atom	Normalization Factor
31 mg/cm^2 C	1.56×10^{21}	1.38×10^{9}	2.15×10^{30}	3.35
18 mg/cm^2 CD_2	6.66×10^{20}	1.08×10^{10}	7.19×10^{30}	-

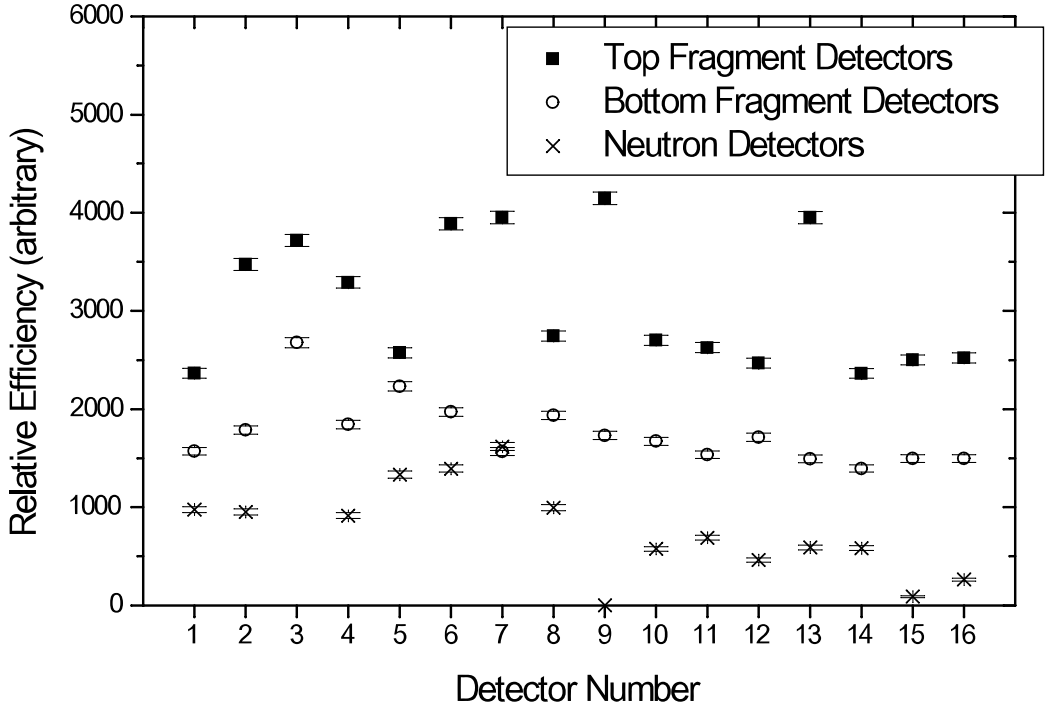

Figure 3.30 Relative detection efficiency of all detectors used in the measurement of d(^{7}Be,^{8}B)n. These were calculated using a Monte Carlo simulation of the detector geometries and intrinsic efficiencies. Similar calculations were performed using the kinematics of d(^{12}C,^{12}C)d, d(^{7}Be,^{7}Be)d, and d(^{12}C,^{13}N)n. Note that the scatter in this plot is caused by the irregular grouping of pixels as shown in Figure 2.3

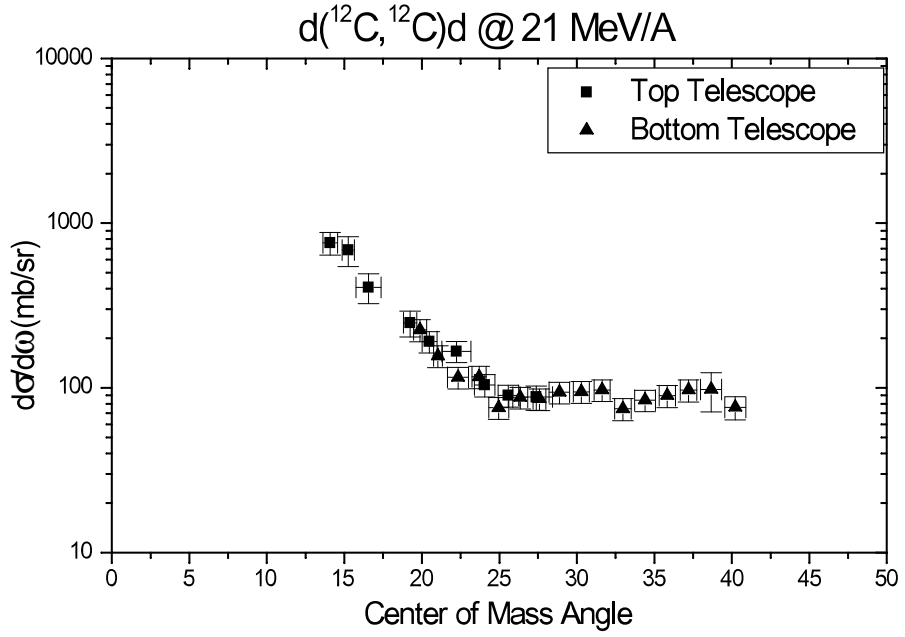

Figure 3.31 Measured Differential Reaction Cross section for d(^{12}C,^{12}C)d at 21 MeV/A.

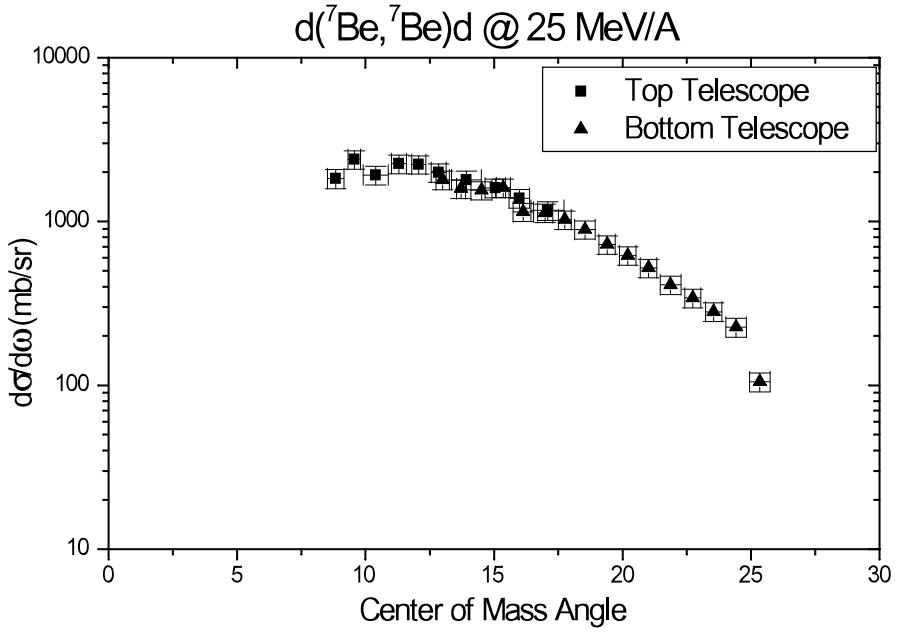

Figure 3.32 Measured Differential Reaction Cross section for d(^{7}Be,^{7}Be)d at 25 MeV/A.

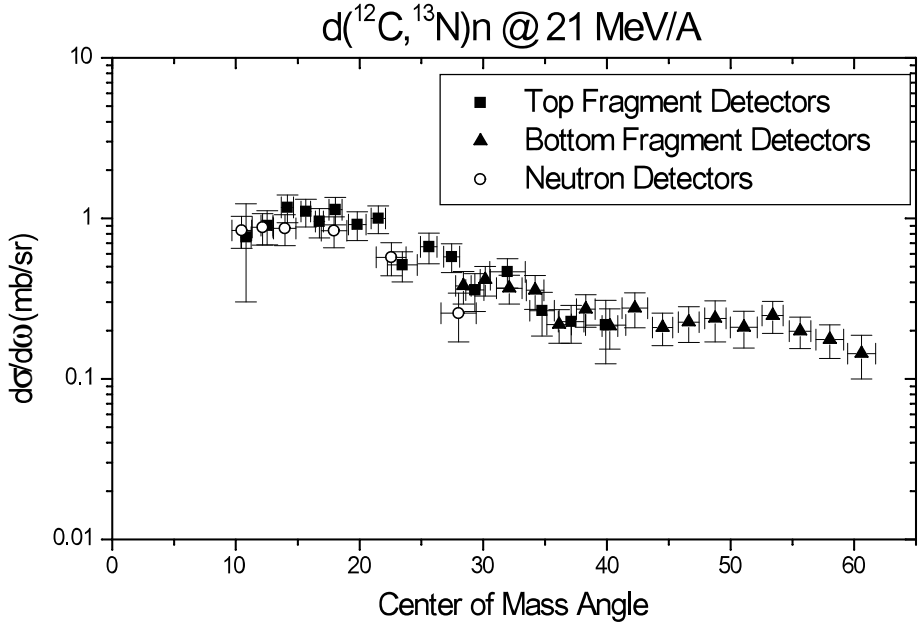

Figure 3.33 Measured Differential Reaction Cross section for d(^{12}C,^{13}N)n at 21 MeV/A.

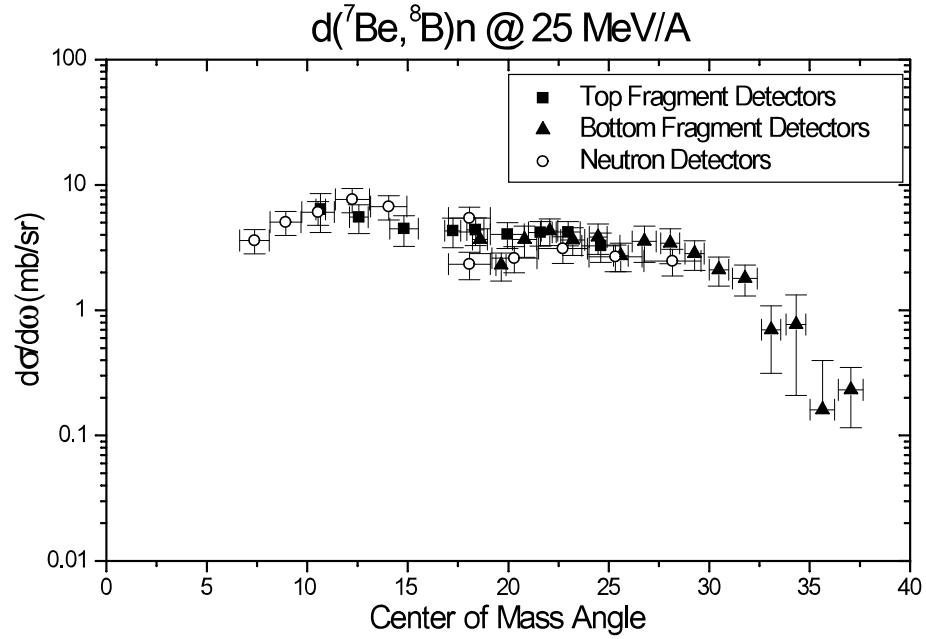

Figure 3.34 Measured Differential Reaction Cross section for d(^{7}Be,^{8}B)n at 25 MeV/A.

Table 3.8 Peak areas and calculated reaction cross sections from the detectors used in the measurement of d(^{12}C,^{12}C)d at 21 MeV/A.

Detector	Center of Mass Angle	Area of Gaussian Fit	Reaction Cross Section (mb/sr)
Top 1	7.78 ± 0.3	5563788 ± 305002	
Top 2	9 ± 0.35	5094015 ± 173178	
Top 3	10.16 ± 0.35	2065668 ± 71425	
Top 4	11.21 ± 0.28	745759.8 ± 40283	
Top 5	11.97 ± 0.23	312491 ± 5875	
Top 6	12.87 ± 0.37	320426.3 ± 19750	
Top 7	14.09 ± 0.48	201706.3 ± 12194	759.38 ± 117.94
Top 8	15.25 ± 0.4	132427.8 ± 19321	687.16 ± 140.58
Top 9	16.57 ± 0.81	115099.9 ± 16820	408.68 ± 83.56
Top 10	18.02 ± 0.45	59978.76 ± 6075	0 ± 38.04
Top 11	19.25 ± 0.43	43035.72 ± 4540	248.25 ± 44.23
Top 12	20.5 ± 0.48	31630.22 ± 972	191.09 ± 28.07
Top 13	22.24 ± 0.94	43938.74 ± 1135	166.63 ± 24.22
Top 14	24.06 ± 0.65	17207.28 ± 1051	104.32 ± 16.28
Top 15	25.59 ± 0.67	15309.68 ± 749	90.2 ± 13.68
Top 16	27.38 ± 1.04	15704.47 ± 1352	87.88 ± 14.71
Bottom 1	19.89 ± 0.41	15767.02 ± 736	224.87 ± 34.17
Bottom 2	21.05 ± 0.28	13329.86 ± 612	156.15 ± 23.62
Bottom 3	22.33 ± 0.67	16241.56 ± 673	115.78 ± 17.28
Bottom 4	23.7 ± 0.46	10255.56 ± 601	116.93 ± 18.19
Bottom 5	24.96 ± 0.65	8655.24 ± 391	75.78 ± 11.41
Bottom 6	26.35 ± 0.49	8083.77 ± 306	87.45 ± 13.02
Bottom 7	27.6 ± 0.41	6976.81 ± 287	85.63 ± 12.85
Bottom 8	28.88 ± 0.66	9451.38 ± 375	93.89 ± 14.01
Bottom 9	30.3 ± 0.52	7973.48 ± 345	94.84 ± 14.28
Bottom 10	31.64 ± 0.53	7494.54 ± 304	97.21 ± 14.58
Bottom 11	32.98 ± 0.54	5834.15 ± 318	74.66 ± 11.52
Bottom 12	34.4 ± 0.67	7436.46 ± 263	84.21 ± 12.49
Bottom 13	35.85 ± 0.52	6569.85 ± 374	89.68 ± 13.93
Bottom 14	37.21 ± 0.53	6970.36 ± 344	97.13 ± 14.83
Bottom 15	38.67 ± 0.68	7679.36 ± 1716	97.65 ± 25.97
Bottom 16	40.24 ± 0.68	5654.04 ± 405	76.3 ± 12.3

Table 3.9 Peak areas and calculated reaction cross sections from the detectors used in the measurement of d(^{7}Be,^{7}Be)d at 25 MeV/A.

Detector	Center of Mass Angle	Area of Gaussian Fit	Reaction Cross Section (mb/sr)
Top 1	4.78 ± 0.2	18500000 ± 400000	
Top 2	5.58 ± 0.23	12800000 ± 100000	
Top 3	6.33 ± 0.22	1700000 ± 100000	
Top 4	7.01 ± 0.19	216000 ± 10000	
Top 5	7.51 ± 0.17	72700 ± 4000	
Top 6	8.06 ± 0.24	251000 ± 160000	
Top 7	8.84 ± 0.32	71700 ± 3000	1831.71 ± 244.08
Top 8	9.56 ± 0.25	68300 ± 1000	2395.44 ± 306.04
Top 9	10.4 ± 0.49	80200 ± 2000	1922.7 ± 247.8
Top 10	11.3 ± 0.29	61700 ± 2000	2252.13 ± 295.15
Top 11	12.07 ± 0.27	57300 ± 1000	2234.73 ± 286.67
Top 12	12.85 ± 0.29	48600 ± 1000	1989.61 ± 256.31
Top 13	13.93 ± 0.58	70700 ± 2000	1797.2 ± 232.97
Top 14	15.05 ± 0.4	38700 ± 1000	1606.41 ± 208.5
Top 15	15.99 ± 0.4	34900 ± 1000	1388.7 ± 180.96
Top 16	17.08 ± 0.64	29000 ± 1000	1168.55 ± 153.94
Bottom 1	13 ± 0.25	34404 ± 640	1799.58 ± 233.33
Bottom 2	13.72 ± 0.18	36440 ± 405	1588.79 ± 203.87
Bottom 3	14.51 ± 0.41	54101 ± 540	1551.57 ± 197.68
Bottom 4	15.36 ± 0.28	37000 ± 400	1609.25 ± 206.45
Bottom 5	16.14 ± 0.4	31700 ± 318	1146.84 ± 146.59
Bottom 6	16.99 ± 0.3	27122 ± 326	1129.78 ± 144.95
Bottom 7	17.75 ± 0.24	20161 ± 254	1026.58 ± 132.28
Bottom 8	18.54 ± 0.4	22207 ± 258	894.59 ± 114.67
Bottom 9	19.4 ± 0.32	15510 ± 177	724.76 ± 93.14
Bottom 10	20.21 ± 0.32	12679 ± 154	620.67 ± 79.88
Bottom 11	21.02 ± 0.32	10130 ± 150	521.8 ± 67.38
Bottom 12	21.87 ± 0.4	9010 ± 156	411.01 ± 53.07
Bottom 13	22.74 ± 0.31	6278 ± 136	341.47 ± 44.47
Bottom 14	23.55 ± 0.32	5008 ± 143	281.67 ± 37.09
Bottom 15	24.42 ± 0.4	4344 ± 148	226.55 ± 30.08
Bottom 16	25.35 ± 0.4	1902 ± 77	105.23 ± 14.18

Table 3.10 Peak areas and calculated reaction cross sections from the detectors used in the measurement of d(^{12}C,^{13}N)n at 21 MeV/A.

Detector	Center of Mass Angle	Area of Gaussian Fit	Reaction Cross Section (mb/sr)
Top 1	10.82 ± 0.42	154 ± 89	0.77 ± 0.46
Top 2	12.53 ± 0.49	268 ± 42	0.9 ± 0.22
Top 3	14.17 ± 0.5	368 ± 28	1.17 ± 0.23
Top 4	15.66 ± 0.4	320 ± 23	1.1 ± 0.22
Top 5	16.76 ± 0.33	219 ± 22	0.96 ± 0.2
Top 6	18.05 ± 0.53	381 ± 26	1.13 ± 0.22
Top 7	19.82 ± 0.7	330 ± 31	0.91 ± 0.19
Top 8	21.52 ± 0.58	257 ± 19	1 ± 0.2
Top 9	23.46 ± 1.2	194 ± 22	0.51 ± 0.11
Top 10	25.6 ± 0.67	173 ± 20	0.67 ± 0.14
Top 11	27.45 ± 0.64	139 ± 13	0.58 ± 0.12
Top 12	29.33 ± 0.73	83 ± 16	0.36 ± 0.1
Top 13	31.97 ± 1.44	177 ± 17	0.46 ± 0.1
Top 14	34.76 ± 1	62 ± 15	0.27 ± 0.08
Top 15	37.11 ± 1.03	57 ± 11	0.23 ± 0.06
Top 16	39.9 ± 1.64	57 ± 22	0.22 ± 0.09
Bottom 1	28.41 ± 0.62	86 ± 12	0.38 ± 0.09
Bottom 2	30.16 ± 0.42	105 ± 11	0.41 ± 0.09
Bottom 3	32.11 ± 1.03	151 ± 14	0.37 ± 0.08
Bottom 4	34.21 ± 0.71	97 ± 15	0.36 ± 0.09
Bottom 5	36.14 ± 1	73 ± 11	0.22 ± 0.05
Bottom 6	38.3 ± 0.76	79 ± 11	0.27 ± 0.06
Bottom 7	40.24 ± 0.63	52 ± 11	0.21 ± 0.06
Bottom 8	42.26 ± 1.04	84 ± 14	0.28 ± 0.07
Bottom 9	44.5 ± 0.82	57 ± 8	0.21 ± 0.05
Bottom 10	46.62 ± 0.84	58 ± 10	0.23 ± 0.06
Bottom 11	48.77 ± 0.86	63 ± 14	0.24 ± 0.07
Bottom 12	51.07 ± 1.08	60 ± 11	0.21 ± 0.05
Bottom 13	53.41 ± 0.85	61 ± 8	0.25 ± 0.06
Bottom 14	55.63 ± 0.87	48 ± 6	0.2 ± 0.04
Bottom 15	58.02 ± 1.12	46 ± 7	0.18 ± 0.04
Bottom 16	60.6 ± 1.12	37 ± 9	0.14 ± 0.04
Neutron 1	22.57 ± 1.21	50 ± 7	0.57 ± 0.13
Neutron 2	17.93 ± 1.03	71 ± 8	0.84 ± 0.18
Neutron 4	12.16 ± 0.84	66 ± 8	0.88 ± 0.19
Neutron 5	10.47 ± 0.79	60 ± 8	0.84 ± 0.19
Neutron 8	13.96 ± 0.9	74 ± 9	0.87 ± 0.19
Neutron 14	28.01 ± 1.43	13 ± 4	0.26 ± 0.09

Table 3.11 Peak areas and calculated reaction cross sections from the detectors used in the measurement of d(^{7}Be,^{8}B)n at 25 MeV/A.

Detector	Center of Mass Angle	Area of Gaussian Fit	Reaction Cross Section (mb/sr)
Top 1	6.78 ± 0.29		
Top 2	7.91 ± 0.33		
Top 3	8.98 ± 0.31		
Top 4	9.95 ± 0.27		
Top 5	10.67 ± 0.24	292 ± 82	6.38 ± 2.19
Top 6	11.45 ± 0.35		
Top 7	12.57 ± 0.46	389 ± 65	5.53 ± 1.43
Top 8	13.61 ± 0.35		
Top 9	14.82 ± 0.71	330 ± 64	4.47 ± 1.24
Top 10	16.12 ± 0.42		
Top 11	17.24 ± 0.39	201 ± 35	4.31 ± 1.13
Top 12	18.37 ± 0.42	192 ± 29	4.38 ± 1.09
Top 13	19.95 ± 0.85	285 ± 35	4.06 ± 0.94
Top 14	21.6 ± 0.59	176 ± 18	4.19 ± 0.93
Top 15	22.99 ± 0.59	187 ± 18	4.21 ± 0.92
Top 16	24.61 ± 0.95	147 ± 25	3.28 ± 0.86
Bottom 1	18.6 ± 0.37	215 ± 23	3.67 ± 0.83
Bottom 2	19.65 ± 0.26	153 ± 24	2.29 ± 0.58
Bottom 3	20.81 ± 0.6	368 ± 72	3.68 ± 1.02
Bottom 4	22.06 ± 0.41	297 ± 40	4.32 ± 1.03
Bottom 5	23.21 ± 0.59	305 ± 46	3.66 ± 0.91
Bottom 6	24.48 ± 0.44	283 ± 53	3.85 ± 1.05
Bottom 7	25.6 ± 0.36	160 ± 26	2.73 ± 0.7
Bottom 8	26.77 ± 0.6	257 ± 64	3.56 ± 1.13
Bottom 9	28.06 ± 0.47	221 ± 54	3.42 ± 1.08
Bottom 10	29.27 ± 0.48	177 ± 31	2.83 ± 0.75
Bottom 11	30.49 ± 0.49	121 ± 21	2.11 ± 0.56
Bottom 12	31.78 ± 0.61	115 ± 22	1.8 ± 0.5
Bottom 13	33.09 ± 0.48	39 ± 20	0.7 ± 0.38
Bottom 14	34.32 ± 0.48	40 ± 28	0.77 ± 0.56
Bottom 15	35.64 ± 0.61	9 ± 13	0.16 ± 0.24
Bottom 16	37.05 ± 0.61	13 ± 6	0.23 ± 0.12
Neutron 1	22.72 ± 1.21	54 ± 7	3.11 ± 0.75
Neutron 2	18.07 ± 1.04	92 ± 10	5.44 ± 1.22
Neutron 4	12.25 ± 0.85	125 ± 11	7.7 ± 1.68
Neutron 5	10.54 ± 0.8	144 ± 12	6.08 ± 1.31
Neutron 6	8.92 ± 0.77	125 ± 11	5.04 ± 1.1
Neutron 7	7.37 ± 0.74	104 ± 10	3.62 ± 0.8
Neutron 8	14.06 ± 0.9	119 ± 11	6.74 ± 1.48
Neutron 10	18.07 ± 1.04	50 ± 7	2.33 ± 0.57
Neutron 11	20.31 ± 1.12	67 ± 8	2.6 ± 0.61
Neutron 13	25.34 ± 1.32	59 ± 8	2.68 ± 0.64
Neutron 14	28.17 ± 1.42	54 ± 7	2.48 ± 0.6

Chapter 4

Optical Model Analysis

In order to understand the data from Experiment 96019, Optical Model calculations were performed and the results were compared to the measured scattering and transfer reaction data. Such an analysis allows the measured cross sections to be related to structural properties of the nuclei involved.

4.1 Theoretical Background of the Optical Model

The Optical Model is an effective model in which the interactions of an incident particle with the nucleons of the nucleus are replaced by the interaction of the incident particle with a potential-energy well. The aim is to find a potential that can reproduce the measured scattering cross section. The features of this potential then give information about the general or average structure of the nuclei involved in the reaction.

Nuclear scattering can be divided into two categories: elastic scattering in which only the direction of the incoming particle is changed, and inelastic scattering in which the particle is scattered into an exit channel different from the incident one. The Optical Model treats these two possibilities analogously to the study of optical waves, with elastic

scattering corresponding to *refraction* of the wave at the surface of the potential, and inelastic scattering corresponding to *absorption*. As is the case with optics, a complex potential is used to describe the nucleus, with refraction caused by the real potential, and absorption caused by the imaginary part. A more complete description of the Optical Model can be found in [Wo90].

In order to calculate nuclear scattering cross sections, an Optical Model potential is chosen to describe the nuclear potential. The Schrodinger equation for the scattering is then given by

$$(\nabla^2 + k^2)\psi(r) = \tfrac{2\mu}{\hbar^2}V(r)\psi(r)$$

where *V(r)* is the sum of the Coulomb potential and the Optical Model Potential, μ is the reduced mass of the projectile and target, and *k* is the relative momentum. The solution to this equation can be expressed as

$$\psi(r) = e^{ik_i \cdot r} + \tfrac{2\mu}{\hbar^2}\int G(r,r')V(r')\psi(r')d^3r'$$

where G(r,r') is a Green's Function. The scattering amplitude *f*(θ) determined by this wave function is given by

$$f(\theta) \approx -\tfrac{\mu}{2\pi\hbar^2}\int e^{-ik_f \cdot r'}V(r')e^{ik_i \cdot r'}d^3r'$$

The scattering amplitude is then directly related to the differential cross section by the simple expression

$$\frac{d\sigma}{d\Omega}(\theta,\phi) = |f(\theta,\phi)|^2$$

A variety of more complicated reactions are possible, from transfer of a single particle between the nuclei, to the complete absorption of the projectile and the formation of the compound nucleus. The single nucleon transfer reactions are powerful probes of nuclear structure because detailed analyses are possible in an Optical Model framework. On the other hand, compound nuclear reactions probe the average statistical properties of nuclei.

4.2 Practical Application of the Optical Model

In practice, the Phenomenological Optical Model is often used to interpret the results of direct reactions. In the analysis of data with this technique, a trial potential is used to make an initial calculation of the cross section, and the parameters of the trial potential are then adjusted to fit the calculated cross section to the measured data. This trial potential is then refined and the general properties of the wave functions can be determined.

It has been found that Optical Model potentials with a Woods-Saxon shape do a good job of reproducing measured cross sections for a wide range of data. The Woods-Saxon potential has the form

$$V(r) = \frac{V_0}{1+\exp\left[\frac{r-r_0 A^{1/3}}{a}\right]}$$

where V_0 is the well depth, r_0 is the reduced radius, and a is the diffuseness. The Woods-Saxon form has 3 adjustable parameters (V_0, r_0, a), thus an Optical potential containing both real and imaginary Woods-Saxon potentials has 6 free parameters (V, r_V, a_V, W, r_W, a_W).

Trial potentials can be obtained either from a microscopic calculation [Wo90], or from a previous experiment involving nearby nuclei at a similar bombarding energy. Several compilations of phenomenological Optical Model potentials have been published, including those by Becchetti & Greenlees [Be69] and Perey & Perey [Pe76]. In addition, global fits have been made to these compilations, parameterizing the behavior of optical potentials over a range of projectiles, targets, and incident energies. These global parameter sets allow extrapolation to new energies and targets. Such global optical potential sets have been formulated for common light projectiles, including protons [Va91], neutrons [Ra82, Va91], and deuterons [Bo88, Da80]. Note that these global sets were all formulated using data on heavier targets than those in this work.

For a simple scattering process, the entrance channel is identical to the exit channel, and only one Optical potential is needed to describe the reaction. During a transfer reaction, however, the identity of the nuclei are changed by the reaction, and a second potential is needed to describe the exit channel. For example, analysis of the d(^{12}C,^{13}N)n reaction requires one optical potential to describe the ^{12}C + d entrance

channel, and another potential to describe the $^{13}N + n$ exit channel. Thus, there are 12 free parameters in the calculation of the d(^{12}C,^{13}N)n cross section, and a larger uncertainty for each parameter.

In order to reduce the number of free parameters in the calculation of a transfer reaction cross section, it is advantageous to measure the elastic scattering of the entrance channel at the same center-of-mass energy. In this way, an Optical potential can be fit to the elastic scattering data, and that potential can be used as the entrance channel potential in the calculation of the transfer reaction, reducing the number of free parameters in the transfer reaction calculation. In the same way, the elastic scattering of the reverse reaction (exit channel) could be measured, fixing all of the parameters of the transfer reaction calculation.

In this work, we have measured the reaction cross sections of both d(^{12}C,^{13}N)n and d(^{7}Be,^{8}B)n, and the scattering cross sections of d(^{12}C,^{12}C)d and d(^{7}Be,^{7}Be)d. Though the experiment was not designed specifically to measure the scattering cross sections, the scattering products were detected in the forward telescopes, and the scattering cross sections could be extracted over a certain angular range. Measurement of the neutron exit channels would be helpful for calculations of the transfer reaction cross section, but such measurements would be rather difficult, and were beyond the scope of the experiment. Our goal is to use the measurements of the d(^{12}C,^{12}C)d and d(^{7}Be,^{7}Be)d scattering cross sections to determine Optical potentials for the entrance channels of the d(^{12}C,^{13}N)n and d(^{7}Be,^{8}B)n reactions. Then, the transfer reaction cross section can be calculated, and the exit channel Optical potentials can be fitted.

There were no data for our reaction systems at comparable energies in the literature. A large number of calculations were performed using a variety of Optical Model potentials for similar reactions at similar energies and with potentials obtained from global analyses. These Finite-Range Distorted-Wave Born Approximation (DWBA) calculations were performed using the code FRESCO [Th88]. Table 4.1 and Table 4.2 list the parameters of the Optical Potentials used in the remainder of this work for the analysis of d(^{12}C,^{13}N)n and d(^{7}Be,^{8}B)n, respectively. Sample input for the code can be found in Appendix B.

Table 4.1 Optical Model Potential parameters used for the calculations of d(^{12}C,^{12}C)d and d(^{12}C,^{13}N)n described in this chapter.

Name	Reference	Nuclei	V	r_V	a_V	W_{vol}	r_{Wvol}	a_{Wvol}	W_{surf}	r_{Wsurf}	a_{Wsurf}	V_{so}	r_{so}	a_{so}	r_C
daeh	[Da80]	^{12}C + d	78.53	1.17	0.77	2.11	1.31	0.67	11.2	1.31	0.67	5.87	1.07	0.66	1.3
bojo	[Bo88]	^{12}C + d	75.08	1.18	0.72	0	1.27	0.82	10.2	1.27	0.82	6	0.87	0.87	
rap	[Ra82]	^{13}N + n	42.81	1.2	0.66	10.2	1.3	0.59	0	1.29	0.59	6.2	1.01	0.75	
CH89	[Va91]	^{12}C + d	42.39	1.15	0.69	15.5	1.15	0.69	5.06	1.15	0.69	5.9	0.82	0.63	
CH89	[Va91]	^{13}N + n	42.52	1.15	0.69	14.2	1.15	0.69	5.53	1.15	0.69	5.9	0.83	0.63	
sche	[Sc84]	^{12}C + d	118	0.89	0.93				6.11	1.52	0.79	5	0.89	0.93	1.3
sche	[Sc84]	^{13}N + n	44.8	1.31	0.66				9.19	1.26	0.48	11	1.12	0.57	1.3

Table 4.2 Optical Model Potential parameters used for the calculations of d(^{7}Be,^{7}Be)d and d(^{7}Be,^{8}B)n described in this chapter.

Name	Reference	Nuclei	V	r_V	a_V	W_{vol}	r_{Wvol}	a_{Wvol}	W_{surf}	r_{Wsurf}	a_{Wsurf}	V_{so}	r_{so}	a_{so}	r_C
daeh	[Da80]	^{7}Be + d	75.75	1.17	0.78	2.97	1.31	0.65	10.57	1.31	0.65	5.61	1.07	0.66	1.3
bojo	[Bo88]	^{7}Be + d	72.36	1.18	0.7	0.63	1.27	0.81	9.34	1.27	0.81	6	0.85	0.85	1.3
rap	[Ra82]	^{8}B + n	44.31	1.2	0.66	11.36	1.29	0.59	0.53	1.29	0.59	6.2	1.01	0.75	1.3
liu1	[Li96]	^{7}Be + d	138.74	1.02	0.86	14.84	1.64	0.29	16.34	1.31	0.76	7	1.64	0.81	1.3
liu1	[Li96]	^{8}B + n	48.19	1.13	0.72				11.33	1.43	0.66	6.2	1.13	0.77	1.3
CH89	[Va91]	^{7}Be + d	38.64	1.13	0.69	13.02	1.11	0.69	3.44	1.11	0.69	5.9	0.71	0.63	1.3
CH89	[Va91]	^{8}B + n	43.86	1.14	0.69	13.09	1.12	0.69	6.74	1.12	0.69	5.9	0.74	0.63	1.3
nun1		^{7}Be + d	51.73	1.24	0.97	13.2	1.38	0.54				1.51	3.86	0.41	1.97
nun3		^{7}Be + d	31.63	1.96	0.88				2.05	3.71	0.42				1.88
nun5		^{7}Be + d	42.27	1.56	0.85	24.4	0.77	0.7				1.62	3.81	0.57	1.75
nunC		^{7}Be + d	37.44	1.04	0.81	15.9	1.43	0.56				1.82	4.28	0.65	1.97
olss	[Ol90]	^{8}B + n	49.41	1.02	0.62				3.47	1.6	0.6	1.25	1.1	0.56	1.25

4.3 Survey of Published Optical Potential Parameters

In order test the applicability of previous work on the present data, calculations were made using a variety of Optical potentials found in the literature. Calculations were performed for both scattering and transfer reactions. Additional calculations of the scattering processes will be discussed in Section 4.7, and additional calculations of the transfer reactions will be discussed in Section 4.8. The literature potential parameters used are tabulated in Table 4.1 and Table 4.2 for d(^{12}C,^{13}N)n and d(^{7}Be,^{8}B)n, respectively.

Figure 4.1 shows the measured cross sections of the d(^{12}C,^{12}C)d quasi-elastic scattering and the d(^{12}C,^{13}N)n transfer reaction (The sum of elastic and inelastic scattering is referred to as *quasi-elastic* scattering, a term which will be used in the remainder of this document). Also shown are the results of several DWBA calculations using published optical potentials. For the ^{12}C + d entrance channel potentials, the blue curves use the global deuteron potentials described by Bojowald et al. [Bo88], while the red curves use the global deuteron potential described by Daehnick et al. For the ^{13}N + n exit channel potentials, the solid lines use the global neutron potential described by Rapaport [Ra82], while the dashed lines use the *CH89* global neutron potential [Va91]. Also shown is a calculation using entrance and exit channel potentials from a previous measurement of d(^{12}C,^{13}N)n by Schelin et al. [Sc84]. This measurement was made at 13 MeV, so it is not expected that potentials determined for such a low energy will reproduce the present data.

Each of these calculations uses a Woods-Saxon potential to bind the ^{13}N, the parameters of which are tabulated in Table 4.3. A Gaussian potential is used to bind the deuteron, the parameters of this potential are given in Table 4.4.

The overall agreement between calculation and measurement seems good, but not excellent. The curves do not follow the quasi-elastic scattering data, having deeper minima. The calculations also overestimate the transfer reaction cross section.

Figure 4.2 shows the measured cross sections of the d(^{7}Be,^{7}Be)d scattering to the ground and first excited states of ^{7}Be, and the d(^{7}Be,^{8}B)n transfer reaction. Also shown are the results of several DWBA calculations using several published optical potentials. For the ^{7}Be + d entrance channel potentials, the blue curves use the global deuteron potentials described by Bojowald et al. [Bo88], while the red curves use the global deuteron potential described by Daehnick et al. For the ^{8}B + n exit channel potentials, the solid lines use the global neutron potential described by Rapaport [Ra82], while the dashed lines use the CH89 global neutron potential [va91]. Also shown is a calculation using entrance and exit channel potentials from a previous measurement of d(^{7}Be,^{8}B)n by Liu et al. [Li96] The measurement of d(^{7}Be,^{8}B)n by Liu et al. was made at 7.4 MeV, so the potentials are not expected to reproduce the present data, but are included for completeness.

Each of these calculations uses the Woods-Saxon potential calculated by Tombrello [To65] to bind the ^{8}B, the parameters of which are tabulated in Table 4.3. A Gaussian potential is used to bind the deuteron, the parameters of this potential are given

in Table 4.4. The input file for the calculation using the Daehnick entrance channel and Rapaport exit channel parameters is given in Appendix B.

As shown in Figure 4.1 and Figure 4.2, none of the potentials derived from previous work give an adequate description of the measured cross sections. Thus, it is necessary to use these potentials as a starting point, and determine if the calculations can describe the measurements with adjusted parameters.

Table 4.3 Parameters of the Woods-Saxon potentials used to bind the products of the (d,n) reactions.

Name	Nucleus	Reference	V	r	a	V_{so}
tomb	^{13}N	[To65]	32.62	1.54	0.52	
tomb	^{8}B	[To65]	32.62	1.54	0.52	
kim	^{8}B	[Ki87]	32.12	1.48	0.52	8.24
stnd	^{8}B		50	1.25	0.65	

Table 4.4 Parameters of the Gaussian potential used to bind the deuteron in the DWBA calculations. The potential has the functional form used in the Fresco code:

$$V = -P1 \quad \exp\left[-\left(\frac{r-(P2 \quad A^{1/3})}{P3}\right)^2\right]$$

P1	P2	P3	A
72.15	0	1.48	1

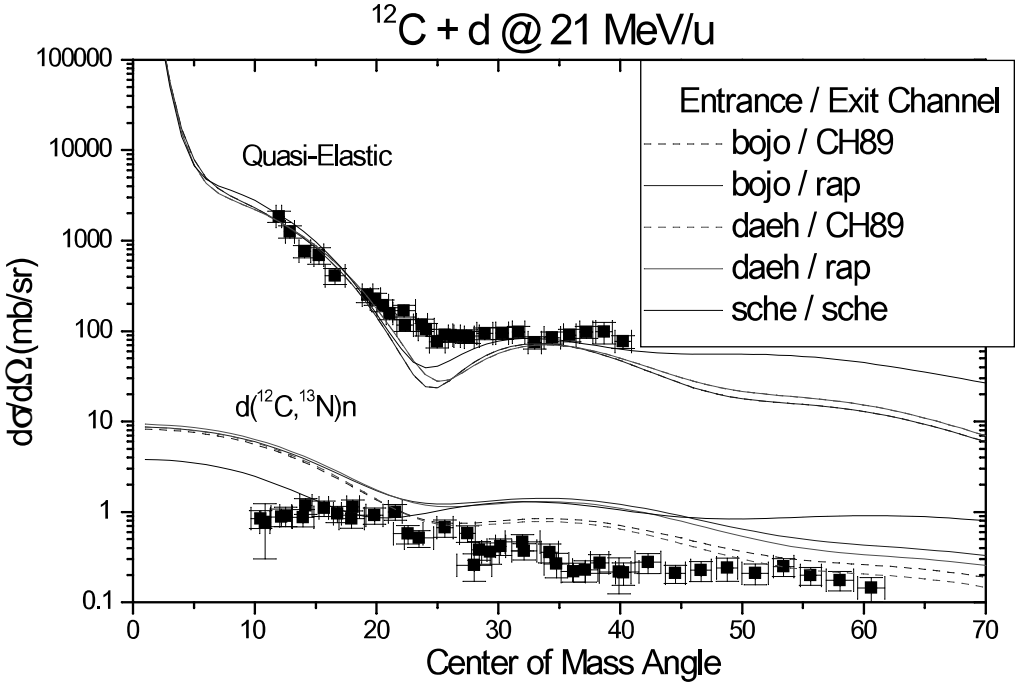

Figure 4.1 DWBA calculations of the d(^{12}C,^{12}C)d quasi-elastic and d(^{12}C,^{13}N)n transfer reactions at 21 MeV/u. Each line represents a different combination of entrance and exit channel parameters from the literature.

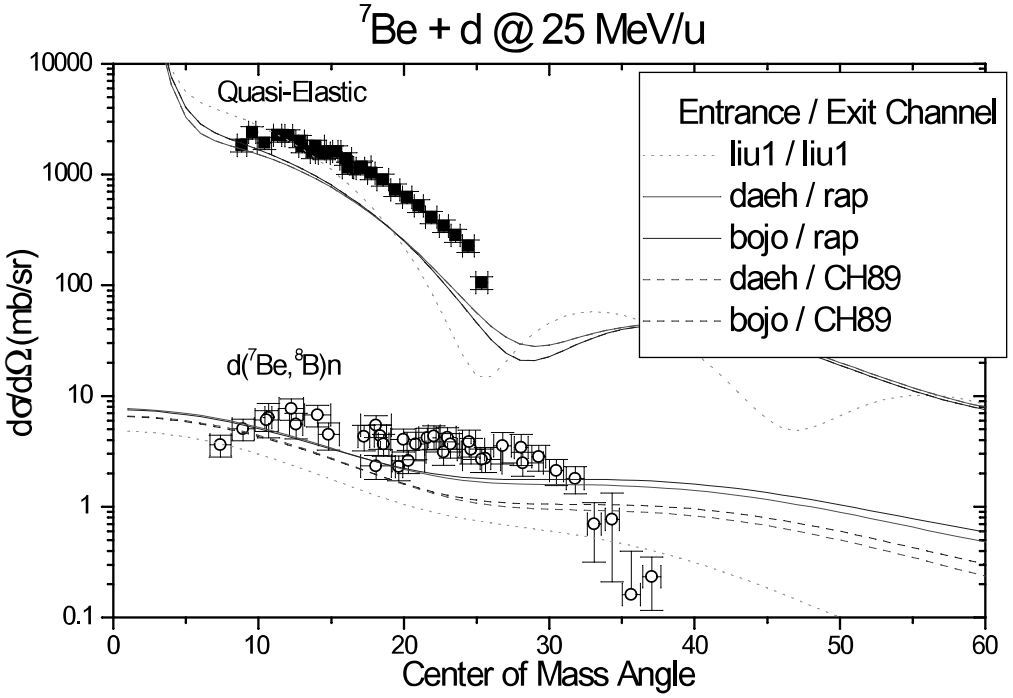

Figure 4.2 DWBA calculations of the d(^{7}Be,^{7}Be)d quasi-elastic and d(^{7}Be,^{8}B)n transfer reactions at 25 MeV/u. Each line represents a different combination of entrance and exit channel parameters from the literature.

4.4 Variation of Optical Potential Parameters

In order to try to reproduce the experimentally measured cross section in the DWBA framework, the parameters of the optical potential were adjusted to the data. In order to understand the effect each parameter has on the shape of the calculated DWBA cross section, the parameters were explored individually. The results of these calculations are shown in Figure 4.3 for the d(^{12}C,^{12}C)d scattering and in Figure 4.4 for the d(^{7}Be,^{7}Be)d scattering to the ground and first excited states of ^{7}Be. The solid line represents the calculation using the global deuteron optical potentials of Daehnick et al, and in each panel the dashed and dotted lines show the effect of varying one parameter of either the real or imaginary potential.

The results of this search indicated that the observed data cannot be adequately described by simply changing the values of the parameters in the potentials. This realization led to an exploration of the effects of projectile (heavy nucleus) excitation and deuteron breakup on the present data.

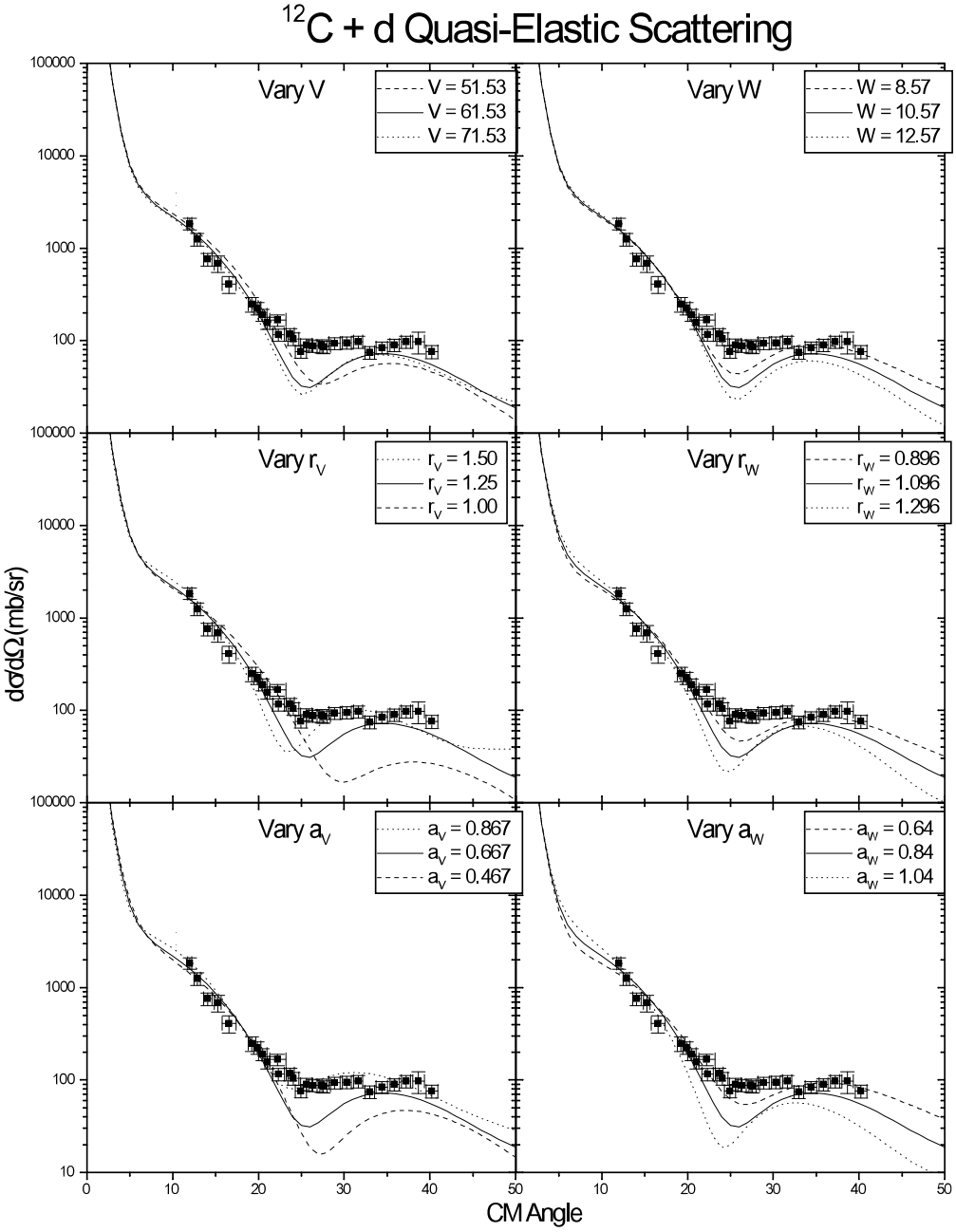

Figure 4.3 DWBA calculations of the quasi-elastic scattering of ^{12}C from deuterium at 21 MeV/u. The solid line in each panel represents the calculation made using the global deuteron parameters of Daehnick et al. [Da80]. In each panel, one of the parameters of the real or imaginary potentials is varied.

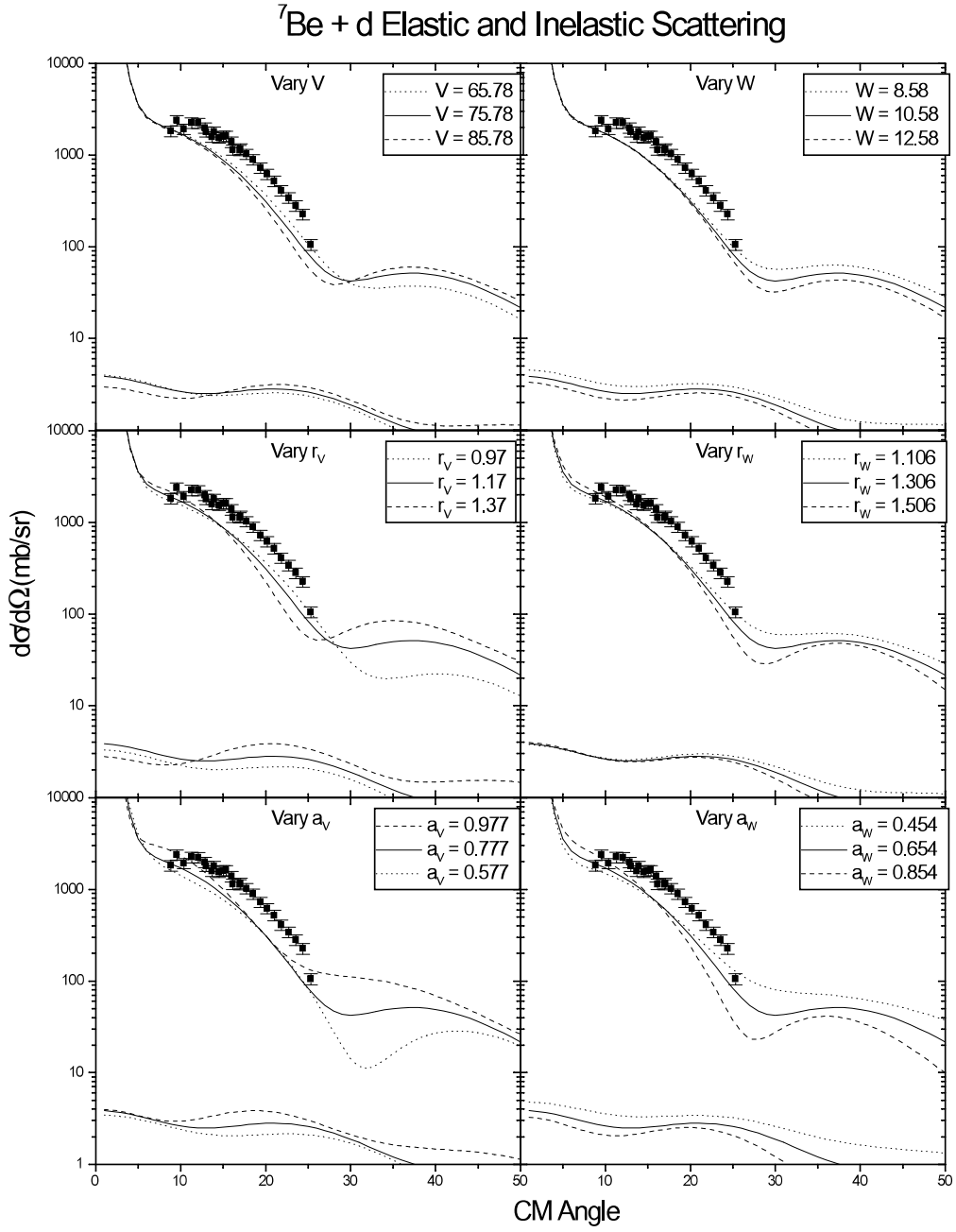

Figure 4.4 DWBA calculations of the elastic and inelastic scattering of ^{7}Be from deuterium at 25 MeV/u. The solid line in each panel represents the calculation made using the global deuteron parameters of Daehnick et al. [Da80]. In each panel, one of the parameters of the real or imaginary potentials is varied

4.5 Estimate of the Contribution of Projectile Excitation

Because of the limited energy resolution of the measurement of the heavy fragment, the observed scattering cross sections contain contributions from both elastic and inelastic scattering. In order to estimate the relative contribution of the inelastic processes, DWBA calculations were performed using the FRESCO code [Th88].

Figure 4.5 shows the results of the DWBA calculation of the d(^{12}C,^{12}C)d scattering to both the ground and first excited states of ^{12}C. The calculation uses the global deuteron Optical potential as described by Daehnick et al. [Da80]. The 2+ state of ^{12}C is populated via Coulomb excitation, the calculation uses a deformation length of 1.648 fm ($\beta \approx 0.58$), a deformation which has been shown to be valid for this state [Kh95]. The calculation shows that at small angles, the elastic scattering is dominant, but near 20° inelastic scattering to the 2+ state becomes important. At these angles, the measurement of d(^{12}C,^{12}C)d is likely to contain a significant contribution from both the ground and first excited state of ^{12}C. Any fitting of Optical potentials will have to include the contributions from scattering to this 2+ state.

Figure 4.6 shows a similar calculation for the d(^{7}Be,^{7}Be)d scattering. The global deuteron Optical potential described by Daehnick et al. [Da80] was again used. The DWBA calculation uses the ^{7}Be deformation $\beta = 0.566$, a deformation calculated in [Do97]. Similar DWBA calculations have also been performed with $\beta = 0.383$, a value calculated in [Va97], which decreases the cross section to the ^{7}Be first excited state. Both calculations show that scattering to the excited state of ^{7}Be is likely to be a small

contribution to the measured cross section. In the fitting of Optical parameters, contributions from scattering to this state can be ignored. Thus, in order to understand the discrepancy between measured and calculated cross sections, the contribution from excitation of the deuterium target must be examined.

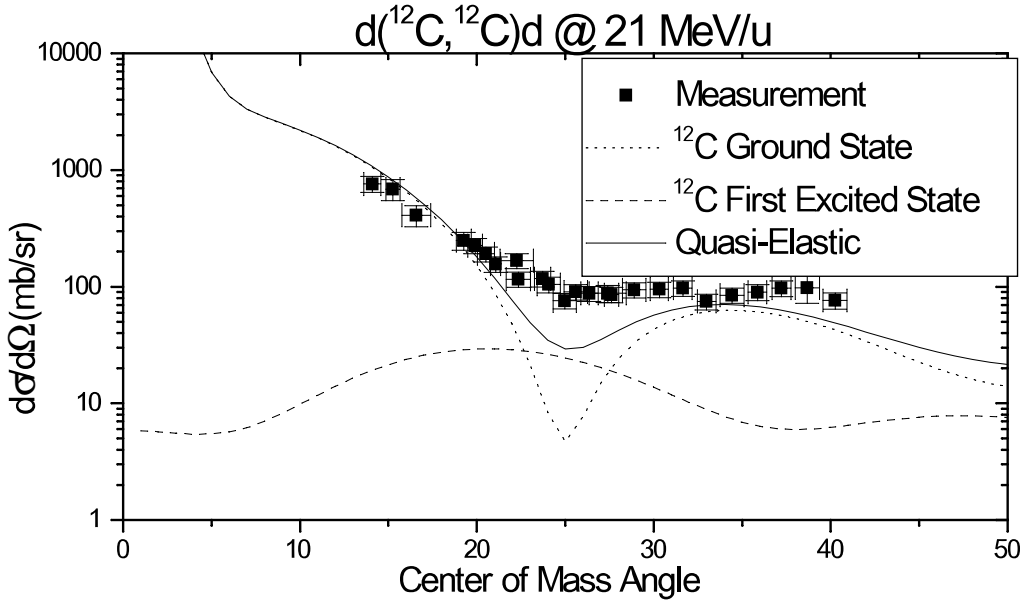

Figure 4.5 DWBA calculations of the scattering of ^{12}C from deuterium at 21 MeV/u. Calculations are shown for both the ground and first excited states of ^{12}C. The sum of these two processes is the solid line, referred to as the quasi-elastic scattering.

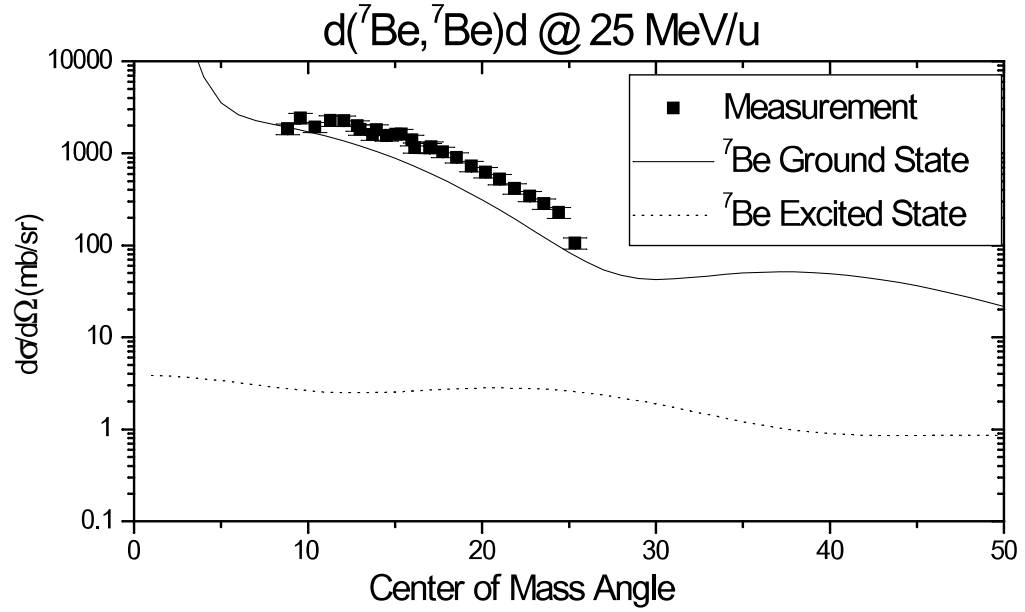

Figure 4.6 DWBA calculations of the scattering of ^{7}Be from deuterium at 25 MeV/u. Calculations are shown for both the ground and excited states of ^{7}Be.

4.6 Estimate of the Contribution of Target Excitation

In addition to internal excitation of the scattered particle, the deuterium target can also be excited in the scattering process. However, the deuteron does not have any bound excited states and will be broken up in the excitation process. Such target excitations are a complication of the inverse kinematics measurement that was not present in traditional forward kinematics studies. In a forward kinematics experiment, if the deuteron is detected, then it was not excited. In inverse kinematics the deuteron is not measured, and only with a precise measurement of the energy of the scattered particle can its excitation be detected. With the limited energy resolution of the current study, these events could not be isolated from the elastic scattering events. We will rely on a calculation to estimate the contribution of deuteron excitation to the measured cross sections.

A calculation of the scattering cross section of ^{7}Be + d leading to continuum states of the deuteron has been performed by F. Nunes [Nu98]. The results of these calculations are shown in Figure 4.7, along with the measured d(^{7}Be,^{7}Be)d scattering cross section. The calculation shows that deuteron excitation events are likely to be a significant part of the measured cross section, particularly at angles >15°. In the fitting of Optical parameters, contributions from scattering events that excite the deuteron target cannot be ignored. In order to resolve the elastic data, the calculated deuteron excitation cross section should be subtracted from the measured cross section, leaving the purely elastic cross section.

A measurement of the deuteron excitation cross section has also been extracted from the data. Neutrons in coincidence with ^{7}Be events in the Bottom Fragment Detector were observed in Neutron Detectors 14, 15, and 16. A Monte Carlo simulation of the ^{7}Be inelastic scattering and subsequent deuteron breakup was performed, and the energies of the observed neutrons were found to be consistent with an average deuteron excitation energy of ~5.5 MeV, which agrees very well with the calculation of deuteron excitation discussed above. The simulation also calculated the geometric acceptance of the neutron detectors for the deuteron breakup, and the average cross section for deuteron excitation was determined over the angular coverage of the Bottom Fragment Detector (11°→24° CM). The observed cross section for this angular range is plotted in Figure 4.7. Note that the large uncertainty in the angle of this measurement reflects the angular range over which the measurement is averaged. While the measured cross section is significantly lower than the calculation, it suggests that deuteron excitation is still likely to be a significant contribution to the measured cross section, particularly at large angles.

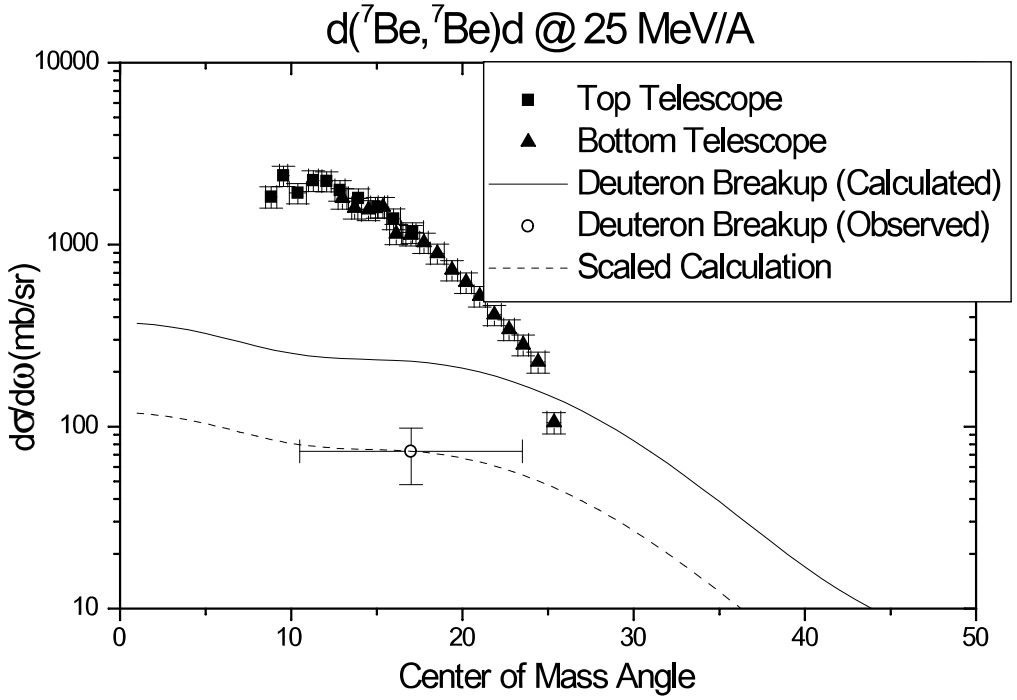

Figure 4.7 The scattering cross section of ^{7}Be from deuterium leaving the deuteron in an unbound excited state. The solid line represents a calculation of this cross section, the open circle is the observed cross section. The dashed line shows the result of scaling the calculation to match the measurement. Note that the large uncertainty in the angle of the deuteron breakup measurement represents the angular range over which the measurement is averaged. The solid data points are the measured scattering cross section, shown for comparison. Because of the limited energy resolution, deuteron excitation events will contribute to the measured scattering cross section.

4.7 Fitting of Optical Potentials to the Scattering Data

In order to obtain Optical Potentials that reproduce the measured cross sections, the parameters were adjusted to fit the data. This was performed using the code CUPID [Co78]. There were no restrictions on the Optical parameters in these fits. Fits to the ^{7}Be + d scattering data have been made with and without corrections for deuteron excitation.

In Figure 4.9, the measured cross section (without correction for deuteron excitation) is shown, along with three potentials that have been fit to the data. The parameters of these potentials (*nun1, nun2, nun3*) are tabulated in Table 4.2. The calculations using these potentials reproduce the measured cross section rather well, but the data cannot distinguish between these three very different Optical Potentials. Measurement of the cross section at larger angles would have reduced these ambiguities.

Figure 4.10 shows the scattering data that has been corrected for the effect of deuteron excitation. The correction was made by subtracting the calculated cross section for deuteron excitation (Figure 4.7) from the measured d(^{7}Be,^{7}Be)d scattering cross section (Figure 3.32). An Optical potential was fitted to this corrected data (which should be purely elastic), and the resulting DWBA cross section is shown. The parameters of the fitted Optical potential (*nunC*) are given in Table 4.2.

Fits to the ^{12}C + d quasi-elastic data have not been performed. As discussed in Section 4.5 and Section 4.6, the contributions of both projectile and target excitations are expected to contribute significantly to the measured cross section. Fitting of Optical potentials to this data is likely to lead to large uncertainties in the parameters.

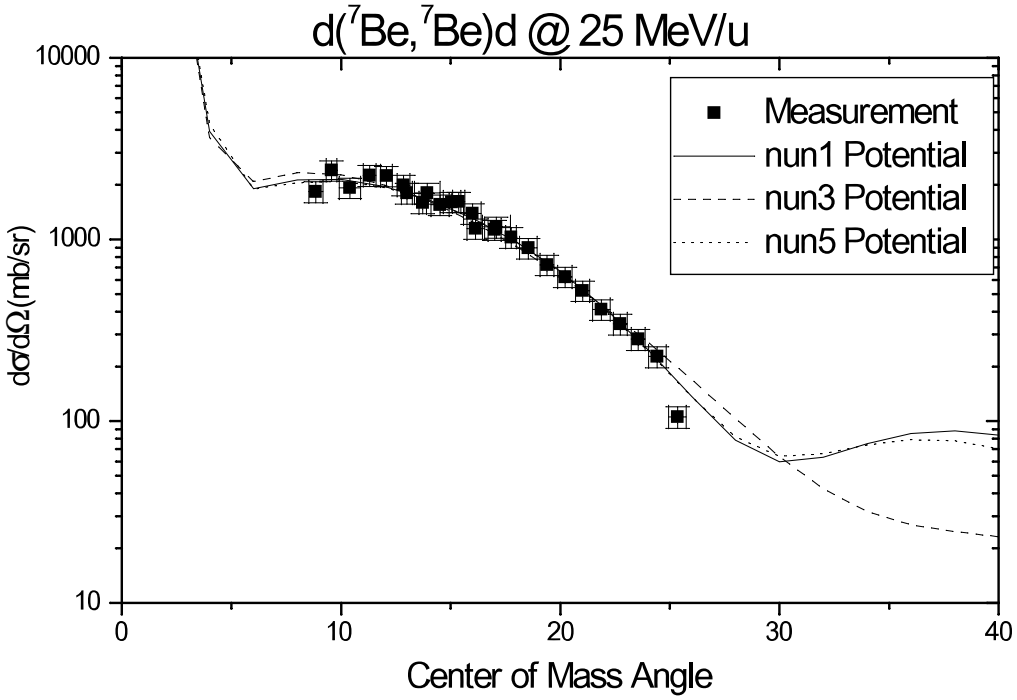

Figure 4.9 Measured d(^{7}Be,^{7}Be)d scattering cross section and DWBA calculations of the elastic scattering using 3 potentials which were fit to the measurement. The parameters of these potentials are given in Table 4.2.

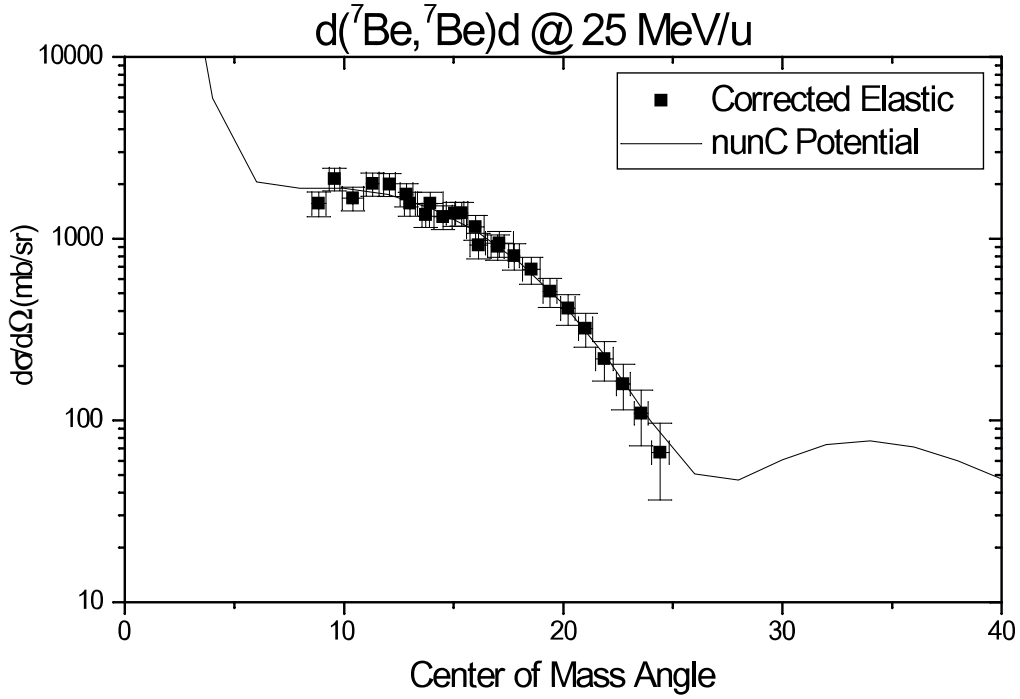

Figure 4.10 Scattering cross section of d(^{7}Be,^{7}Be)d which has been corrected for the effect of deuteron excitation. The points represent the calculated deuteron excitation cross section (Figure 4.7) subtracted from the measured scattering cross section (Figure 3.32). The curve is a DWBA calculation using a potential which has been fitted to the corrected data. The data point at the largest center-of-mass angle has been discarded. The parameters of the *nunC* potential are given in Table 4.2.

4.8 Optical Model Calculations of the Transfer Reaction

In Figure 4.1 and Figure 4.2, the results of DWBA calculations for the scattering and transfer reactions using several potentials from the literature were presented. The agreement between these calculations and the data was unsatisfactory, and led us to adjust the potentials to fit the scattering data. Potentials were fit to the observed scattering data, and also to the data corrected for deuteron excitation. These scattering potentials can now be used as entrance channel potentials for the d(^{7}Be,^{8}B)n transfer reaction calculations, and exit channel potentials can be explored.

Figure 4.11 shows the DWBA calculations using the *nun1* potential for the entrance channel, and several different literature potentials for the exit channel. The *nun1* potential was fit to the measured d(^{7}Be,^{7}Be)d scattering cross section, without corrections for deuteron excitation. The calculations overestimate the reaction cross section, and none of the exit channel potentials reproduce the shape of the angular distribution. The Spectroscopic Factor S_{lj} can be extracted from the comparison of the experimental and calculated cross sections. S_{lj} is given by

$$_{ex}(\ \ _0) = S_{lj}\ \ _{DWBA}(\ \ _0)$$

where $\sigma_{ex}(\theta_0)$ and $\sigma_{DWBA}(\theta_0)$ are the experimental and calculated cross sections near zero degrees. Figure 4.11 includes the extracted value of S_{lj} for each calculation, and the effect of multiplying the measured cross section is shown in the lower panel of the figure.

Figure 4.12 shows the results of DWBA calculations using the *nunC* potential for the entrance channel, and several literature potentials for the exit channel. The *nunC*

potential was fit to the d(^{7}Be,^{7}Be)d cross section which was corrected by subtracting the calculated deuteron excitation cross section. Again, the calculations overestimate the reaction cross section and fail to reproduce the shape of the angular distribution. Also shown is the result of multiplying the calculated cross section by the indicated Spectroscopic Factors, S_{lj}.

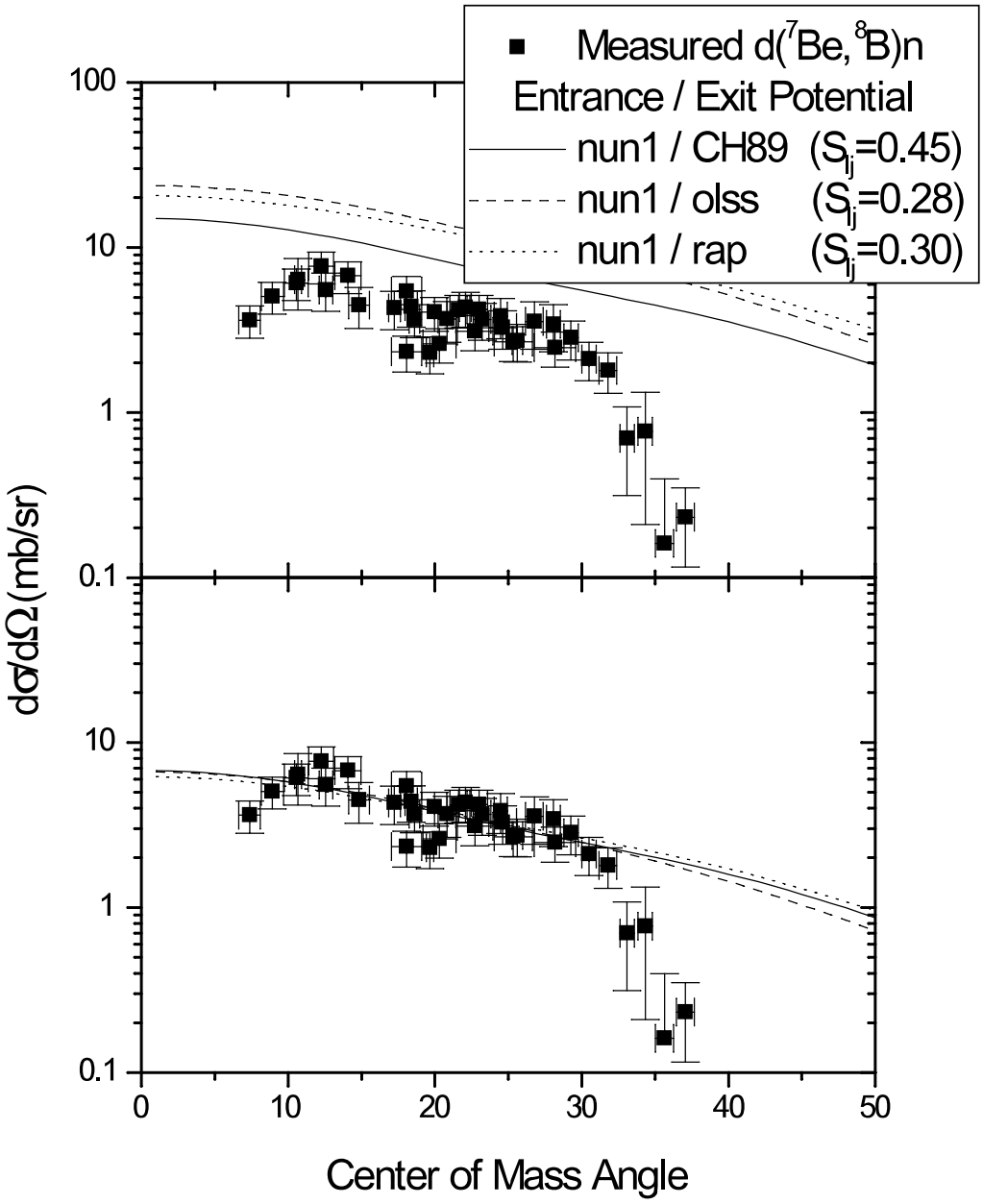

Figure 4.11 DWBA calculations of the d(^{7}Be,^{8}B)n transfer reaction. The entrance channel potential is *nun1*, which was fit to the measured scattering data, and the exit channel potentials were taken from the literature. These potentials are described in Table 4.2. For all calculations the *tomb* potential was used to bind the ^{8}B, which is described in Table 4.3. In the upper panel, the raw results are shown. The lower panel shows the results of the calculation multiplied by the given Spectroscopic Factor S_{lj}.

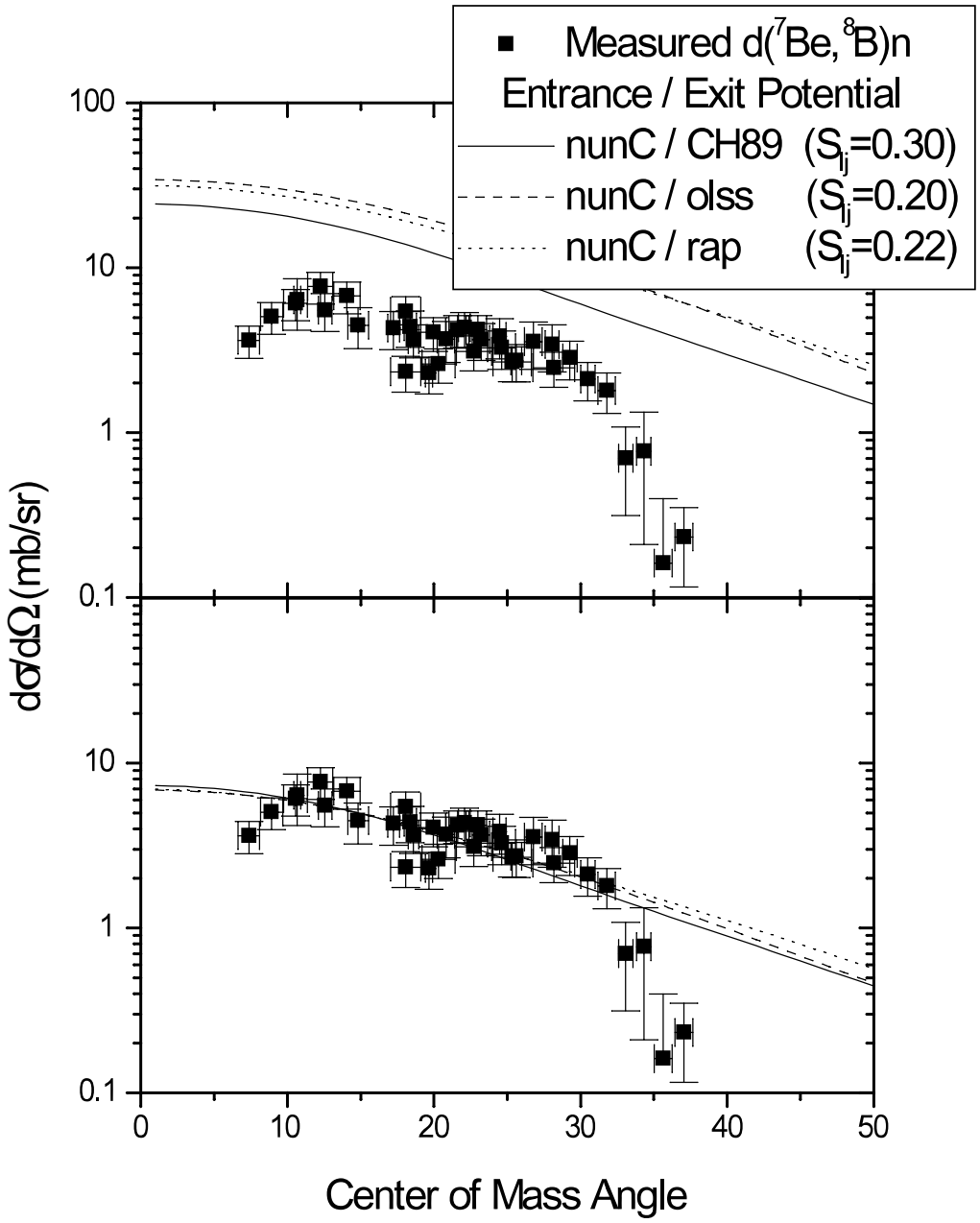

Figure 4.12 DWBA calculations of the d(^{7}Be,^{8}B)n transfer reaction with corrections for deuteron excitation. The entrance channel potential is *nunC*, which was fit to the scattering data corrected by the calculated deuteron excitation cross section. The exit channel potentials were taken from the literature. These potentials are described in Table 4.2. For all calculations the *tomb* potential was used to bind the ^{8}B, which is described in Table 4.3. In the upper panel, the raw results are shown. The lower panel shows the results of the calculation multiplied by the given Spectroscopic Factor S_{lj}.

Figure 4.13 explores the sensitivity of the measured d(^{7}Be,^{8}B)n data to the potential used to bind the ^{8}B in the DWBA calculation. The figure shows several DWBA calculations using the *nun1* entrance and *CH89* exit channel potentials. In each calculation, a different potential is used to bind the ^{8}B product. The parameters of the binding potentials are listed in Table 4.3. Though none of the calculations reproduce the experimental cross section, it can be seen that the calculation has very little sensitivity to the binding potential used. In order to discriminate between these binding potentials, very precise data at small angles is needed. It can also be seen that the choice of binding potential has little effect on the value of the Spectroscopic Factor S_{lj}.

Following the method described by Xu et al., the d(^{7}Be,^{8}B)n transfer reaction can be used to calculate the $S_{17}(0)$ factor for the ^{7}Be(p,γ)^{8}B reaction [Xu94]. This method uses the Asymptotic Normalization Coefficient C_{lj} to calculate $S_{17}(0)$. C_{lj} is given by

$$C_{lj} = S_{lj}^{1/2} \quad _{lj}$$

where S_{lj} is the Spectroscopic Factor, and β_{lj} is the normalization coefficient of the asymptotic part of the ^{8}B wave function, which is determined by the ^{8}B binding potential. The astrophysical factor $S_{17}(0)$ is has been shown by Barker to be almost directly proportional to C_{lj}^{2}, such that $C_{lj}^{2}/S_{17}(0) \approx 0.026$ [Ba80]. The value of $S_{17}(0)$ has been extracted for each of the calculations shown in Figures 4.11 and 4.12, the results are given in Table 4.5. The values of $S_{17}(0)$ determined from this work are much lower than the currently accepted value $S_{17}(0) = 19^{+4}_{-2}$ eV b [IN97].

A partial wave analysis of the calculated cross section illustrates the reason for the lack of sensitivity of the current work to the value of $S_{17}(0)$. Figure 4.14 shows the

contribution of various values of the orbital angular momentum L to the total calculated cross section. The solid line represents the contribution of all partial waves to the cross section. The other lines show the effect on the cross section of removing the partial waves inside of a certain radius, for example the dashed line includes contributions to the total cross section at radii greater than 1 fm. It can be seen from this figure that contributions to the cross section from radii greater than 2 fm are very small. At 25 MeV/u, the transfer reaction probes very deeply into the nucleus, and the contribution from transfer reactions at the nuclear surface is small. Because the determination of $S_{17}(0)$ from the d(^{7}Be,^{8}B)n reaction relies on a peripheral reaction sampling the tail of the wave function [Xu94], this measurement is not a sensitive probe of the value of $S_{17}(0)$.

Table 4.5 Calculation of $S_{17}(0)$ from the d(^{7}Be,^{8}B)n transfer reaction. A separate value of S17(0) is extracted for each of the calculations in Figures 4.11 and 4.12. Those using the *nunC* entrance channel potential include corrections for deuteron excitation, those using the *nun1* potential do not.

calculation	nun1/CH89	nun1/olss	nun1/rap	nunC/CH89	nunC/olss	nunC/rap
S_{lj}	0.45	0.28	0.30	0.30	0.20	0.22
β_{lj}	0.7838	0.7838	0.7838	0.7838	0.7838	0.7838
C_{lj}^2	0.28	0.17	0.18	0.18	0.12	0.14
$S_{17}(0)$	10.6	6.6	6.9	6.9	4.6	5.2

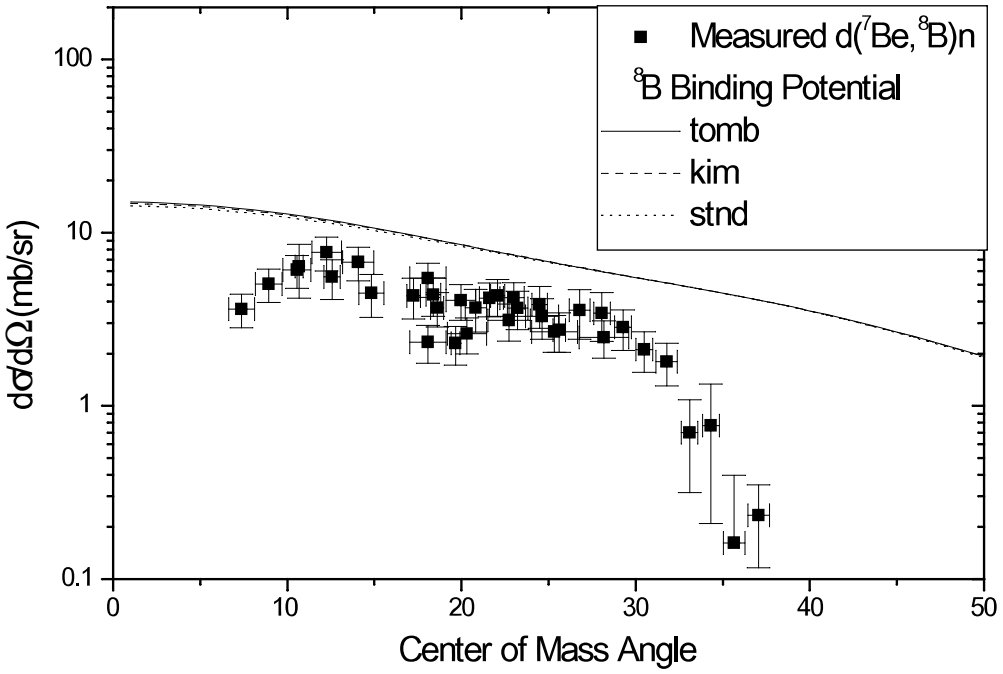

Figure 4.13 Exploration of the effect of different ^{8}B binding potentials on the calculated cross section. In each calculation, a different potential has been used to bind the ^{8}B product. The parameters of these ^{8}B binding potentials are given in Table 4.3. For all calculations, the *nun1* entrance and *CH89* exit channel potentials were used. A very precise measurement of the transfer reaction cross section extending to very small angles would be required to pick from among these different binding potentials.

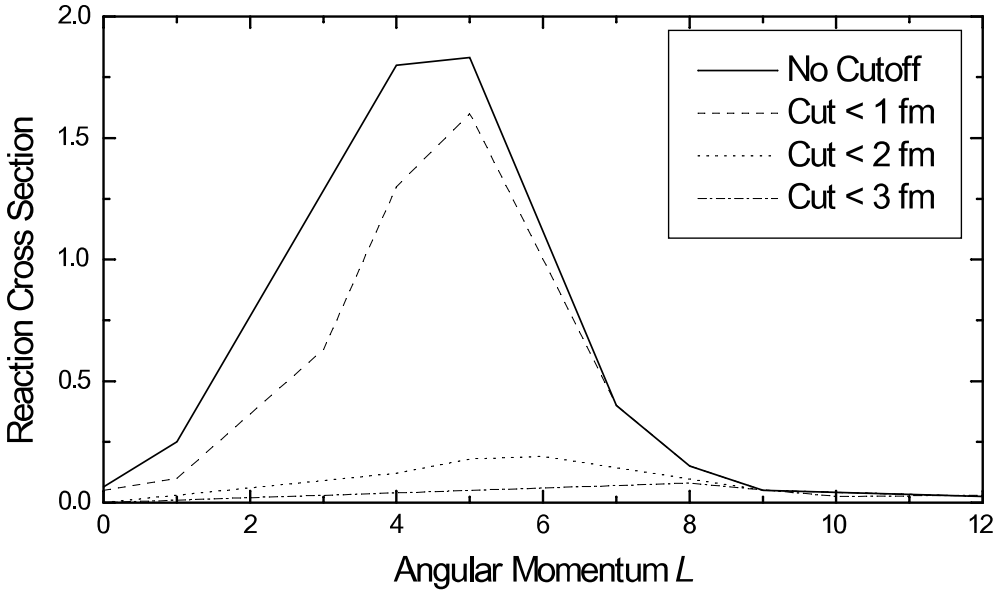

Figure 4.14 The contribution to the total d(^{7}Be,^{8}B)n cross section of partial waves with certain values of orbital angular momentum *L*. The points are joined with lines. The solid line shows the contribution to the cross section for all values of the radius. The dashed line shows the contribution to the cross section from radii greater than 1 fm. The figure shows that nearly all of the transfer reaction cross section comes from interactions at radii less than 2 fm.

Chapter 5

Conclusions

This work was the first of its kind: a coincidence measurement of a transfer reaction in inverse kinematics using a radioactive beam. As such, its successes and failures can be helpful in the planning of future experiments. The primary results of this work are the measurements of two cross sections, the scattering of ^{7}Be from deuterium, and the transfer reaction d(^{7}Be,^{8}B)n.

5.1 Measurement and Analysis of the Scattering Reaction

The measurement of the d(^{7}Be,^{7}Be)d scattering cross section was limited by the inability to clearly resolve the inelastic contributions to the measured cross sections. While the use of silicon telescopes gave an accurate identification of the scattering products, their limited energy resolution prevented us from resolving inelastic scattering to excited states of the projectile. In addition, their small angular coverage only allowed the scattering cross section to be measured over a small range of angles. The use of a spectrometer (such as the S800 at the NSCL) would avoid these limitations in future studies.

In addition to inelastic contributions from the excitation of ^{7}Be, scattering events leading to excitation of the deuteron have also been shown to make an important contribution to the measured scattering cross section. Because deuteron excitation is a continuum process, a precise measurement of the energy of the scattered particle (such as with a spectrometer) cannot resolve these events from other inelastic processes above the 2.2 MeV binding energy of the deuteron. In order to quantify the contribution of deuteron excitation, it is necessary to measure this process. We have shown that this can be accomplished by measurement of the neutron from deuteron breakup. Alternatively, the elastic scattering process could be resolved by measuring the recoiling deuteron in coincidence with the scattered projectile.

The limitations due to inelastic contributions to the measured scattering cross section, along with the limited angular range of the scattering measurement, have led to significant uncertainty in the Optical Model analysis of the scattering cross sections. Several different potentials have been presented that reproduce the scattering cross section with equal accuracy. This uncertainty in the analysis of the scattering process contributed to the uncertainty in the analysis of the transfer reaction.

5.2 Measurement and Analysis of the Transfer Reaction

This study of d(^{7}Be,^{8}B)n was the first to make a kinematically-complete coincidence measurement of the reaction cross section. The coincidence measurement was quite successful, with very good agreement between the cross section measured using

the ^{8}B events and the cross section measured using the neutrons in coincidence with ^{8}B. We have shown that such a measurement is feasible, it reduces the statistical uncertainty, and it provides a good check for self-consistency.

The Optical Model analysis of the measured d(^{7}Be,^{8}B)n cross section was limited by uncertainty of the entrance channel potential, as discussed above, and also by uncertainty in the exit channel potential. The lack of available data for neutron scattering from ^{8}B has forced us to use exit channel potentials derived from studies of other nuclei. Several different exit channel potentials have been shown to predict similar reaction cross sections.

From the measured d(^{7}Be,^{8}B)n cross section and the DWBA calculations, the Spectroscopic Factor for this reaction has been determined to be 0.29 ± 0.09. This is in contrast to the measurement of the Spectroscopic Factor for the mirror reaction ^{7}Li(d,p)^{8}Li (E_d= 12 MeV) which has been shown to be 0.87 [Sc67].

It has been shown by Xu et al. that the cross section of d(^{7}Be,^{8}B)n can be used to determine the value of the Astrophysical $S_{17}(0)$ Factor [Xu94]. We have demonstrated that because of the high bombarding energy, our work is not particularly sensitive to the value of $S_{17}(0)$.

BIBLIOGRAPHY

Bibliography

[Al95] J. S. Al-Khalili *et al.*, Nucl. Phys. **A581**, 331 (1995).

[Ba80] F. C. Barker, Aust. J. Phys. **33**, 177 (1980).

[Ba92] J. N. Bahcall and M. Pinsonneault., Rev. Mod. Phys. **64**, 885 (1992).

[Ba95] D. Bazin *et al.*, Phys. Rev. Lett. **74**, 3569 (1995).

[Be69] F. D. Becchetti, Jr. and G. W. Greenlees, Phys. Rev. **182**, 1190 (1969).

[Be93] Yu. A. Berezhnoy and V. Yu. Korda, Nucl. Phys. **A556**, 453 (1993).

[Bo88] J. Bojowald *et al.*, Phys. Rev. **C38**, 1153 (1988).

[Ce79] R. A. Cecil, B. D. Anderson, and R. Madey, Nucl. Inst. Meth. 161, 439 (1979).

[Co78] J. R. Comfort, Computer Phys. Commun. **16**, 35 (1978).

[Da80] W. W. Daehnick *et al.*, Phys. Rev. **C21**, 2253 (1980).

[Do97] A. Doté *et al.*, Phys. Rev. **C56**, 1844 (1997).

[Fe92] Herman Feshbach, *Theoretical Nuclear Physics* (Wiley-Interscience, New York, 1992) pp 455-463.

[Fr81] G. Friedlander, J. W. Kennedy, E. S. Macias, J. M. Miller, *Nuclear and Radiochemistry* (Wiley-Interscience, New York, 1981) p32.

[Fu91] M. Fukuda *et al.*, Phys. Lett. **B268**, 339 (1991).

[Ha92] R. Harkewicz, Ph.D. Thesis, NSCL (1992).

[IN92] INT Workshop on Solar Fusion Cross Sections, Rev. Mod. Phys., to be published October 1998.

[Ke96] J. H. Kelley *et al.*, Phys. Rev. Lett. **77**, 5020 (1996).

[Ki87] K. H. Kim *et al.*, Phys. Rev. **C35**, 363 (1987).

[Li91] W. Z. Liu, Ph.D. Thesis, University of Michigan (1991).

[Li96] W. Liu *et al.*, Phys. Rev. Lett. **77**, 611 (1996).

[Mi92] T. Minamisono *et al.*, Phys. Rev. Lett. **69**, 2058 (1992).

[Na94] H. Nakada and T. Otsuka, Phys. Rev. **C49**, 886 (1994).

[Nu98] F. Nunes, private communication (1998).

[Ol90] N. Olsson *et al.*, Nucl. Phys. **A509**, 161 (1990).

[Or92] N. A. Orr *et al.*, Phys. Rev. Lett. **69**, 2050 (1992).

[Pe72] C. A. Pearson *et al.*, Nucl. Phys. **A191**, 1 (1972).

[Pe76] C. M. Perey and F. G. Perey, Atom. Data and Nucl. Data Tab. **17**, 1 (1976).

[Pe95] I. Pecina *et al.*, Phys. Rev. **C52**, 191 (1995).

[Ra82] J. Rapaport, Phys. Rep. **87**, 25 (1982).

[Sc67] J. P. Schiffer *et al.*, Phys. Rev. **164**, 1274 (1967).

[Sc84] H. R. Schelin *et al.*, Nucl. Phys. **A414**, 67 (1984).

[Sc93] K. W. Scheller, Ph.D. Thesis, Notre Dame (1993).

[Sc95] W. Schwab *et al.*, Z. Phys. **A350**, 283 (1995).

[Sh91] B. M. Sherrill, D. J. Morrissey, J. A. Nolen, Jr. and J. A. Winger, Nucl. Inst. Meth. **B56/57**, 1106 (1991).

[St95] M. Steiner, Ph.D. Thesis, Michigan State University (1995).

[Sw94] D. Swan, J. Yurkon, D. J. Morrissey, Nucl. Inst. Meth. **A348**, 314 (1994).

[Ta85] I. Tanihata *et al.*, Phys. Rev. Lett. **55**, 2676 (1985).

[Ta88] I. Tanihata *et al.*, Phys. Lett. **B206**, 592 (1988).

[To65] T. A. Tombrello, Nucl. Phys. **71**, 459 (1965).

[Th88] I. J. Thompson, Comp Phys. Rep. **7**, 167 (1988).

[Va91] R. L. Varner *et al*., Phys. Rep. **201**, 57 (1991).

[Va97] K. Varga *et al*., Nucl. Phys. **A616**, 383c (1997).

[Wa95] R. E. Warner *et al*., Phys. Rev. **C**52, R1166 (1995).

[Wo90] Samuel S. M. Wong, *Introductory Nuclear Physics* (Prentice-Hall, New Jersey, 1990) pp 336-354.

[Xu94] H. M. Xu *et al*., Phys. Rev. Lett. **73**, 2027 (1994).

[Za93] M. Zahar *et al*., Phys. Rev. **C48**, R1484 (1993).

APPENDICES

Appendix A

Fabrication of Thin Polyethylene Foils

The preparation of thin foils for use as target materials is an important technique in experimental nuclear physics. Targets must be of uniform thickness, and thin enough to minimize energy straggling. In some instances targets must have a large area, and in the case of isotopically enriched targets, must be manufactured with efficient use of expensive raw materials. A recent effort to produce thin polyethylene targets at the NSCL was motivated by the desire to use ^{13}C as the target nucleus in reaction studies using radioactive nuclear beams. Enriched polyethylene (in either ^{13}C or deuterium) is commercially available from several sources, and the raw material can be fashioned into target quality films. We describe a technique developed to prepare thin foils of polyethylene meeting the above criteria.

The first successful method used at the NSCL for fabrication of polyethylene foils is described in [St95]. This technique used several stages of melting under vacuum to remove trapped air from the sample, then the sample was clamped between two heated blocks of steel. The technique was able to produce foils with thickness as small as ~40 μm

(~4 mg/cm^2 polyethylene), but the uniformity was difficult to control and a minimum of 24 hours was required to produce a single foil.

Another technique developed previously to produce polyethylene foils is described in [Li91]. This method involves dissolving the polyethylene in xylene, pouring onto a glass plate, and heating to drive off the xylene, leaving a film of polyethylene behind. This technique was reported to produce films down to a thickness of ~10 μm (~1 mg/cm^2 polyethylene), but attempts at the NSCL failed to produce a target of acceptable quality.

Our most successful method to date to produce thin foils of polyethylene involves forming the target using a heated hydraulic press (Carver Model 2112). The raw material (~200 mg for a 30 μm target of ~10 cm^2) is placed between two pieces of highly polished steel, with brass shim stock used as a spacer between the plates to set the desired target thickness. The plates are placed in the heated press and compressed under 15,000 lbs of force at 250°F for three minutes. The heat and high pressure consistently produce foils of high quality in a very short period of time. Thicknesses as small as 30 μm (~3 mg/cm^2 polyethylene) and thickness uniformity of 3% FWHM over an area of 10 cm^2 have been produced.

The choice of raw material is important for target fabrication. Enriched polyethylene can be purchased in either low or high-density forms. High-density polyethylene is much more rigid and has a higher melting point (>300°F), which led to difficulty in constructing quality targets. Enriched polyethylene obtained from ISOTEC,

Inc. proved to be very suitable for target fabrication. The fine powder produced foils without problems caused by air inclusion.

Appendix B

Sample Input for the FRESCO Code

This Appendix contains sample input for the FRESCO code [Th88] which was used to calculate the scattering and transfer reaction cross sections presented in this work.

Figure B1 shows the input used for the calculations of d(^{12}C,^{12}C)d and d(^{12}C,^{13}N)n, which are shown as the solid red lines in Figure 4.1. This calculation uses the global deuteron potential described by Daehnick et al. [Da80] for the ^{12}C + d entrance channel, and the global neutron potential described by Rapaport [Ra82] for the ^{13}N + n exit channel. These potentials are listed as *daeh* and *rap*, respectively, in Table 4.1. The potential listed as *tomb* in Table 4.3 is used to bind the ^{13}N product, while the gaussian potential used to bind the deuteron is given in Table 4.4.

Figure B2 shows the input used for the calculations of d(^{7}Be,^{7}Be)d and d(^{7}Be,^{8}B)n which are shown as the solid red lines in Figure 4.2. This calculation uses the global deuteron potential described by Daehnick et al. [Da80] for the ^{7}Be + d entrance channel, and the global neutron potential described by Rapaport [Ra82] for the ^{8}B + n exit channel. These potentials are listed as *daeh* and *rap*, respectively, in Table 4.2. The calculation

uses the potential described by Tombrello [To65] to bind the ^{8}B product, which is listed as *tom*b in Table 4.3. The potential used to bind the deuteron is given in Table 4.4.

```
cat > params.$$    << EOF
     PARAMETER (MXP=3, MXX=7, MXPEX=10,  MLOC=70, MAXIT=10, MSP=15,
    #          MAXN=400, MAXNLN=200, MAXNLO=60, LMAX1=40, MAXNNU=36,
    #          MAXCH=50, MAXB=60, MAXF=150, MFNL=150, MAXQRN=60,
    #          MAXV=1500000, INH = 0, MPAIR=1)
EOF
cat > data.$$ << EOF
12C(d,n)13N-dwba-Finite Range-Ed=42 MeV-daeh,rap params, arbitrary 13N binding
0.100   35.00   0.20    0.2000   4.900   +0.20
  0. 30.   .01   F F
0 0.0    90.    1.0     0.0
0.0        1 1 0  36  00  00 0.05     -4.0   0.01
 0 0 0 0 1 1 0 0 0 0
DEUT    2.0141  1.0       2  12C     12.0000  6.0    0.0000
1.0   +1 0.00000          1  0.0   +1  0.000
   1                   1  2.0   +1  4.439
NEUTRON 1.00866 0.0       1  13N     13.0057  7.0    -0.281
0.5   +1 0.00000          2  0.5   -1  0.000

  1 0  0 12.0   0.00    1.30
  1 1  0 78.53  1.17    0.77    2.11    1.31    0.67
  111 10        1.648
  1 2  0                    11.2    1.312   0.666
  111 10        1.648
  1 4  0 5.87   1.07    0.66
  2 0  0 13.0   0.00    1.30
  2 1  0 42.81  1.2     0.66    10.2    1.3     0.59
  2 2  0                    0.0     1.295   0.59
  2 4  0 6.2    1.01    0.75
  3 0  0 1.000          1.25
  3 1  2 72.15  0.00    1.4840
  4 0  0 12.0           1.25
  4 1  0 50.00  1.25    0.65

  1    1 2 1 0   1 0   0.5   0.5    3  0   2.225  1  0  0  1  0.000
  2    1 2 2 0   1 1   0.5   0.5    4  0   1.944  1  0  0  1  0.000

 -2   1   7 0 0 0
     1   1   1   1  1.00
     2   1   1   2  1.0

  0   1   1 1 1 1
41.63
EOF
```

Figure B1 Sample input for the FRESCO code which was used to calculate the cross

sections of d(^{12}C,^{12}C)d and d(^{12}C,^{13}N)n. This calculation produces the cross sections shown as the solid lines in Figure 4.1.

```
cat > params.$$    << EOF
     PARAMETER (MXP=3, MXX=7, MXPEX=10,  MLOC=70, MAXIT=10, MSP=15,
    #          MAXN=400, MAXNLN=200, MAXNLO=60, LMAX1=40, MAXNNU=36,
    #          MAXCH=50, MAXB=60, MAXF=150, MFNL=150, MAXQRN=60,
    #          MAXV=1500000, INH = 0, MPAIR=1)
EOF
cat > data.$$ << EOF
7Be(d,n)8B-dwba-Finite Range-Ed=50 MeV-daeh,rap params-tombrello 8B binding
0.100   35.00   0.20    0.2000   4.900   +0.20
  0. 30.   .01   F F
0 0.0    90.    1.0     0.0
0.0        1 1 0  36  00  00 0.05     -4.0   0.01
 0 0 0 0 1 1 0 0 0 0
DEUT    2.0141  1.0        1  7Be     7.0000   4.0    0.0000
1.0   +1 0.00000          1  1.5   -1  0.000
NEUTRON 1.0086  0.0        1  8B      8.0000   5.0    -2.088
0.5   +1 0.00000          2  2.0   +1  0.000

  1 0  0 7.0    0.00    1.3
  1 1  0 75.75  1.17    0.78    2.97    1.31    0.65
  1 2  0                  10.6    1.305   0.654
  1 4  0 5.61   1.07    0.66
  2 0  0 8.0    0.00    1.3
  2 1  0 44.31  1.2     0.66    11.4    1.3     0.59
  2 2  0                  0.53    1.295   0.59
  2 4  0 6.2    1.01    0.75
  3 0  0 1.000          1.25
  3 1  2 72.15  0.00    1.4840
  4 0  0 7.0            1.25
  4 1  0 32.62  1.54    0.52

  1    1 2 1 0   1 0   0.5   0.5    3  0   2.225  1  0  0  1  0.0000
  2    1 2 2 0   1 1   0.5   1.5    4  0   0.137  1  0  0  1  0.000

 -2   1   7 0 0 0
     1   1   1   1  1.00
     2   1   1   2  1.0

  0   1   1 1 1 1
50.0
EOF
/ ... params ... all/bin/fresco params.$$ < data.$$
```

Figure B2 Sample input for the FRESCO code which was used to calculate the cross

sections of d(^{7}Be,^{7}Be)d and d(^{7}Be,^{8}B)n. This calculation produces the cross sections shown as the solid lines in Figure 4.2.